

CZECH TECHNICAL UNIVERSITY IN PRAGUE
Faculty of Nuclear Sciences and Physical Engineering
Department of Physics



MASTER'S THESIS

**Efficiency and accuracy of time-of-flight detector
measurements in the ATLAS experiment and di-photon
vertex reconstruction for the search for an axion-like
particle in data from LHC Run-3**

Viktoriia Lysenko
Supervisor: doc. Dr. André Sopczak
Prague, 2023

ČESKÉ VYSOKÉ UČENÍ TECHNICKÉ V PRAZE

Fakulta Jaderná a Fyzikálně Inženýrská

Katedra fyziky



DIPLOMOVÁ PRÁCE

**Účinnost a přesnost měření detektoru doby letu v
experimentu ATLAS a rekonstrukce di-fotónového
vertexu pro pátrání po axionu podobné částici v datech
z LHC Run-3**

Viktoriia Lysenko

Vedoucí práce: doc. Dr. André Sopczak

Praha, 2023



DIPLOMA THESIS ASSIGNMENT

Academic year: 2022/2023

Student: Viktoria Lysenko

Study programme: ***Nuclear and particle physics***

Thesis title:
(in Czech) Účinnost a přesnost měření detektoru doby letu v experimentu ATLAS a rekonstrukce di-fotónového vertexu pro pátrání po axionu podobné částici v datech z LHC Run-3

Thesis title:
(in English) Efficiency and accuracy of time-of-flight detector measurements in the ATLAS experiment and di-photon vertex reconstruction for the search for an axion-like particle in data from LHC Run-3

Language of the Thesis: English

Instructions:

- 1) Familiarise yourself with the ATLAS software for data analysis, including grid processing
- 2) Study the vertex reconstruction for di-photons events
- 3) Demonstrate that the background rejection for an Axion-Like-Particle search will increase with an improved vertex reconstruction, assuming the ToF detector resolution
- 4) Study the ToF detector performance with first LHC Run-3 data
- 5) Use the ToF data and demonstrate an improved vertex reconstruction for di-photon events
- 6) Discuss your results regarding the search for Axion-Like-Particles with LHC Run-3 data

Recommended literature:

- [1] ATLAS Collaboration, Phys. Rev. Lett. 125 (2020) 261801 [2009.14537]
- [2] CMS Collaboration, J. High Energy Phys. 2018, 153.
- [3] ATLAS Collaboration, ATL-COM-FWD-2021-013 [<https://cds.cern.ch/record/2749821>]
- [4] A. Sopczak, et al., ATL-COM-PHYS-2020-238 [<https://cds.cern.ch/record/2714416>]
- [5] L. Adamczyk, et al., ATLAS-TDR-024 [<https://cds.cern.ch/record/2017378>]


Name and affiliation of the supervisor:

doc. Dr. André Sopczak
Institute of Experimental and Applied Physics CTU in Prague

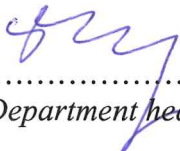
Date of the assignment: 20.10.2022


Due date of the thesis: 03.05.2023

The assignment is valid for two years since the date of the assignment.


.....
Guarantor of the study programme




.....
Department head


.....
Dean

In Prague on 20.10.2022

ZADÁNÍ DIPLOMOVÉ PRÁCE

Akademický rok: 2022/2023



Student: Viktoriia Lysenko

Studijní program: Jaderná a částicová fyzika

Název práce: Účinnost a přesnost měření detektoru doby letu v experimentu ATLAS
(česky) a rekonstrukce di-fotónového vertexu pro pátrání po axionu podobné částici v datech z LHC Run-3

Název práce: Efficiency and accuracy of time-of-flight detector measurements in the
(anglicky) ATLAS experiment and di-photon vertex reconstruction for the search for an axion-like particle in data from LHC Run-3

Jazyk práce: Angličtina

Pokyny pro vypracování:

- 1) Seznamte se s ATLAS softwarem pro analýzu dat včetně gridových výpočtů
- 2) Studium rekonstrukce vertexu pro di-fotónové události
- 3) Ukažte, že potlačení pozadí pro pátrání po axionu podobné částici se zvýší s vylepšenou rekonstrukcí vertexu vzhledem k rozlišení ToF detektoru
- 4) Studium výkonu ToF detektoru z prvních LHC Run-3 dat
- 5) Použijte ToF data a demonstруйте vylepšenou rekonstrukci vertexu pro di-fotónové události
- 6) Diskutujte výsledky týkající se pátrání po axionu podobné částici pomocí LHC Run-3 dat

Doporučená literatura:

- [1] ATLAS Collaboration, Phys. Rev. Lett. 125 (2020) 261801 [2009.14537]
- [2] CMS Collaboration, J. High Energy Phys. 2018, 153.
- [3] ATLAS Collaboration, ATL-COM-FWD-2021-013 [<https://cds.cern.ch/record/2749821>]
- [4] A. Sopczak, et al., ATL-COM-PHYS-2020-238 [<https://cds.cern.ch/record/2714416>]
- [5] L. Adamczyk, et al., ATLAS-TDR-024 [<https://cds.cern.ch/record/2017378>]


Jméno a pracoviště vedoucího diplomové práce:

doc. Dr. André Sopczak
Institute of Experimental and Applied Physics CTU in Prague


Datum zadání diplomové práce: 20.10.2022

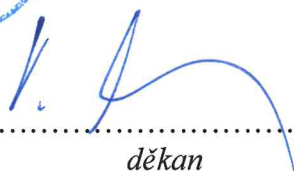
Termín odevzdání diplomové práce: 03.05.2023

Doba platnosti zadání je dva roky od data zadání.


.....
garant studijního programu




.....
vedoucí katedry


.....
děkan

V Praze dne 20.10.2022



PROHLÁŠENÍ

Já, níže podepsaný

Jméno a příjmení studenta: Viktoriia Lysenko
Osobní číslo: 514021
Název studijního programu (oboru): Jaderná a částicová fyzika

prohlašuji, že jsem diplomovou práci s názvem:

Efficiency and accuracy of time-of-flight detector measurements in the ATLAS experiment and di-photon vertex reconstruction for the search for an axion-like particle in data from LHC Run-3

vypracoval(a) samostatně a uvedl(a) veškeré použité informační zdroje v souladu s Metodickým pokynem o dodržování etických principů při přípravě vysokoškolských závěrečných prací.

V Praze dne 1.05.2023

.....


podpis

Acknowledgements

I would like to thank my supervisor, doc. Dr. André Sopczak, for all advises and active involvement during the work. The support for this study by the AFP team, and in particular by the AFP-ToF team is gratefully acknowledged. I also would like to thank my family for the encouragement during my studies.

Viktoriia Lysenko

Title:

Efficiency and accuracy of time-of-flight detector measurements in the ATLAS experiment and di-photon vertex reconstruction for the search for an axion-like particle in data from LHC Run-3

Author: Viktoriia Lysenko

Study program: Nuclear and particle physics

Type of work: Master's thesis

Supervisor: doc. Dr. André Sopczak
Ústav technické a experimentální fyziky ČVUT v Praze

Abstract:

In summer 2022, the first LHC Run-3 proton-proton collision data were recorded with the ATLAS central detector and the ATLAS Forward Proton (AFP) detectors. The first analysis of this new data was performed. Efficiencies and resolutions for the Time-of-Flight (ToF) detector were studied with different methods. In addition, these performance studies of the ToF data included the proton-proton vertex reconstruction using matching of ToF and central ATLAS vertex position. After a calibration, a preliminary resolution of the vertex reconstruction was determined with a low- μ ATLAS run. Based on selected di-photon events, vertex reconstruction studies were conducted using simulated and recorded 2017 data. Different techniques of central ATLAS vertex reconstruction were compared. Using one technique, a di-photon vertex reconstruction was performed with 2022 data. The potential of ToF data for an improved vertex reconstruction and thus reduction of background in an Axion-Like-Particle search using AFP data has been demonstrated.

Key words: LHC Run-3, AFP, ToF, ALP, di-photon

Název práce:

Účinnost a přesnost měření detektoru doby letu v experimentu ATLAS a rekonstrukce di-fotónového vertexu pro pátrání po axionu podobné částici v datech z LHC Run-3

Autor: Viktoriia Lysenko

Studijní program: Jaderná a částicová fyzika

Druh práce: Diplomová práce

Vedoucí práce: doc. Dr. André Sopczak
Ústav technické a experimentální fyziky ČVUT v Praze

Abstrakt:

V létě 2022 byla na Velkém hadronovém urychlovači zaznamenána první data z proton-proton srážek v rámci LHC Runu-3 pomocí centrálního detektoru ATLAS a detektorů ATLAS Forward Proton (AFP). Byla provedena první analýza těchto nově získaných dat. Různými metodami byla studována účinnost a rozlišení detektoru doby letu (ToF). Navíc tyto studie kvality ToF dat zahrnovaly rekonstrukci proton-proton vertexu porovnáním poloh vertexů ToF a centrálního ATLAS. Po kalibraci bylo určeno předběžné rozlišení vertexové rekonstrukce pomocí ATLAS runu s nízkým μ .

Na základě vybraných di-fotonových událostí byly provedeny studie rekonstrukce vertexů pomocí simulovaných dat a zaznamenaných dat z roku 2017. Byly porovnány různé techniky rekonstrukce vertexů za použití centrálního detektoru ATLAS. Pomocí jedné techniky byla provedena di-fotonová rekonstrukce vertexů s daty z roku 2022. Byl prokázán potenciál ToF dat pro vylepšení rekonstrukce vertexů, a tím i snížení pozadí při hledání Axionu podobné částice pomocí AFP dat.

Klíčová slova: LHC Run-3, AFP, ToF, ALP, di-foton

Contents

1	Introduction	1
2	Detector design	3
2.1	ATLAS Central Detector	3
2.2	ATLAS Forward Proton Detector	4
2.3	Time-of-Flight Detector	5
3	First analysis of the ToF detector with LHC Run-3 Data	7
3.1	Data selection	7
3.2	Time resolution	8
3.3	Efficiency	24
4	Di-photon vertex reconstruction	39
4.1	Data 2017	39
4.1.1	Photon pointing	39
4.1.2	Calorimeter pointing	40
4.2	Data 2022	44
5	ToF vertex reconstruction	47
5.1	Time delays correction	48
5.2	Vertex matching	53
6	Future applications on an ALP search	57
7	Conclusions	59
	Bibliography	61
	Acronyms	65

List of Figures

1.1	Feynman diagram illustrating Axion-like particle (ALP) mediated light-by-light scattering in process of central exclusive di-photons production.	2
2.1	Cut-away view of the A Toroidal LHC ApparatuS (ATLAS) detector.	3
2.2	ATLAS Forward Proton (AFP) design.	4
2.3	Time-of-Flight (ToF) LQ-bar design. Vertical \times Horizontal \times Depth.	5
2.4	AFP Silicon pixel Tracker (SiT) and ToF LQ-bars. Proton beam comes from the right side.	6
3.1	Correlation of SiT versus ToF in run 429142 for C-side. Horizontal axis stands for the ToF trains, vertical axis stands for the x-position in the SiT in mm.	8
3.2	Raw time distribution before (left) and after (right) additional cuts on time were applied.	9
3.3	Raw time distributions in run 429142 after the cut on the time for train 3 for each channel: A (top left), B (top right), C (bottom left) and D (bottom right).	10
3.4	Raw time distributions in run 435229 after the cut on the time for train 3 for each channel: A (top left), B (top right), C (bottom left) and D (bottom right).	10
3.5	Raw time distributions in run 429142 separately for each side: A-side(left) and C-side(right).	11
3.6	Δt distributions for the run 429142 with a single Gaussian fitted curve overlaid for 2 combinations (AD - left, BC - right) of the ToF channels in train 0 for A-side (top) and C-side (bottom).	12
3.7	Δt distributions for the run 429142 with a single Gaussian fitted curve overlaid for 2 combinations (AD - left, BD - right) of the ToF channels in train 1 for A-side (top) and C-side (bottom).	12
3.8	Δt distributions for the run 429142 with a single Gaussian fitted curve overlaid for 2 combinations (AC - left, BC - right) of the ToF channels in train 2 for A-side (top) and C-side (bottom). Right distributions show large data fluctuations.	13

3.9	Δt distributions for the run 429142 with a single Gaussian fitted curve overlaid for 2 combinations (AD - left, CD - right) of the ToF channels in train 3 for A-side (top) and C-side (bottom).	13
3.10	Fit for the run 429142, a single Gaussian case, for A-side.	14
3.11	Fit for the run 429142, a single Gaussian case, for C-side.	15
3.12	Δt distributions for the run 429142 with a double Gaussian fitted curve overlaid for 2 combinations (AD - left, BC - right) of the ToF channels in train 0 for A-side (top) and C-side (bottom).	16
3.13	Δt distributions for the run 429142 with a double Gaussian fitted curve overlaid for 2 combinations (AD - left, BD - right) of the ToF channels in train 1 for A-side (top) and C-side (bottom).	16
3.14	Δt distributions for the run 429142 with a double Gaussian fitted curve overlaid for 2 combinations (AC - left, BC - right) of the ToF channels in train 2 for A-side (top) and C-side (bottom). Right distributions show large data fluctuations.	17
3.15	Δt distributions for the run 429142 with a double Gaussian fitted curve overlaid for 2 combinations (AD - left, CD - right) of the ToF channels in train 3 for A-side (top) and C-side (bottom).	17
3.16	Fit for the run 429142, a double Gaussian case, for A-side.	18
3.17	Fit for the run 429142, a double Gaussian case, for C-side.	19
3.18	Δt distributions for the run 435229 with a double Gaussian fitted curve overlaid for 2 combinations (AD - left, BC - right) of the ToF channels in train 0 for A-side (top) and C-side (bottom).	20
3.19	Δt distributions for the run 435229 with a double Gaussian fitted curve overlaid for 2 combinations (AD - left, BD - right) of the ToF channels in train 1 for A-side (top) and C-side (bottom).	21
3.20	Δt distributions for the run 435229 with a double Gaussian fitted curve overlaid for 2 combinations (AC - left, BC - right) of the ToF channels in train 2 for A-side (top) and C-side (bottom). Right distributions show large data fluctuations.	21
3.21	Δt distributions for the run 435229 with a double Gaussian fitted curve overlaid for 2 combinations (AD - left, CD - right) of the ToF channels in train 3 for A-side (top) and C-side (bottom).	22
3.22	Fit for the run 435229, a double Gaussian case, for A-side.	23
3.23	Fit for the run 435229, a double Gaussian case, for C-side.	23
3.24	Ratios, which define efficiencies for the run 429142, for the case of cuts "one train ON" for A-side for each train and one bar: 0B (top left), 1B (top right), 2B (bottom left) and 3B (bottom right).	26
3.25	Ratios, which defines efficiencies for the run 429142, for the case of cuts "one train OFF" for A-side for each train and one bar: 0B (top left), 1B (top right), 2B (bottom left) and 3B (bottom right).	26

3.26	Efficiencies (%) for the run 429142 for each channel of ToF for A (left) and C (right) sides with the optional requirement ON, (top) and OFF, (bottom) for the "histogram" method.	27
3.27	Efficiencies (%) for the run 429142 for each channel of ToF for A (left) and C (right) sides with the optional requirement ON, (top) and OFF, (bottom) for the "direct numbers" method.	28
3.28	Efficiencies (%) for the run 435229 for each channel of ToF for A (left) and C (right) sides with the optional requirement ON, (top) and OFF, (bottom) for the "direct numbers" method.	29
3.29	Efficiencies (%) for the run 429142 for each channel of the ToF with track pointing to train 0 for A (left) and C (right) sides with the optional requirement ON, (top) and OFF, (bottom) for the "direct numbers" method.	30
3.30	Efficiencies (%) for the run 429142 for each channel of the ToF with track pointing to train 1 for A (left) and C (right) sides with the optional requirement ON, (top) and OFF, (bottom) for the "direct numbers" method.	31
3.31	Efficiencies (%) for the run 429142 for each channel of the ToF with track pointing to train 2 for A (left) and C (right) sides with the optional requirement ON, (top) and OFF, (bottom) for the "direct numbers" method.	32
3.32	Efficiencies (%) for the run 429142 for each channel of the ToF with track pointing to train 3 for A (left) and C (right) sides with the optional requirement ON, (top) and OFF, (bottom) for the "direct numbers" method.	33
3.33	Efficiencies (%) for the low- μ run 435229 for each channel of the ToF with track pointing to train 0 for A (left) and C (right) sides with the optional requirement ON, (top) and OFF, (bottom) for the "direct numbers" method.	34
3.34	Efficiencies (%) for the low- μ run 435229 for each channel of the ToF with track pointing to train 1 for A (left) and C (right) sides with the optional requirement ON, (top) and OFF, (bottom) for "direct numbers" method.	35
3.35	Efficiencies (%) for the low- μ run 435229 for each channel of the ToF with track pointing to train 2 for A (left) and C (right) sides with the optional requirement ON, (top) and OFF, (bottom) for the "direct numbers" method.	36
3.36	Efficiencies (%) for the low- μ run 435229 for each channel of the ToF with track pointing to train 3 for A (left) and C (right) sides with the optional requirement ON, (top) and OFF, (bottom) for the "direct numbers" method.	37
4.1	Resolutions using the photon pointing method for converted (left) and unconverted (right) photons for different ALP masses in simulated signal events.	40

4.2	Widths (FWHM - Full Width Half Maximum) of resolutions in mm using photon pointing method for converted (left) and unconverted (right) photons as a function of ALP mass in simulated signal events.	40
4.3	Resolutions using calorimeter pointing method for converted (left) and unconverted (right) photons for different masses of ALP in simulated signal events.	41
4.4	Widths (FWHM - Full Width Half Maximum) of resolutions in mm using calorimeter pointing method for converted (left) and unconverted (right) photons as a function of ALP mass in simulated signal events.	41
4.5	Resolutions using the calorimeter pointing method for different 2017 data sets (DS). The values, z_0 and z_1 , correspond to the z -position of the leading and the sub-leading photons, respectively.	42
4.6	Widths (FWHM - Full Width Half Maximum) of the resolutions in mm using the calorimeter pointing method for different 2017 data sets.	42
4.7	Compared resolutions for converted (left) and unconverted (right) photons for simulated events and recorded data using the calorimeter pointing method.	43
4.8	Resolutions for converted (left) and unconverted (right) photons for first Run-3 data from 2022 using the calorimeter pointing method with fitted curve overlaid. The values, z_0 and z_1 , correspond to the z -position of the leading and the sub-leading photons, respectively.	45
5.1	$z_{\text{ToF}} - z_{\text{BS}}$ distributions for the run 429142 with a Gaussian fitted curve overlaid for 2 combinations of the ToF channels. Left - side A 0A (train 0, bar A) with side C 1B (train 1, bar B). Right - side A 2B (train 2, bar B) with side C 0D (train 0, bar D).	49
5.2	$z_{\text{ToF}} - z_{\text{BS}}$ distributions for the low- μ run 435229 with Gaussian fitted curve overlaid for 2 combinations of the ToF channels. Left - side A 0A (train 0, bar A) with side C 1B (train 1, bar B). Right - side A 2B (train 2, bar B) with side C 0D (train 0, bar D).	49
5.3	All differences between delay correction constants for each of the 256 combinations of the ToF channels for the run 429142 (left) and for the low- μ run 435229 (right).	50
5.4	All differences between delay correction constants for each of the 256 combinations of the ToF channels with fit overlaid for the run 429142 (left) and for the low- μ run 435229 (right).	51
5.5	Delay correction constants for all ToF channels on A-side (top) and C-side (bottom) for the run 429142 (left) and for the low- μ run 435229 (right).	51

5.6	Dependence of the z_{BS} and z_{ToF} per lumiblock (LB) before (top) and after (bottom) the corrections on time delays for the run 429142 (left) and for the low- μ run 435229 (right).	52
5.7	Dependence of the z_{BS} and z_{ToF} per LB after the corrections on time delays for the run 429142 (left) and for the low- μ run 435229 (right), magnified version.	53
5.8	The distribution of the $z_{\text{ATLAS}} - z_{\text{ToF}}$ for the low- μ run 435229.	54
5.9	The distribution of the $z_{\text{ATLAS}} - z_{\text{ToF}}$ for the low- μ run 435229 excluding train 2.	54
5.10	The distribution of $z_{\text{ATLAS}} - z_{\text{ToF}}$ measured in events with ToF signals on both sides of the interaction region in run 341419 in data 2017, where z_{ATLAS} is the primary vertex z -position reconstructed by ATLAS. The z_{ToF} is obtained as $z_{\text{ToF}} = -\frac{c}{2}\Delta t$, where Δt is the time difference of proton arrival times in A and C far stations of the AFP measured by ToF. The distribution correspond to the ATLAS data containing a reconstructed primary vertex together with coincidence of signals in both ToF detectors in scenario with no cut on number of vertices reconstructed by ATLAS. A double Gaussian function representing the signal and background components is fitted to unbinned data samples using the extended likelihood fit as implemented in RooFit. The mean of the signal component as well as the mean and width of the background component are always estimated from a Gaussian fit to the mixed event data, denoted as μ_{sig}^{FIX} , μ_{bgd}^{FIX} and σ_{bgd}^{FIX} . The mixed event data $z_{\text{ATLAS}} - z_{\text{ToF}}$ distributions are obtained by random mixing of times measured by ToF in either station and the z_{ATLAS} values which do not originate in the same collision event. The expected resolution of the ToF detector, quoted as $\sigma_{expected}^{ToF}$ is obtained from the known single-channel resolutions convoluted with the actual channel-hit-patterns observed in the data [18].	56

List of Tables

3.1	Width of Δt (ps) distributions for the run 429142 using a single Gaussian fit for all combinations of the ToF channels inside one train. Trains: 0-1, bars: A-D.	14
3.2	ToF time resolution (ps) for the run 429142, a single Gaussian case. Trains: 0-1, bars: A-D.	15
3.3	Width of Δt (ps) distributions for the run 429142 using a double Gaussian fit for all combinations of the ToF channels inside one train. Trains: 0-1, bars: A-D.	18
3.4	ToF time resolution (ps) for the run 429142, a double Gaussian case. Trains: 0-1, bars: A-D.	19
3.5	Width of Δt (ps) distributions for the run 435229 using a double Gaussian fit for all combinations of the ToF channels inside one train. Trains: 0-1, bars: A-D.	22
3.6	ToF time resolution (ps) for the run 435229, a double Gaussian case. Trains: 0-1, bars: A-D.	24
3.7	Regions for the x-value of the SiT, corresponding to the ToF trains.	25
4.1	Width (mm) of resolutions using photon and calorimeter pointing methods for different ALP masses.	43
4.2	Rejection factors and sensitivity for converted and unconverted photons for 3 regions ($\pm 1\sigma$, $\pm 2\sigma$, $\pm 3\sigma$). Sens (sensitivity) = $\text{signal}/\sqrt{\text{background}}$	44

Chapter 1

Introduction

Many extensions of the Standard Model (SM) use Axions and Axion-like particles (ALPs), which are considered as candidates for particles that make up missing matter, the so-called dark matter [1, 2]. The ALPs are hypothetical particles with spin 0, which, according to some predictions, can explain the lack of Charge conjugation times Parity (CP) violation in quantum chromodynamics [3]. Usually, ALPs couple to fermions only through dimension-five operators proportional to fermion mass. Moreover, (pseudo) scalars predominantly couple to gauge bosons through dimension-five operators containing derivatives [4]. Thus, in energy regimes exceeding the top quark mass, ALPs are only accessible through their coupling to the gauge bosons and the Higgs boson. They can be formed in different processes.

At the Large Hadron Collider (LHC) [5], the electromagnetic fields between protons are strong enough to create strong fluxes of high-energy virtual photons. These photons can interact, for example, by merging together, after which the product can decay into various final states. Photon fusion is a distinctive way of looking for physics Beyond the Standard Model (BSM), as only electromagnetic coupling needs to be considered. This search is therefore independent of the strong and weak coupling forces on which most other LHC searches are based. High-precision measurements of these types of Quantum Electrodynamics (QED) processes can set limits on various theories, and any non-coincidence with SM can indicate the presence of new physics [6].

Light-by-light scattering is an important process that can occur as described above. Scattering of light by light mediated by ALPs is prohibited in the classical theory of electrodynamics [7]. In various extensions, additional contributions are possible, which makes light-by-light scattering measurements sensitive to physics BSM, which can be used to search for Axion-like particles [8, 4].

In this study, the main focus is on the process of central exclusive di-photon production $pp \rightarrow p(\gamma\gamma)p$, which is shown in Figure 1.1.

These di-photon events can be recorded with the ATLAS central detector. The vertex position of di-photons is used as a criteria to separate di-photon

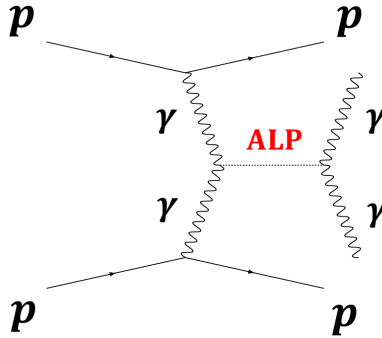


Figure 1.1: Feynman diagram illustrating ALP mediated light-by-light scattering in process of central exclusive di-photons production.

events coming from an ALP signal from di-photon events produced in other background processes. Therefore, an improved di-photon vertex resolution will contribute to better separation of signal and background events.

The ATLAS Forward Proton (AFP) detector [9] is designed to measure trajectories of the leading protons far from an interaction point. After passing through the LHC magnet system, these protons may deviate from the nominal proton beam to such an extent that their deviations can be measured. The two AFP stations are located approximately 210 m on either side of the ATLAS interaction area. The AFP detectors are placed in the so-called Roman Pots (RP). They allow sensitive detectors to be placed close to the beam while maintaining vacuum in the primary beam tube. Position of the deflected protons is measured by the SiT. The forward detector is a useful tool for improvement of the background reduction [10, 11].

The two AFP FAR stations are equipped with the ToF detector. The initial time-of-flight detector performance is determined using early 2022 data. In particular, the detection efficiency and resolution of time measurements in individual channels of the ToF detector are evaluated.

Additionally, the ToF detector can provide data to improve the vertex reconstruction, in particular for di-photon events, as the photon reconstruction uses calorimeters at a large distance from the interaction point. After applying a calibration, with the ToF data, the vertex reconstruction resolution is determined.

Chapter 2

Detector design

2.1 ATLAS Central Detector

The ATLAS (A Toroidal LHC ApparatuS) detector [12] is one of the experiments at the LHC and is a general purpose detector that covers almost the entire solid angle around the interaction point. It is nominally forward-backward symmetric with respect to the interaction point, having dimensions of 25 m in height, 44 m in length and a weight of approximately 7000 tonnes. The brief scheme of the detector is given in Figure 2.1.

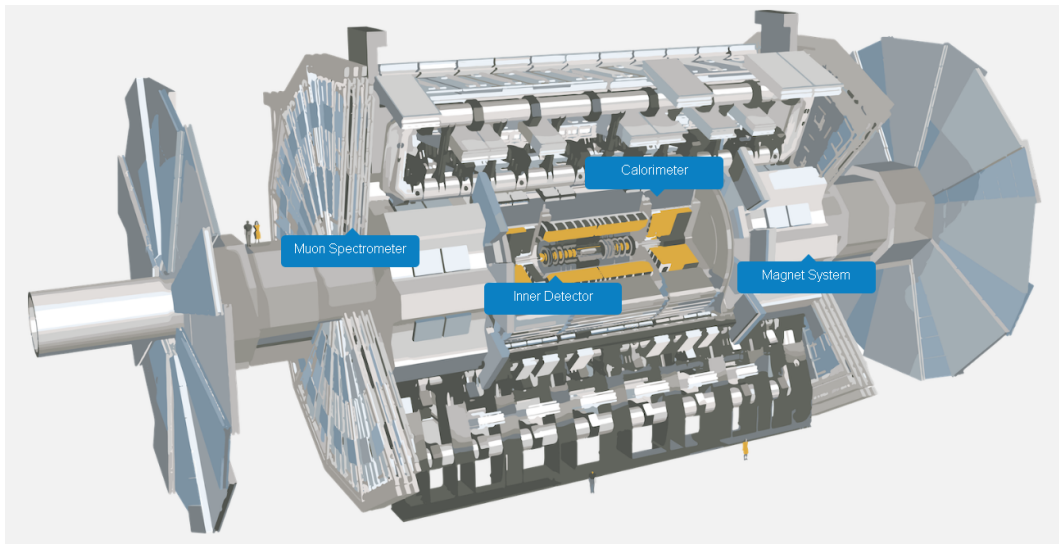


Figure 2.1: Cut-away view of the ATLAS detector.

The central detector consists of 4 layers: the inner detector, the electromagnetic and hadronic calorimeters, and the muon spectrometer.

The inner detector is used to track charged particles in the pseudorapidity region of $|\eta| < 2.5$. It is immersed in a 2 T solenoidal magnetic field. Combination of the inner (discrete high-resolution semiconductor pixel and

strip detectors) and the outer (straw-tube detectors, which can detect transition radiation) parts of the tracking volume are used for momentum and vertex measurements, electron identification, and pattern recognition.

Electromagnetic calorimeter is provided by a high granularity liquid-argon calorimeter and cover the pseudorapidity region of $|\eta| < 3.2$.

The hadronic calorimeter is provided by a scintillator-like calorimeter and cover the range of $|\eta| < 1.7$. Both electromagnetic and hadron energy measurements are taken by the liquid-argon forward calorimeters, they extend pseudorapidity acceptance to the $|\eta| < 4.9$.

The calorimeters are surrounded by the muon spectrometer, which uses high precision tracking chambers and covers regions of $|\eta| < 2.7$. In addition, forward calorimeters cover the region of $3.2 < |\eta| < 4.9$. The ATLAS Forward Proton detectors are described in the next Section 2.2.

2.2 ATLAS Forward Proton Detector

The AFP detector consists of four stations, which are located at around 205 m and 217 m - NEAR and FAR stations, on anticlockwise (A) and clockwise (C) sides of the ATLAS interaction region. A plan view of the detector is presented in Figure 2.2.

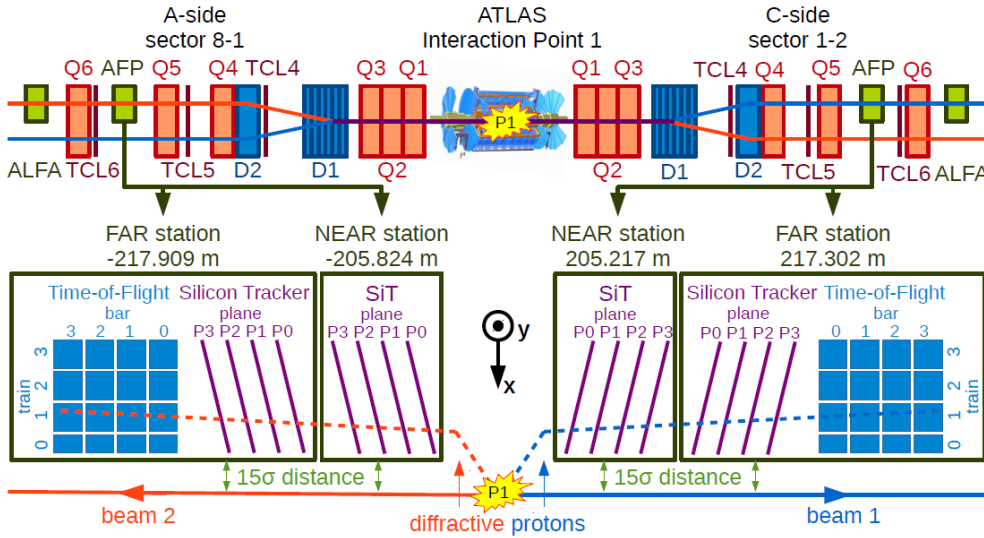


Figure 2.2: AFP design.

The FAR stations are the only ones equipped with the ToF detectors, and therefore only data from them are the subject of this study. In this section only a brief description of the design and function of the AFP and ToF are given, for more detail see [9].

For tracking the SiT is used, which consists of four layers of silicon pixel detectors. The active area of the detector is approximately $20 \times 20 \text{ mm}^2$, the

pixel size is $50 \times 250 \mu\text{m}^2$ and they form a pixel grid with a size of 336 by 80 pixels on each SiT plane. The planes of SiT are tilted by 14° providing a spatial resolution of the $10 \mu\text{m}$ in x and $30 \mu\text{m}$ in y , as measured in beam tests [13].

2.3 Time-of-Flight Detector

The ToF detectors collect Cherenkov photons created in L-shaped fused silica [14] bars (LQ-bars), which are placed behind the tracker plates. Details of the design are given in [15], only a brief description is provided here. The geometry of the ToF detector was designed to optimize light yield given the space constraints of the Roman Pot stations. The LQ-bar consists of two arms: a radiator arm exposed to beam protons and a light guide arm. The elbow presents an Al-mirror and a taper cut to achieve better focusing of the Cherenkov photons (Figure 2.3).

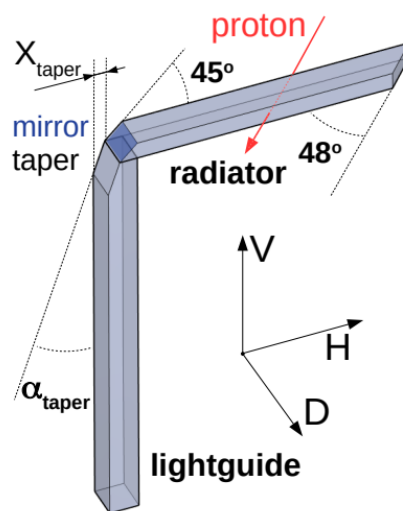


Figure 2.3: ToF LQ-bar design. Vertical \times Horizontal \times Depth.

Photons emitted along a proton trajectory inside the radiator arm propagate to the light-guide arm and to the end of the bars which is attached to a photo-multiplier. To minimize the number of total reflections, the radiator arms are tilted under the Cherenkov angle of 48° with respect to the beam axis, which leads to the optimization of the time needed for light propagation through the bar. To reflect downwards emitted photons back to the bar, the trailing ends of the radiators are cut parallel to the beam axis. Four bars are placed one after another to form a train. There are four trains on each side. The bars and the corresponding channels are denoted as A, B, C, D (or 0 – 3), bar A being the first one to be crossed by protons. Each ToF detector consists of four trains numbered from 0 to 3, 0 being the closest to the beam.

The geometry of the bars is such that the optical path in all bars is equalized. Figure 2.4 shows the design of the assembled LQ bars and SiT mounted on the Roman Pot flange. Proton beam is going through the system, passing firstly through the SiT, and then through the ToF, in this example proton beam is coming from the right side. The direction of the X-axis is up.

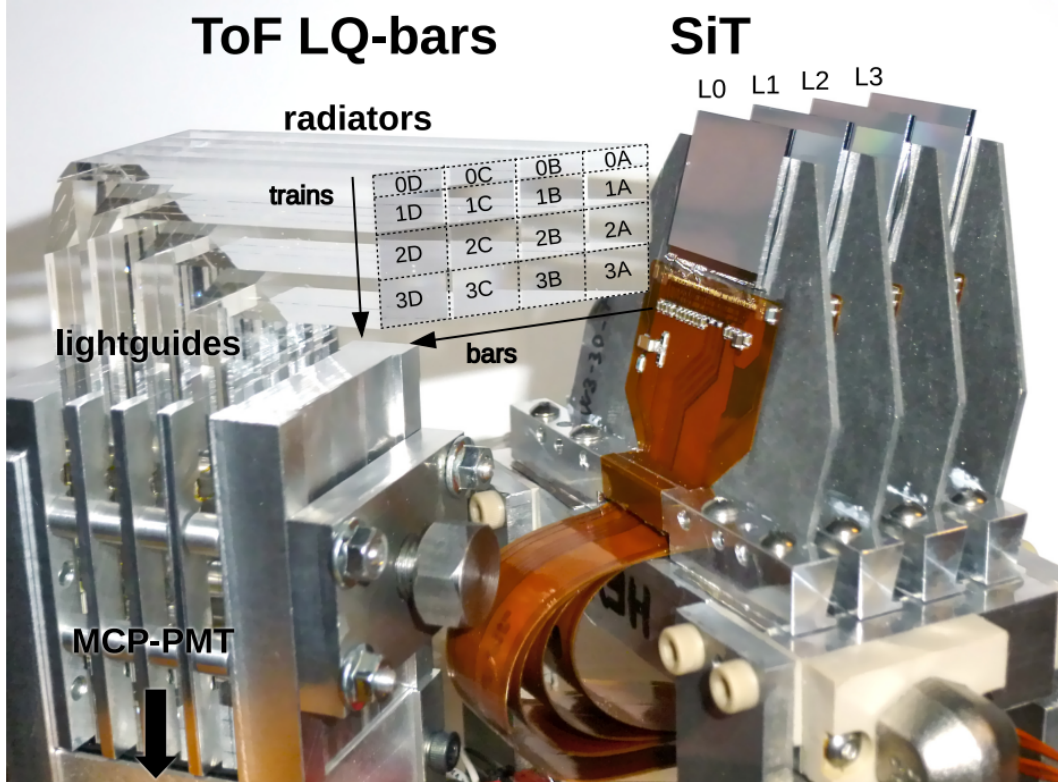


Figure 2.4: AFP SiT and ToF LQ-bars. Proton beam comes from the right side.

The Cherenkov photon statistics translates to the number of photo-electrons via the quantum efficiency of the Photomultiplier Tube (PMT) photo-cathode. The number of photo-electrons is amplified by the high voltage applied to the micro-channel plates of the PMTs. The voltage pulses from the PMT anodes are amplified and processed by a constant fraction discriminator (CFD) [16] providing a square signal for a high performance time-to-digital converter (HPTDC) [17]. The signals are sampled in 1024 bins of about 25 ns time window which corresponds to the LHC bunch spacing. The overall time resolution of the detector is therefore affected at several stages during the formation of the signal and its read-out in the front-end electronics [18].

Chapter 3

First analysis of the ToF detector with LHC Run-3 Data

3.1 Data selection

For the resolution and the efficiency analyses, two runs were chosen, namely 429142 and 435229. These runs have a clear step-like structure in the correlation SiT versus ToF data (Figure 3.1), which is required to identify a run that can be used in such a study.

Run 429142 data was collected on July 25, 2022, with CFD [16] thresholds set to 250 mV and corresponds to an ATLAS integrated luminosity of 39.77 pb⁻¹ from the general integrated luminosity of 44.42 pb⁻¹. The average pile-up (number of pp collisions in the same beam crossing) for this run was 37.5.

Run 435229 was the longest run by the time of this analysis, its duration was 2 days and 20 hours, starting on September 23, 2022. For comparison, duration of the run 429142 was 7 hours. It was a special Large Hadron Collider forward (LHCf) [19] run with extremely low average pile-up, which was 0.02 (low- μ run). Data was collected with CFD [16] thresholds set to 250 mV and corresponds to an ATLAS integrated luminosity of 146.9 nb⁻¹ from the general integrated luminosity of 157.7 nb⁻¹. In the analysis only the first half of the run is used, as at the time of this work only this half was available for study.

The pre-processing of the data includes the correction of the channel map and creating n-tuples from Analysis Object Data (AOD) [20] on the grid.

Before obtaining the resolutions and efficiencies, some general requirements on the data sample were applied:

- One track in the SiT per event.
- At most one cluster per plane in the SiT per event.

Additionally two more requirements were used:

- One active train in the ToF per event.
- A cut on measured ToF arriving time period.

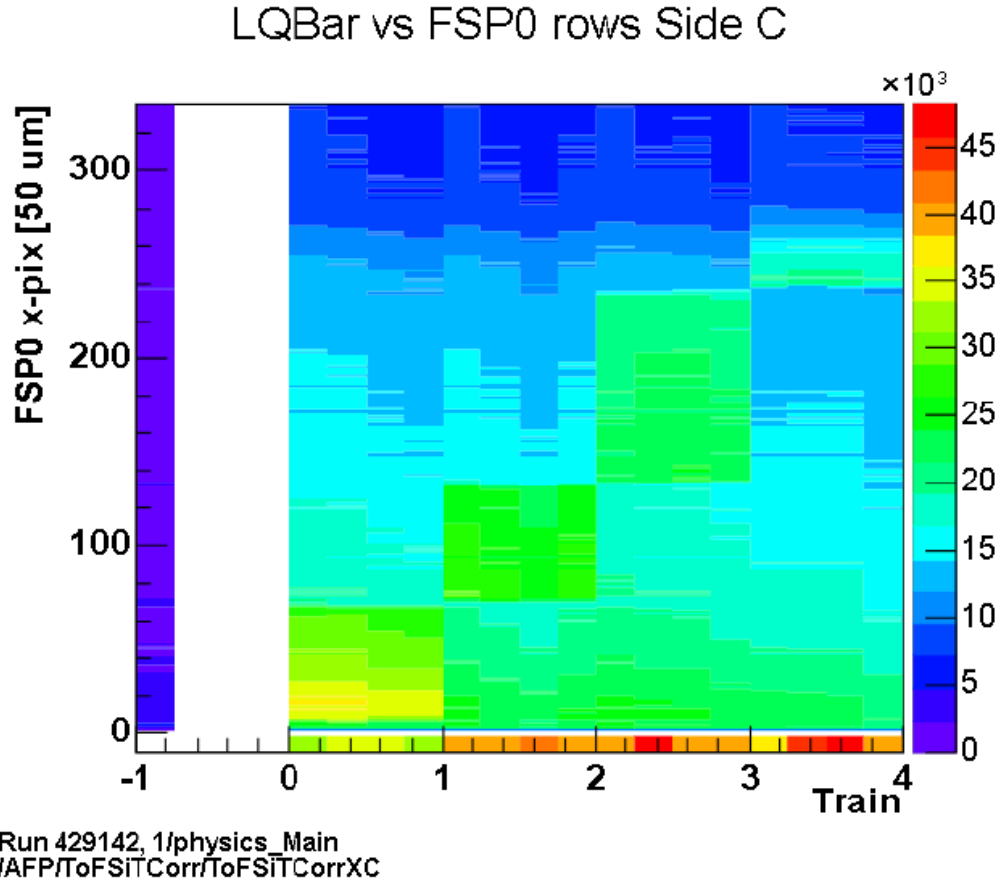


Figure 3.1: Correlation of SiT versus ToF in run 429142 for C-side. Horizontal axis stands for the ToF trains, vertical axis stands for the x-position in the SiT in mm.

3.2 Time resolution

The HPTDC [17] measures the time in terms of one of the 1024 raw time bin numbers within a 25 ns time window of LHC collisions.

The time stored in the AOD [20] is in nanoseconds although it is an uncalibrated HPTDC output (raw time). A HPTDC calibration following the 2017 data analysis [18] is to be performed later. The raw time in terms of one of the 1024 HPTDC bin numbers (0 .. 1023) is translated to nanoseconds by

$$\text{time[ns]} = \text{rawbin} \times 25[\text{ns}]/1024.$$

The 25 ns correspond to the 40 MHz LHC frequency.

In raw time distributions small modulations are seen near the main peaks. This is caused by slower or faster protons spilling to the Radiofrequency (RF) buckets [21] that demarcate the times of circulating protons in the LHC. One RF bucket is 2.5 ns long. This is the frequency used by the RF cavities to accelerate the beam. The RF buckets are so small in order to make the beam more intense, and only one of ten is used for better bunch separation. These

modulations were cleaned to obtain better resolution. This is one of the additional requirements (a cut on measured ToF arriving time period), mentioned before.

Figure 3.2 shows the raw time distribution before and after this additional requirement for only one channel in run 429142 (0A - train 0, bar A), as an example. Such distributions were created for each ToF channel in both runs. The left peak corresponds to the C-side and the right one to the A-side, so they are both plotted on the same histogram.

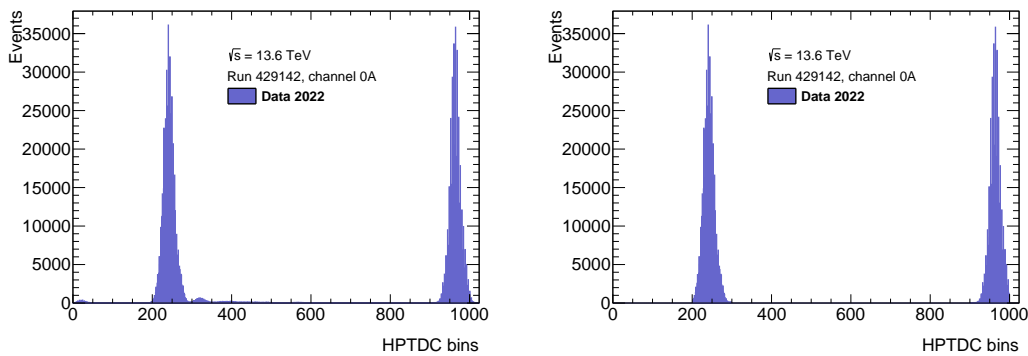


Figure 3.2: Raw time distribution before (left) and after (right) additional cuts on time were applied.

Figures 3.3 (run 429142) and 3.4 (run 435229) show the raw time distributions after cleaning the sample, focusing on the main peak. The double-peak structure is observed only in train 3 in both runs. This could be a feature of the ToF construction. It is also possible that the readout is confused between bunch crossings¹.

¹as discussed at an ATLAS Combined Performance meeting

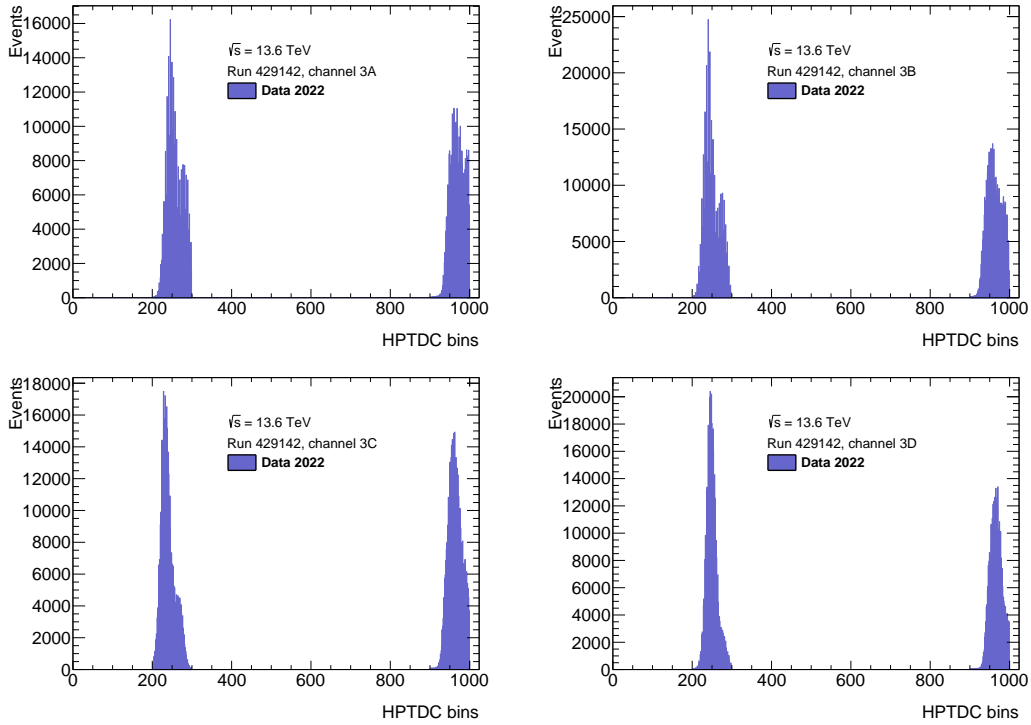


Figure 3.3: Raw time distributions in run 429142 after the cut on the time for train 3 for each channel: A (top left), B (top right), C (bottom left) and D (bottom right).

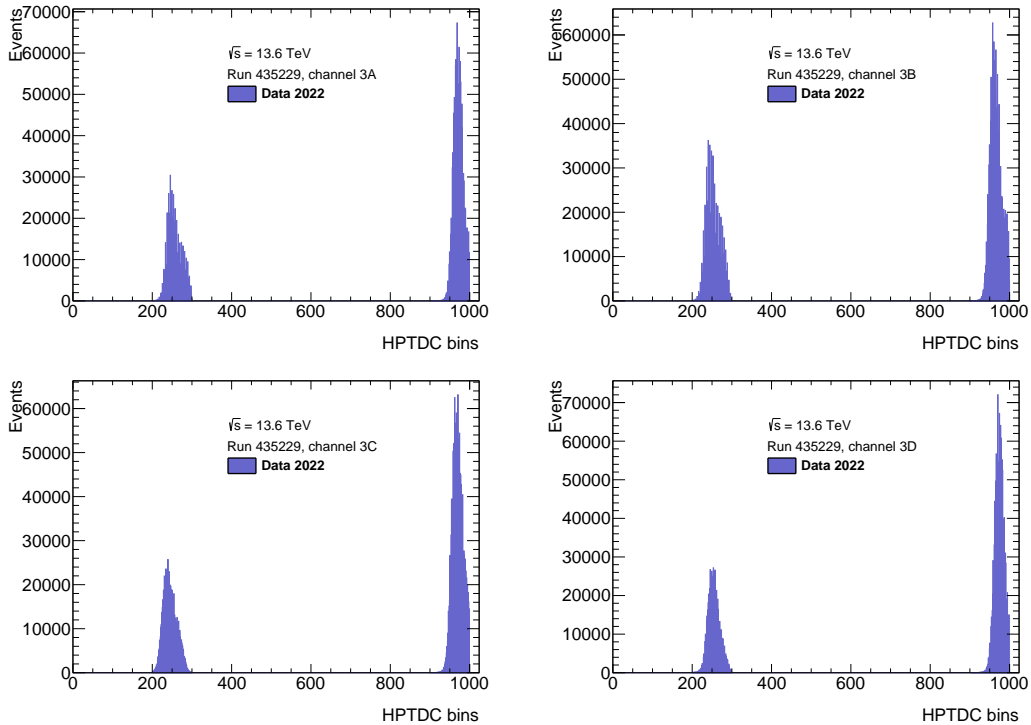


Figure 3.4: Raw time distributions in run 435229 after the cut on the time for train 3 for each channel: A (top left), B (top right), C (bottom left) and D (bottom right).

Figure 3.5 shows the raw time distributions separately for each side in run 429142. The effect of the HPTDC non-calibration can be seen as non-uniformity of the distributions.

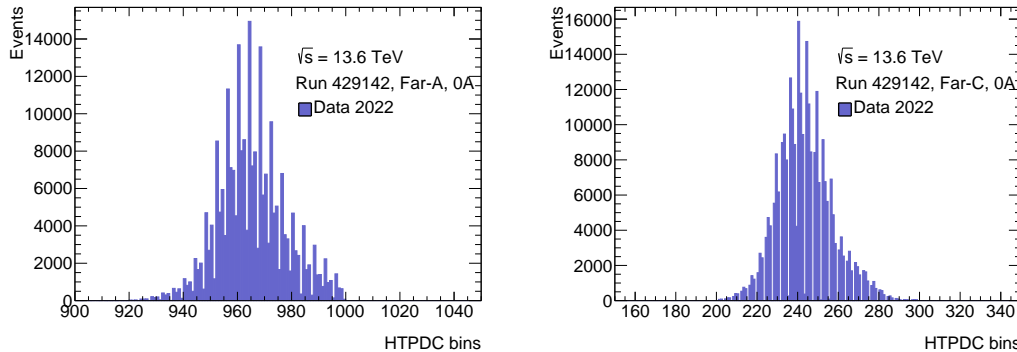


Figure 3.5: Raw time distributions in run 429142 separately for each side: A-side(left) and C-side(right).

The previous analysis with 2017 data [18] concluded that the HPTDC calibration does not affect much the time resolution. Thus, in this analysis, the calibration was not applied yet to obtain time resolutions.

The resolutions were obtained as single-channel resolutions for each channel of the ToF. The following requirements were imposed on the data:

- One track in the SiT per event.
- At most one cluster per plane in the SiT per event.
- Cut on measured ToF arriving time period.
- One active train in the ToF per event.

The widths of the Δt distributions will serve for the determination of the single-channel time resolutions. the Δt here stands for the difference of arrival times in two ToF channels, i and j . There are six Δt values, however, there are only four channels, thus the single-channel resolutions will be obtained using chi-squared minimization [18]. We assume no correlations, which requires a separate study, and set $\rho_{ij} = 0$.

$$\chi^2 = \sum_{ij} \frac{(\sigma_{ij} - \sqrt{\sigma_i^2 + \sigma_j^2 - 2\rho_{ij}\sigma_i\sigma_j})^2}{(\delta_{\text{fit}}(\sigma_{ij}))^2}, \quad (3.1)$$

The shapes of the distributions are not fully Gaussian, therefore these results assume a Gaussian approximation. Δt distributions for the run 429142 with a fitted curve overlaid to obtain the widths of the distributions are shown in Figures 3.6-3.9 for train 0 (3.6), train 1 (3.7), train 2 (3.8) and train 3 (3.9). All widths are listed in Table 3.1. Channel combinations are marked as, for example, 0AB, which means train 0, difference between bars A and B.

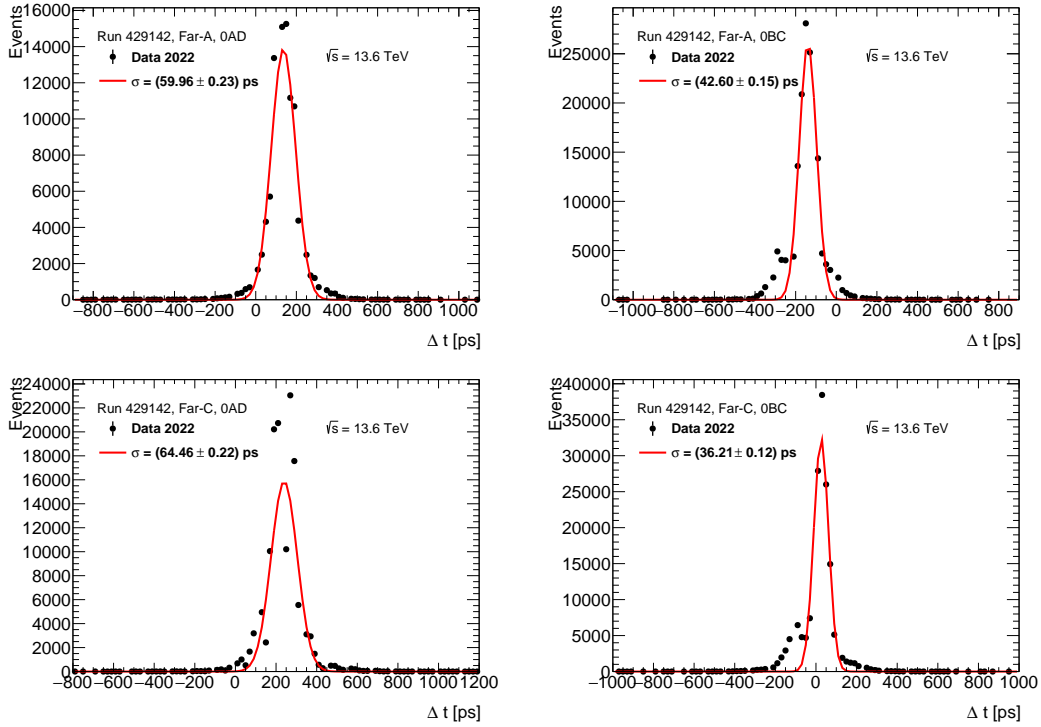


Figure 3.6: Δt distributions for the run 429142 with a single Gaussian fitted curve overlaid for 2 combinations (AD - left, BC - right) of the ToF channels in train 0 for A-side (top) and C-side (bottom).

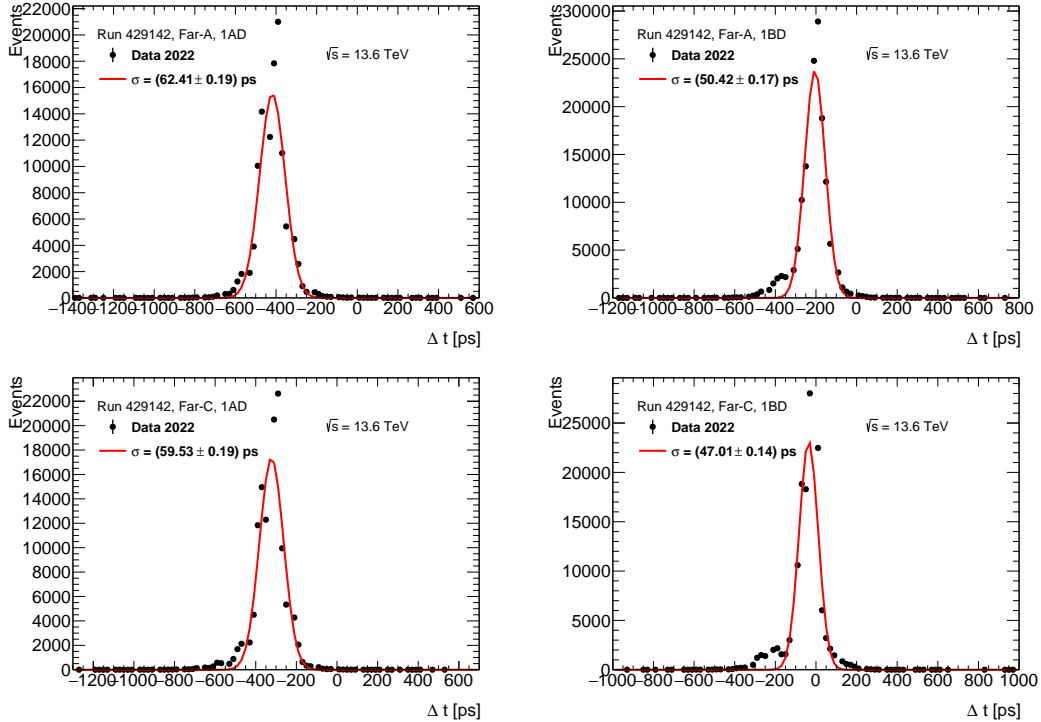


Figure 3.7: Δt distributions for the run 429142 with a single Gaussian fitted curve overlaid for 2 combinations (AD - left, BD - right) of the ToF channels in train 1 for A-side (top) and C-side (bottom).

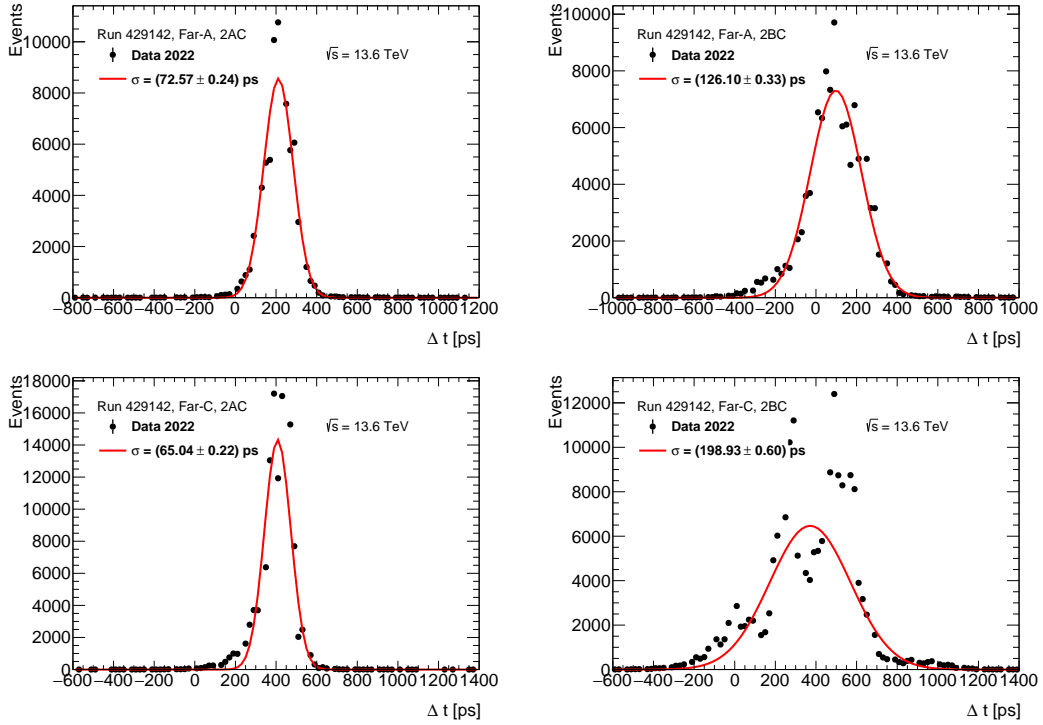


Figure 3.8: Δt distributions for the run 429142 with a single Gaussian fitted curve overlaid for 2 combinations (AC - left, BC - right) of the ToF channels in train 2 for A-side (top) and C-side (bottom). Right distributions show large data fluctuations.

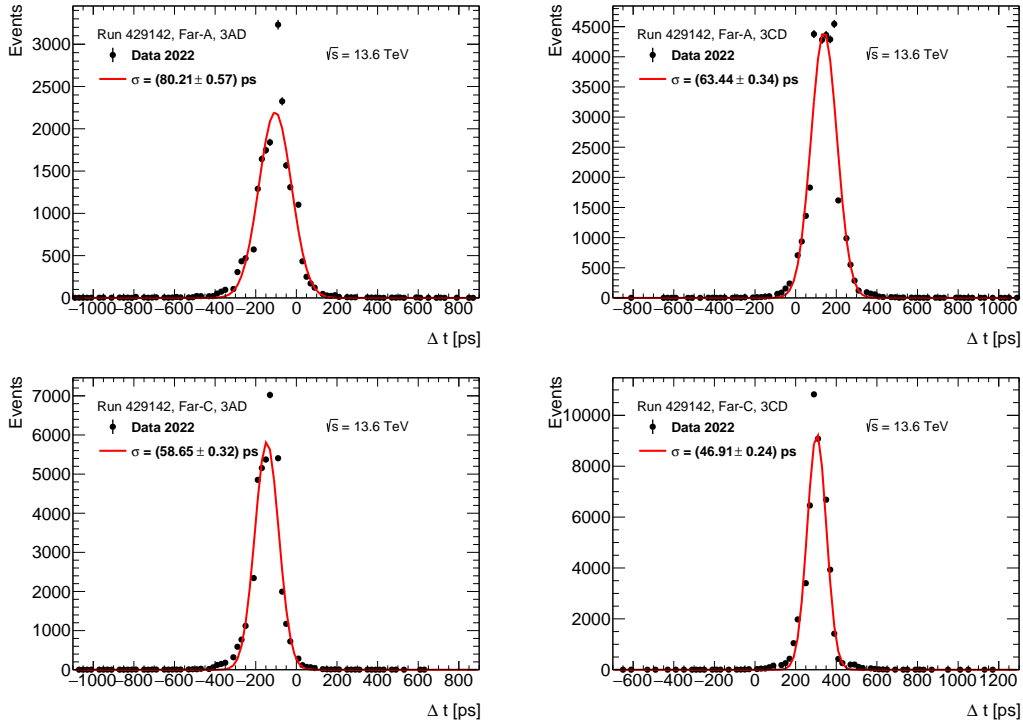


Figure 3.9: Δt distributions for the run 429142 with a single Gaussian fitted curve overlaid for 2 combinations (AD - left, CD - right) of the ToF channels in train 3 for A-side (top) and C-side (bottom).

A-side	AB	AC	AD	BC	BD	CD
0	40.45	45.90	59.96	42.60	50.82	58.41
1	62.06	60.62	62.41	44.50	50.42	42.26
2	84.19	72.57	86.79	126.10	161.22	66.39
3	66.16	116.46	80.21	88.44	84.81	63.44
C-side	AB	AC	AD	BC	BD	CD
0	38.49	50.16	64.46	36.21	51.29	66.42
1	58.14	57.77	59.53	37.61	47.01	39.96
2	100.30	65.04	58.45	198.93	238.43	56.96
3	59.43	55.36	58.65	47.65	56.70	46.91

Table 3.1: Width of Δt (ps) distributions for the run 429142 using a single Gaussian fit for all combinations of the ToF channels inside one train. Trains: 0-1, bars: A-D.

The resulting time resolutions for the run 429142 are given in Table 3.2, as determined from a chi-squared minimization fit of the six time differences for the four bars as previously proposed [18]. The χ^2 is defined in Equation 3.1 for $\rho_{ij} = 0$. Figures 3.10 and 3.11 show this fit for A and C sides, respectively, with channels combinations on X-axis in the same order as in Table 3.1 and widths of the Δt distributions on the Y-axis.

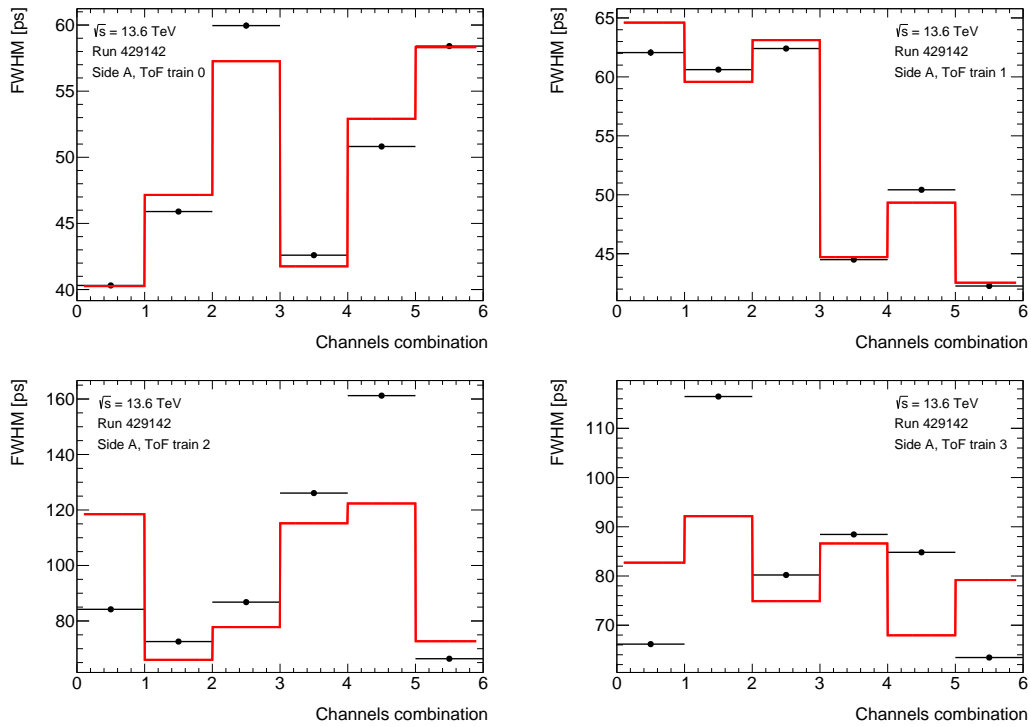


Figure 3.10: Fit for the run 429142, a single Gaussian case, for A-side.

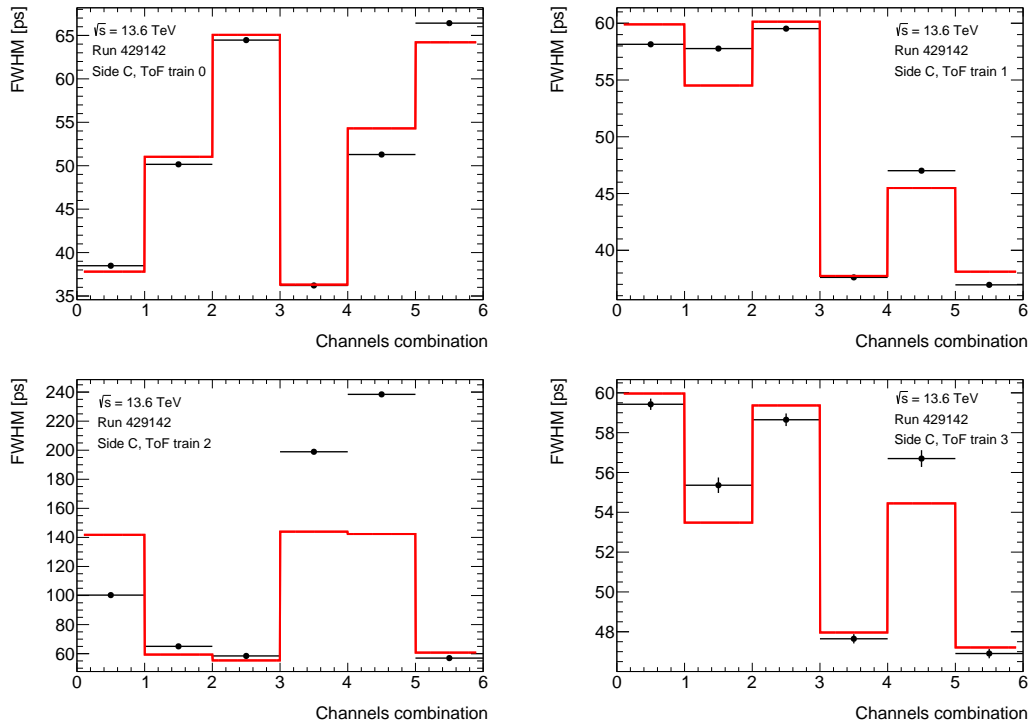


Figure 3.11: Fit for the run 429142, a single Gaussian case, for C-side.

A-side	A	B	C	D
0	32.41	23.88	34.24	47.21
1	53.49	36.21	26.22	33.49
2	50.59	107.13	42.35	59.08
3	62.57	54.08	67.65	41.14
C-side	A	B	C	D
0	36.84	84.83	35.30	53.63
1	50.67	31.94	20.10	32.38
2	38.09	136.55	45.54	40.16
3	45.58	38.96	27.97	38.03

Table 3.2: ToF time resolution (ps) for the run 429142, a single Gaussian case. Trains: 0-1, bars: A-D.

On the basis of the shapes of the Δt distributions a hypothesis of a double-Gaussian was put forward. To check this hypothesis, distributions were fitted using sum of two Gaussians. Δt distributions for the run 429142 with a fitted curve overlaid to obtain the widths of the distributions are shown in Figures 3.12-3.15 for train 0 (3.12), train 1 (3.13), train 2 (3.14) and train 3 (3.15). All widths are listed in Table 3.3.

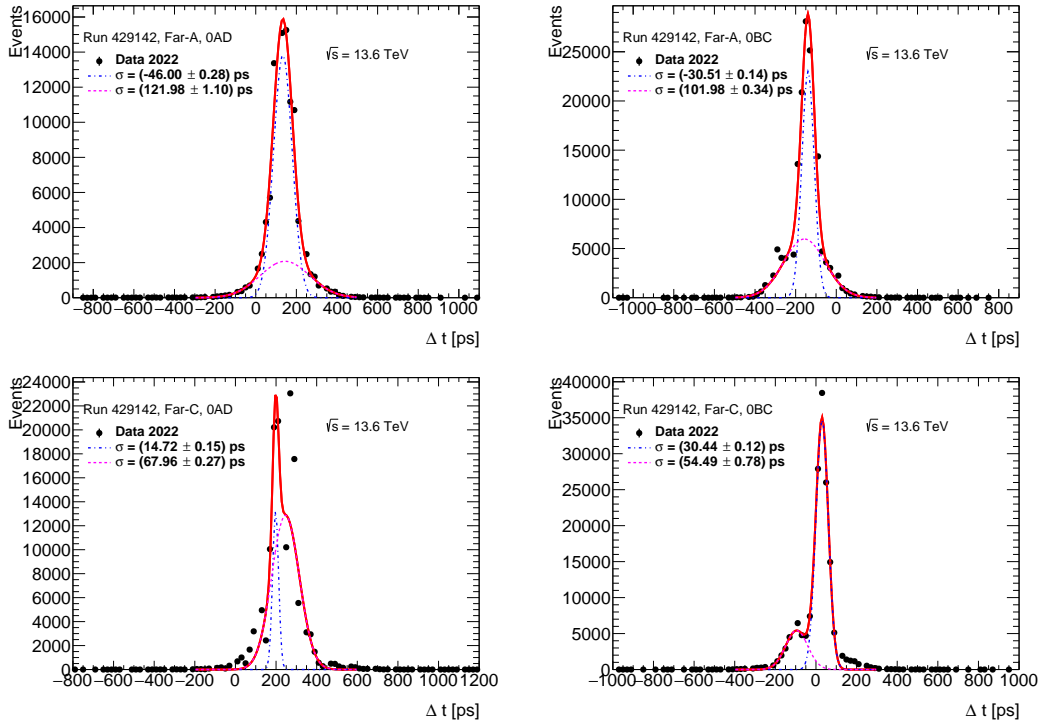


Figure 3.12: Δt distributions for the run 429142 with a double Gaussian fitted curve overlaid for 2 combinations (AD - left, BC - right) of the ToF channels in train 0 for A-side (top) and C-side (bottom).

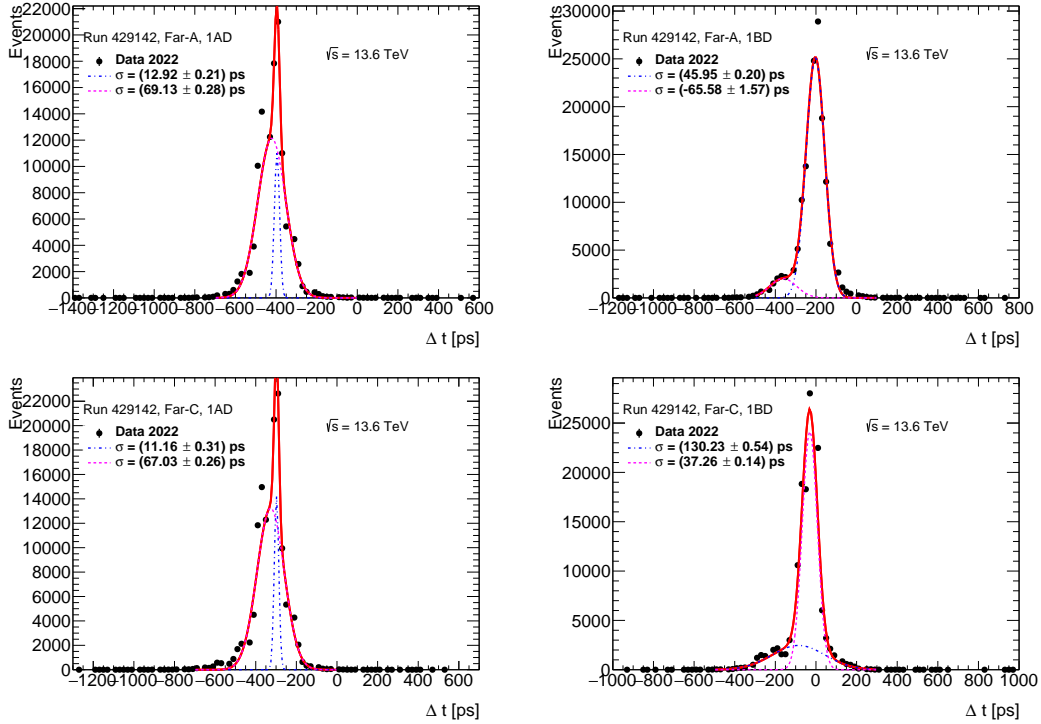


Figure 3.13: Δt distributions for the run 429142 with a double Gaussian fitted curve overlaid for 2 combinations (AD - left, BD - right) of the ToF channels in train 1 for A-side (top) and C-side (bottom).

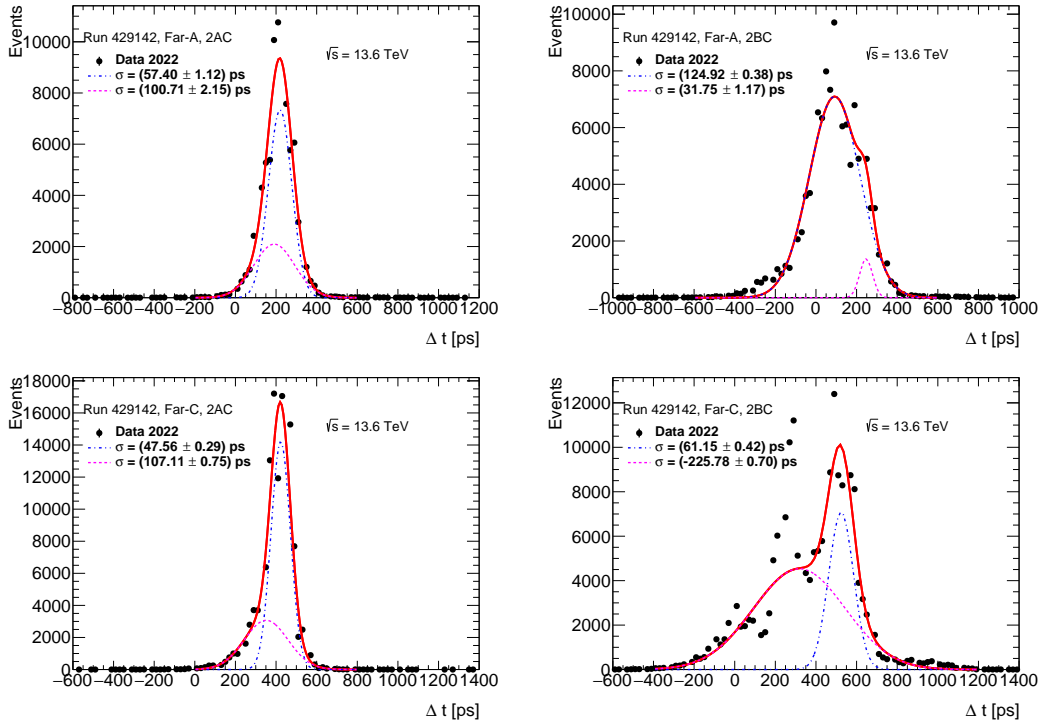


Figure 3.14: Δt distributions for the run 429142 with a double Gaussian fitted curve overlaid for 2 combinations (AC - left, BC - right) of the ToF channels in train 2 for A-side (top) and C-side (bottom). Right distributions show large data fluctuations.

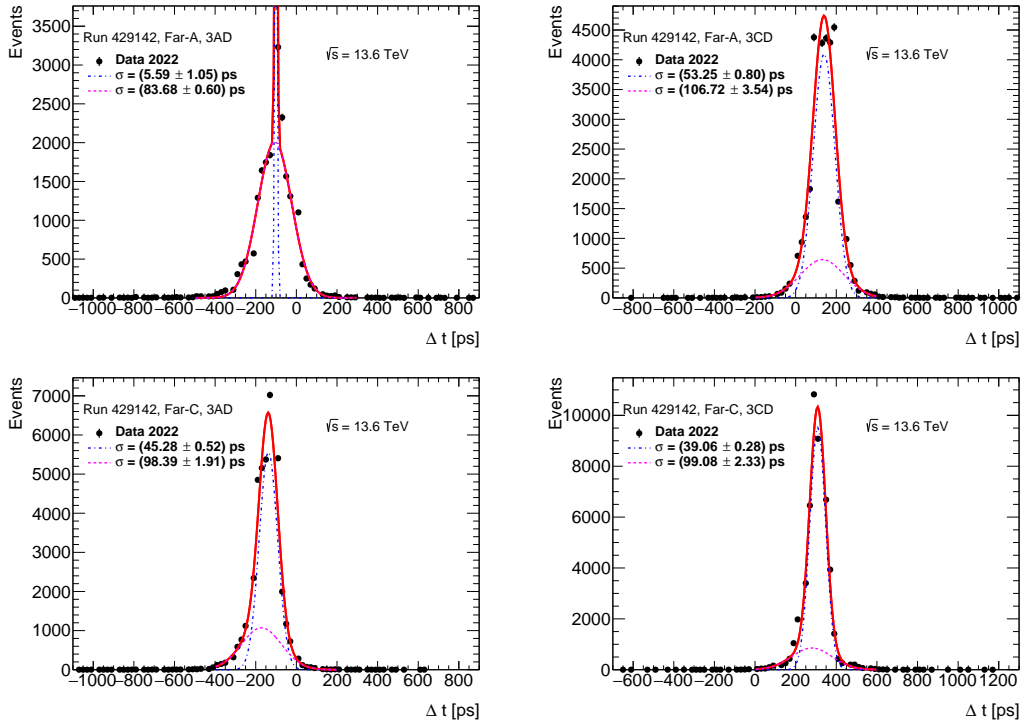


Figure 3.15: Δt distributions for the run 429142 with a double Gaussian fitted curve overlaid for 2 combinations (AD - left, CD - right) of the ToF channels in train 3 for A-side (top) and C-side (bottom).

A-side	AB	AC	AD	BC	BD	CD
0	33.01	42.49	46.00	30.51	48.01	47.60
1	42.42	59.61	69.13	31.11	45.95	37.09
2	74.70	57.40	59.37	124.92	157.35	62.80
3	69.36	77.63	83.68	81.86	80.28	53.25
C-side	AB	AC	AD	BC	BD	CD
0	32.30	40.51	67.96	30.44	46.49	79.14
1	63.94	24.22	67.03	30.86	37.26	27.31
2	104.67	47.56	45.64	61.15	84.00	50.11
3	50.61	42.49	45.28	28.44	30.11	39.06

Table 3.3: Width of Δt (ps) distributions for the run 429142 using a double Gaussian fit for all combinations of the ToF channels inside one train. Trains: 0-1, bars: A-D.

The resulting time resolutions for the run 429142 are given in Table 3.4, as determined from a fit of the six time differences for the four bars as previously proposed [18]. The χ^2 is defined in Equation 3.1 for $\rho_{ij} = 0$. Figures 3.16 and 3.17 show this fit for A and C sides, respectively, with channels combinations on X-axis in the same order as in Table 3.3 and widths of the Δt distributions on the Y-axis.

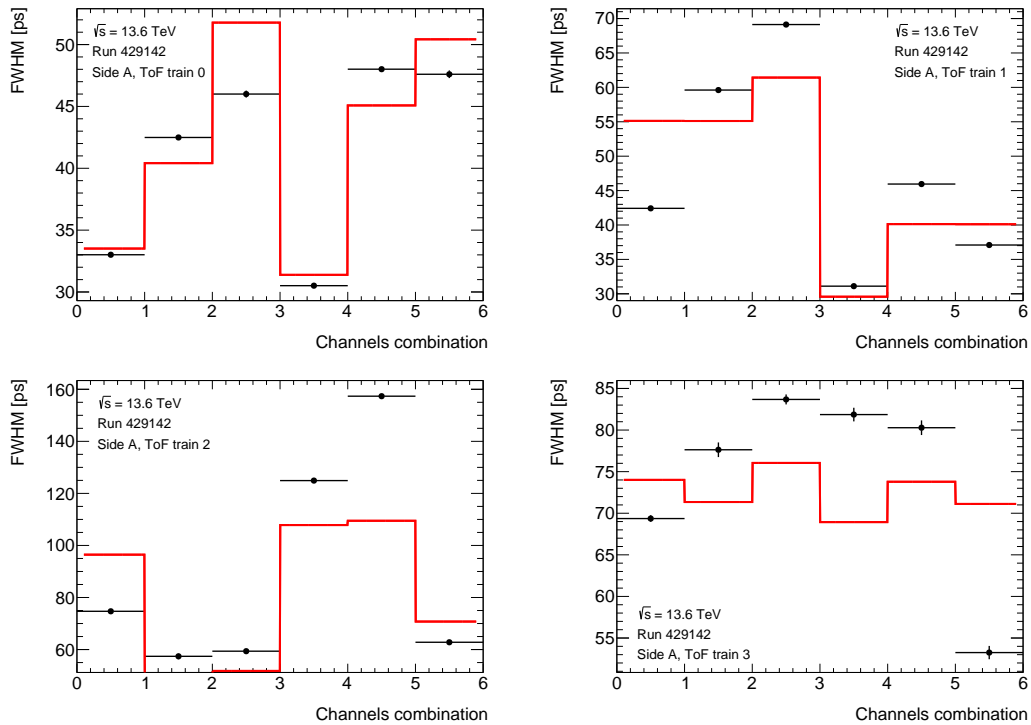


Figure 3.16: Fit for the run 429142, a double Gaussian case, for A-side.

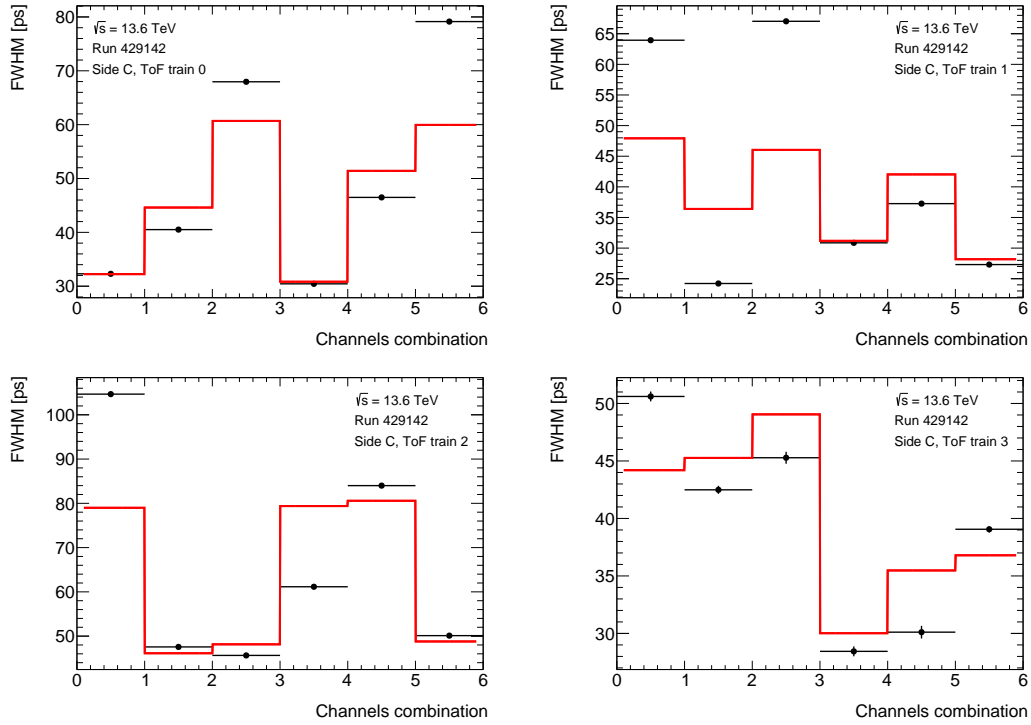


Figure 3.17: Fit for the run 429142, a double Gaussian case, for C-side.

A-side	A	B	C	D
0	29.75	15.40	27.34	42.36
1	50.99	20.93	20.89	34.23
2	-	96.45	48.21	51.78
3	53.92	50.68	46.71	53.61
C-side	A	B	C	D
0	32.24	20.19	30.82	51.41
1	36.39	31.18	-	28.18
2	32.13	72.15	33.09	35.85
3	39.37	20.07	22.32	29.25

Table 3.4: ToF time resolution (ps) for the run 429142, a double Gaussian case. Trains: 0-1, bars: A-D.

The resolutions for the case with a double Gaussian fit are more precise. Main purpose of such a fit is to obtain single-channel resolutions (4 channels) from 6 combinations of the ToF channels in one train. Fit is minimizing chi-square, as shown in Equation 3.1. The double-Gaussian case fit provides more precise and more uniform results in comparison with single-Gaussian. Therefore, only double-Gaussian will be used for the further analysis. The resulting

resolutions for the run 429142 shows that C-side gives better performance than A-side.

The same procedure was used on low- μ (low pile-up) run 435229. The Δt distributions for the run 435229 with a fitted curve overlaid to obtain the widths of the distributions are shown in Figures 3.18-3.21 for train 0 (3.18), train 1 (3.19), train 2 (3.20) and train 3 (3.21). All widths are listed in Table 3.5. The resulting time resolutions for the run 435229 are given in Table 3.6. Figures 3.22 and 3.23 show this fit for A and C sides, respectively, with channels combinations on X-axis in the same order as in Table 3.5 and widths of the Δt distributions on the Y-axis. The resulting resolutions for the low- μ run 435229 shows that C-side gives better performance than A-side, same as it was for the run 429142.

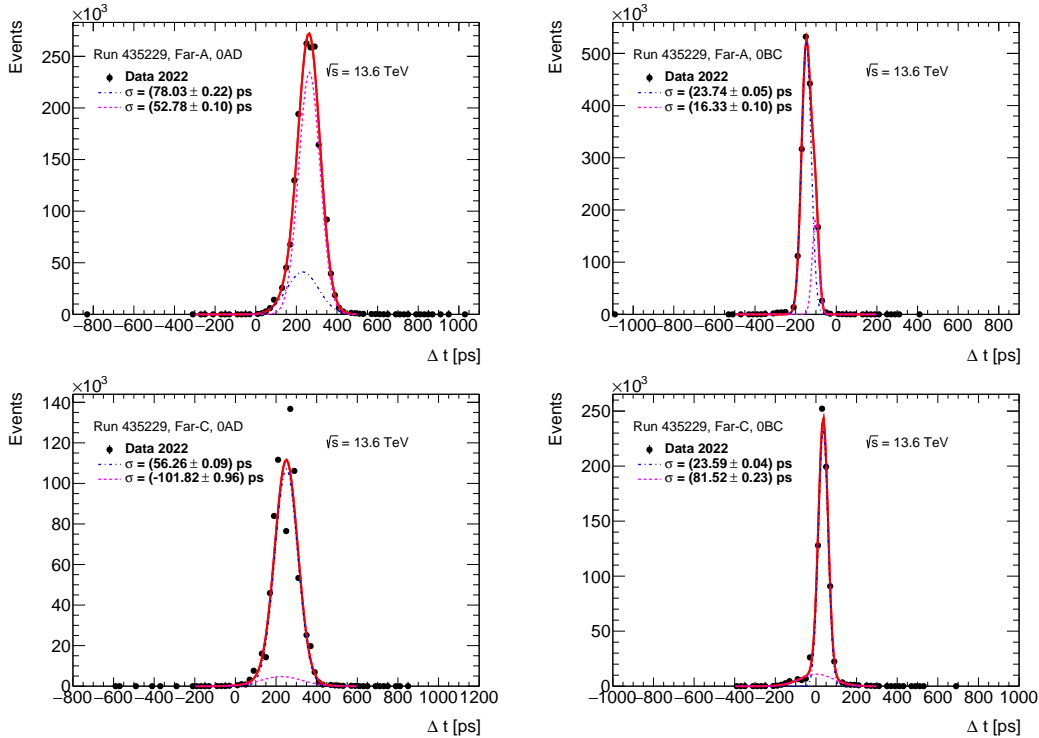


Figure 3.18: Δt distributions for the run 435229 with a double Gaussian fitted curve overlaid for 2 combinations (AD - left, BC - right) of the ToF channels in train 0 for A-side (top) and C-side (bottom).

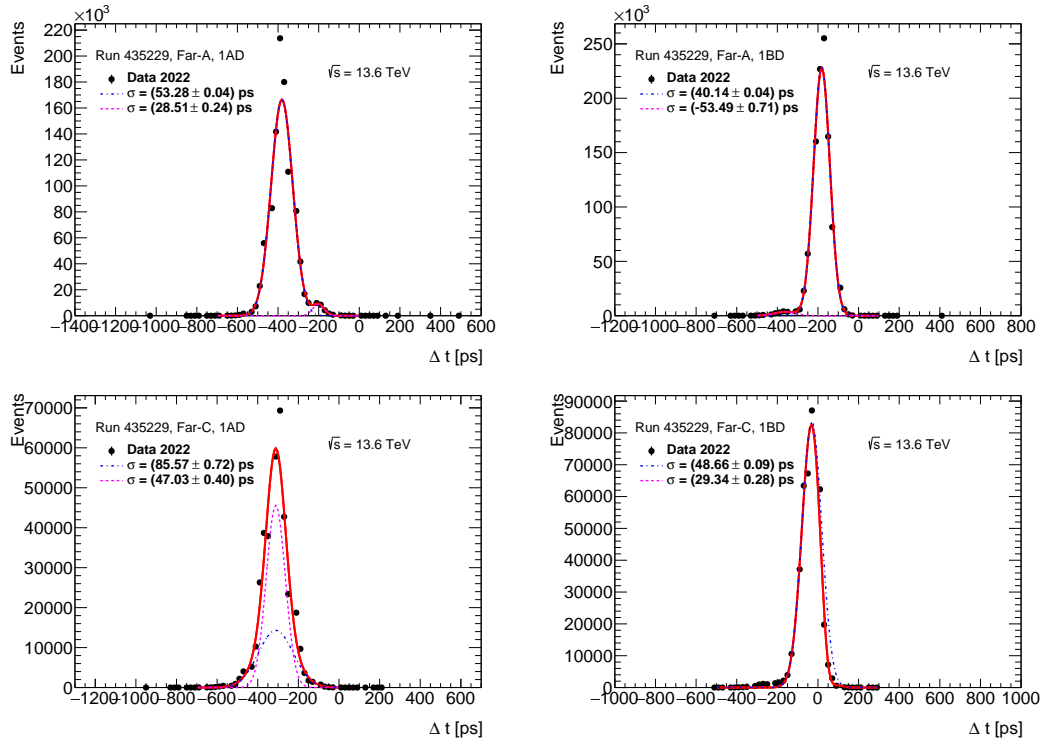


Figure 3.19: Δt distributions for the run 435229 with a double Gaussian fitted curve overlaid for 2 combinations (AD - left, BD - right) of the ToF channels in train 1 for A-side (top) and C-side (bottom).

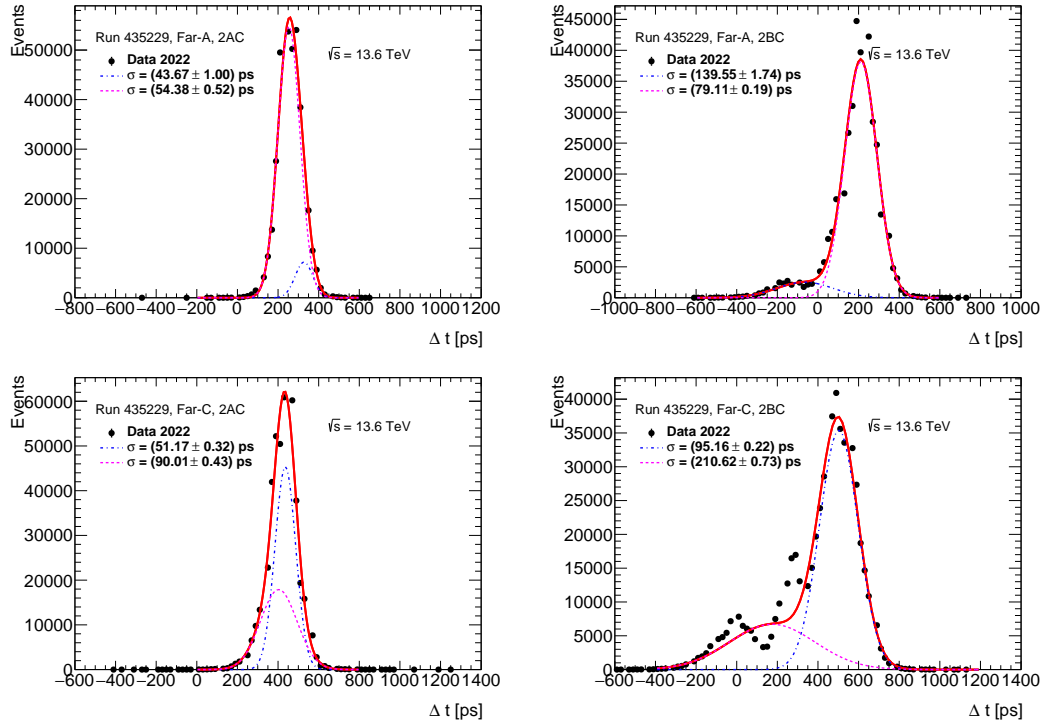


Figure 3.20: Δt distributions for the run 435229 with a double Gaussian fitted curve overlaid for 2 combinations (AC - left, BC - right) of the ToF channels in train 2 for A-side (top) and C-side (bottom). Right distributions show large data fluctuations.

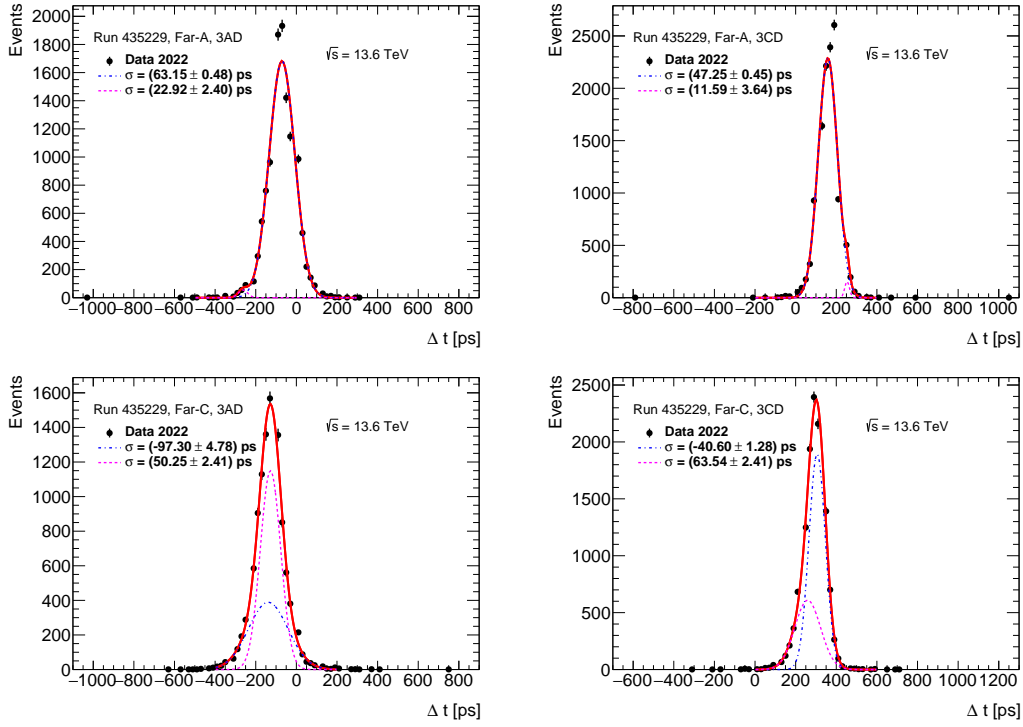


Figure 3.21: Δt distributions for the run 435229 with a double Gaussian fitted curve overlaid for 2 combinations (AD - left, CD - right) of the ToF channels in train 3 for A-side (top) and C-side (bottom).

A-side	AB	AC	AD	BC	BD	CD
0	23.95	36.31	52.78	23.74	45.90	45.53
1	39.45	44.50	53.28	25.69	40.14	22.74
2	47.18	54.38	50.64	79.11	74.80	61.90
3	40.15	58.57	63.15	34.24	55.55	47.25
C-side	AB	AC	AD	BC	BD	CD
0	32.33	42.27	56.26	23.59	45.16	46.89
1	46.38	54.63	47.03	29.64	48.66	29.70
2	101.04	51.17	47.85	95.16	86.67	57.14
3	64.77	60.94	50.25	44.73	59.87	40.60

Table 3.5: Width of Δt (ps) distributions for the run 435229 using a double Gaussian fit for all combinations of the ToF channels inside one train. Trains: 0-1, bars: A-D.

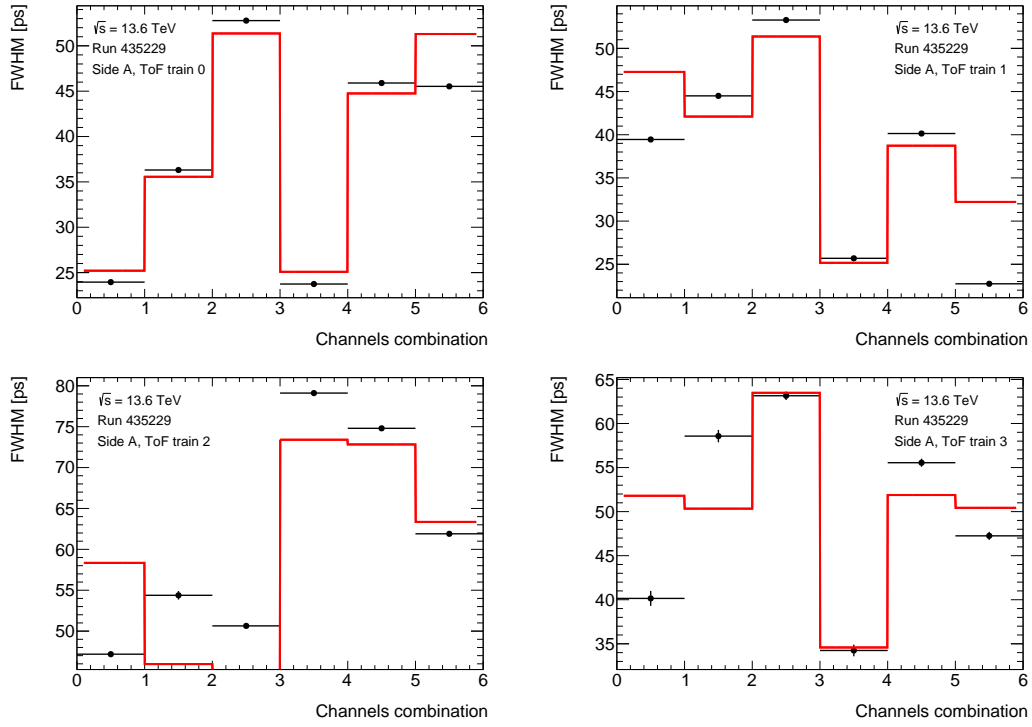


Figure 3.22: Fit for the run 435229, a double Gaussian case, for A-side.

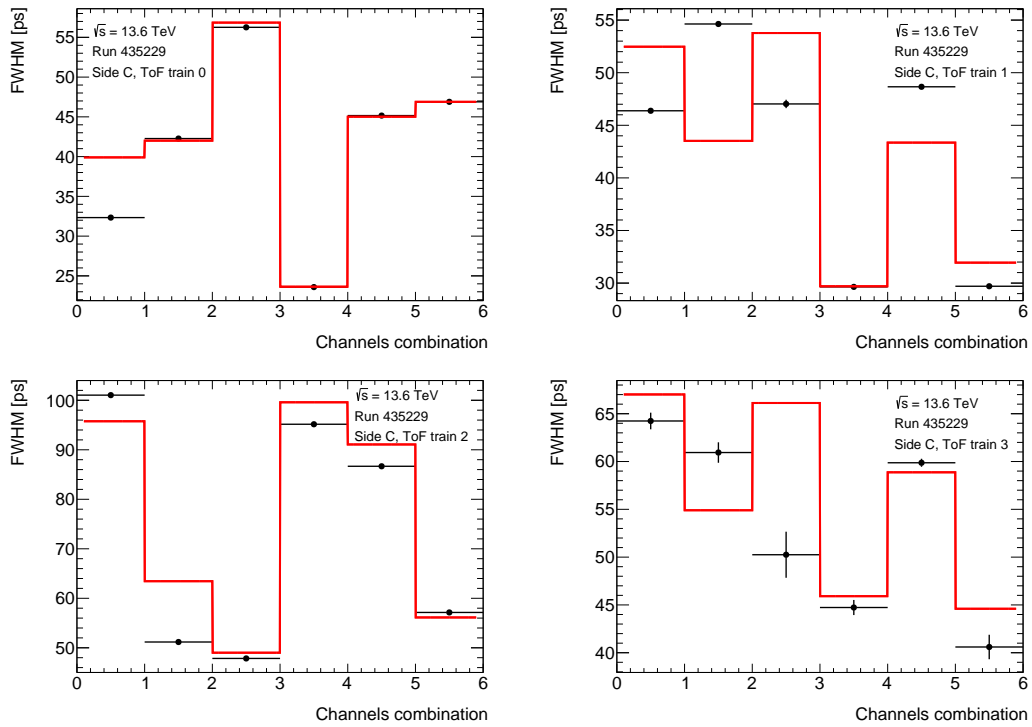


Figure 3.23: Fit for the run 435229, a double Gaussian case, for C-side.

A-side	A	B	C	D
0	25.20	-	25.08	44.75
1	41.07	23.40	9.25	30.85
2	8.04	57.78	45.26	44.32
3	44.83	25.93	22.87	44.93
C-side	A	B	C	D
0	37.40	13.90	19.11	42.81
1	43.38	29.50	3.37	31.76
2	40.47	86.78	48.86	27.62
3	51.94	42.33	17.76	40.90

Table 3.6: ToF time resolution (ps) for the run 435229, a double Gaussian case. Trains: 0-1, bars: A-D.

Resolutions resulting from this fit show very preliminary values. The present fits are not precise enough due to the freshness of the data and some missing calibrations, which are not included in this analysis. Therefore, these values are only indicative.

3.3 Efficiency

Information about the reconstructed SiT tracks are stored in the AFP-TrackContainer [22]. This container was used as a basis for the measurement of the ToF response. The efficiency in each channel is defined as a fraction based on two samples, first where the given ToF channel provided time information, and second a reference sample of events with reconstructed SiT tracks. For obtaining efficiencies two methods were used: dividing histograms and calculating the ratio of sums of events.

For both methods the following requirements were imposed on the data:

- One track in the SiT per event.
- At most one cluster per plane in the SiT per event.
- One active train in the ToF per event (ON/OFF)

The last requirement was imposed as a cleanup cut to remove unwanted events. However, this requirement decreases the statistics as not all tracks are in one train only. Thus, both cases (ON/OFF) were investigated. For both methods the whole procedure is performed separately for side A and side C. The regions for the x-value of the SiT, corresponding to the ToF train, were defined for each side (A and C). These regions are shown in Table 3.7.

Train	A-side (mm)	C-side (mm)
0	-4.9 to -2.0	-5.3 to -2.0
1	-8.0 to -5.0	-8.4 to -5.4
2	-13.0 to -8.1	-13.4 to -8.5
3	-15.0 to -13.1	-15.0 to -13.5

Table 3.7: Regions for the x-value of the SiT, corresponding to the ToF trains.

For the first method, dividing histograms, the reference histogram is defined for events passing the selection criteria without the optional requirement (OFF), only for events with reconstructed SiT tracks. The other 16 histograms include (or no, depends on a case which is under investigation) the additional requirement (ON) for each of the 16 ToF channels.

The next step was dividing each of 16 channel histograms by the reference histogram bin by bin. So, the number of events in each individual bin of one of the 16 histograms of the ToF is divided by the number of events in the corresponding bin of the reference histogram. This ratio defines the efficiency in each bin which is shown in Figure 3.24. The case with the requirement (ON) is shown for the 4 trains, side-A, bar B. In order to define efficiency in each channel the mean value of the bins in the region, corresponding to the exact train, was calculated. For the last train (3) the active region was cut in order to avoid noise, possibly originating from the collimator shadow².

The procedure described above is for the case with the requirement (ON). Next, the procedure is repeated without the requirement (OFF) and results are given in Figure 3.25 for the ToF trains of side-A and bar B. Some background is visible for the case without the requirement (OFF), and the reason needs to be further studied.

²as discussed at an ATLAS Combined Performance meeting

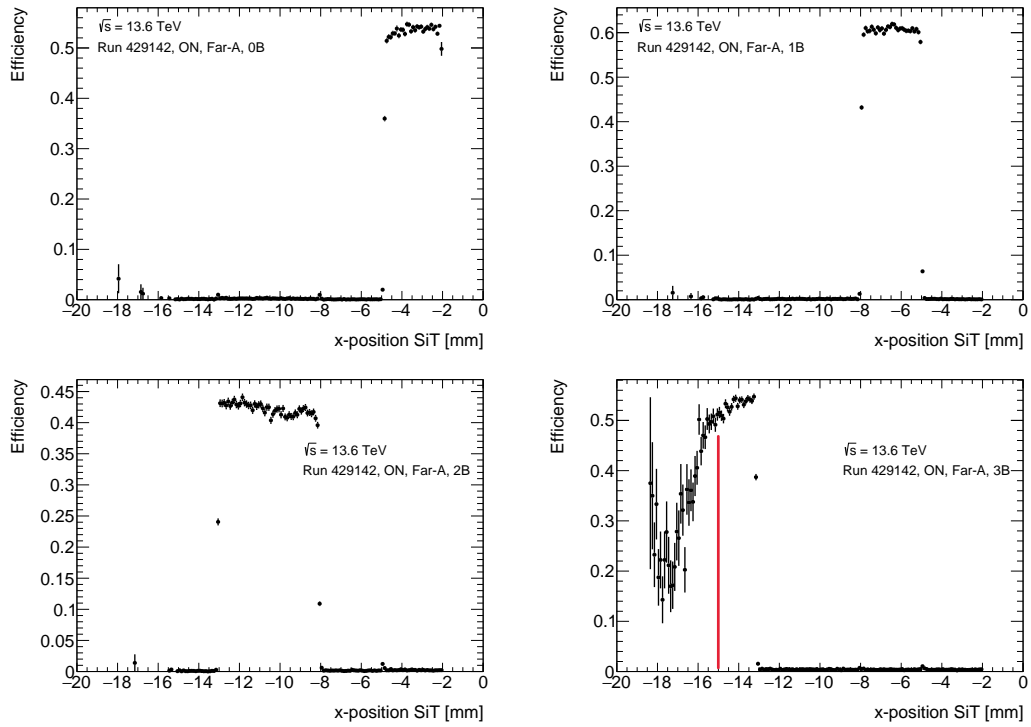


Figure 3.24: Ratios, which define efficiencies for the run 429142, for the case of cuts "one train ON" for A-side for each train and one bar: 0B (top left), 1B (top right), 2B (bottom left) and 3B (bottom right).

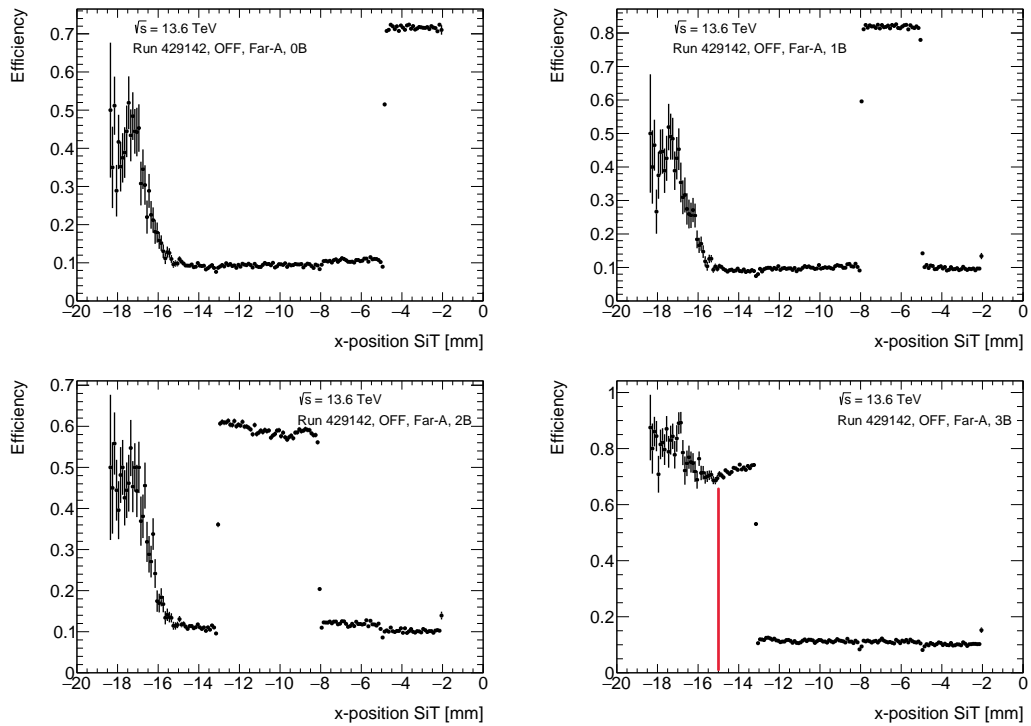


Figure 3.25: Ratios, which defines efficiencies for the run 429142, for the case of cuts "one train OFF" for A-side for each train and one bar: 0B (top left), 1B (top right), 2B (bottom left) and 3B (bottom right).

The resulting efficiencies for both cases (ON/OFF) for the histogram ratio method are shown in Figure 3.26, top: ON, bottom: OFF. Each cell on that plot corresponds to the efficiency in this channel assuming that SiT track points on respective ToF train.

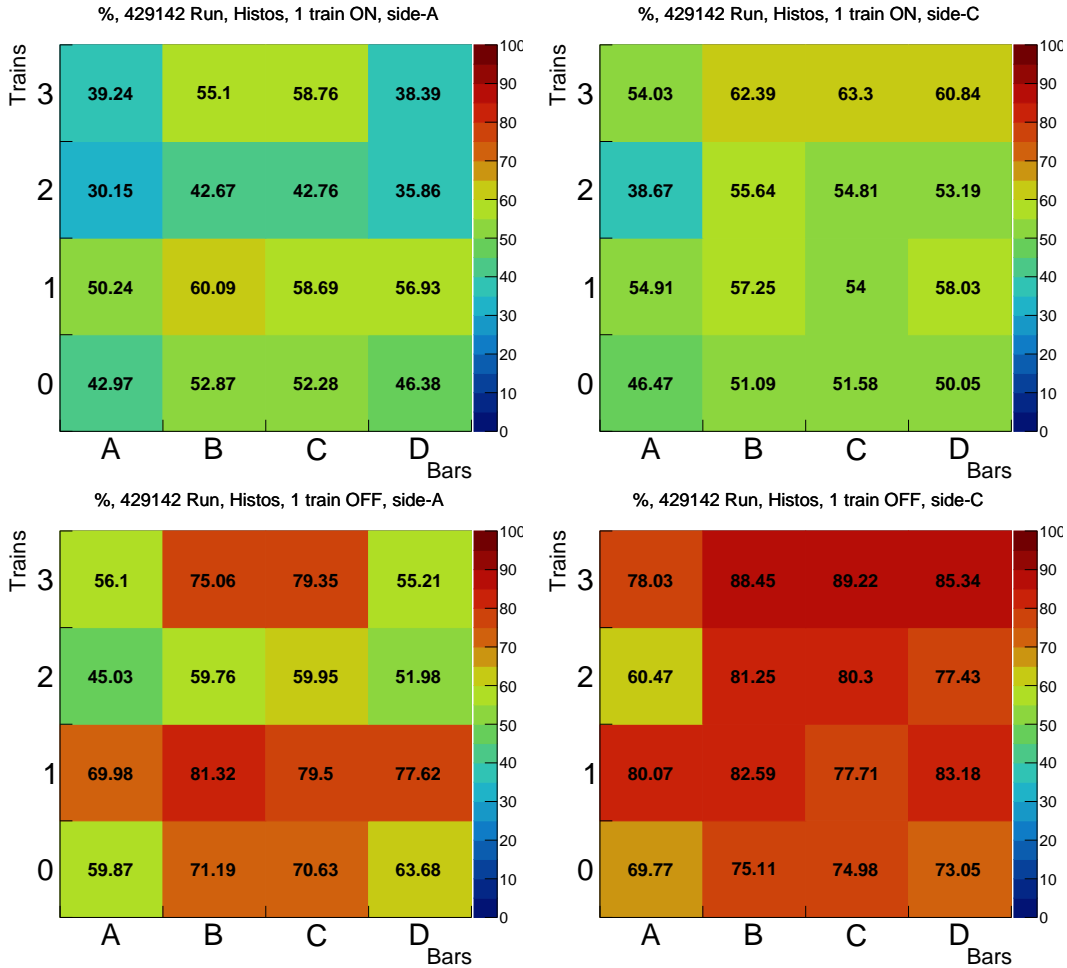


Figure 3.26: Efficiencies (%) for the run 429142 for each channel of ToF for A (left) and C (right) sides with the optional requirement ON, (top) and OFF, (bottom) for the "histogram" method.

For the second method, direct numbers, i.e. the number of events in the two samples were counted. For the first sample an event has to pass the main requirements (OFF) and in addition the track has to be inside a given region in x , as measured by the silicon detector (Table 3.7). For the second sample, the event has to pass the requirement ON (or no, depends on a case which is under investigation) and there must be a hit in a corresponding channel of the ToF. There are 16 values for the second sample (for each channel), and 4 numbers for the first sample (for each train). The efficiency is defined as the ratio of the number of events in the second sample divided by the number of events in the first sample. The resulting efficiencies for both cases (ON/OFF)

for this method are shown in Figure 3.27, top: ON, bottom: OFF. Each cell on that plot corresponds to the efficiency in this channel assuming that SiT track points on respective ToF train.

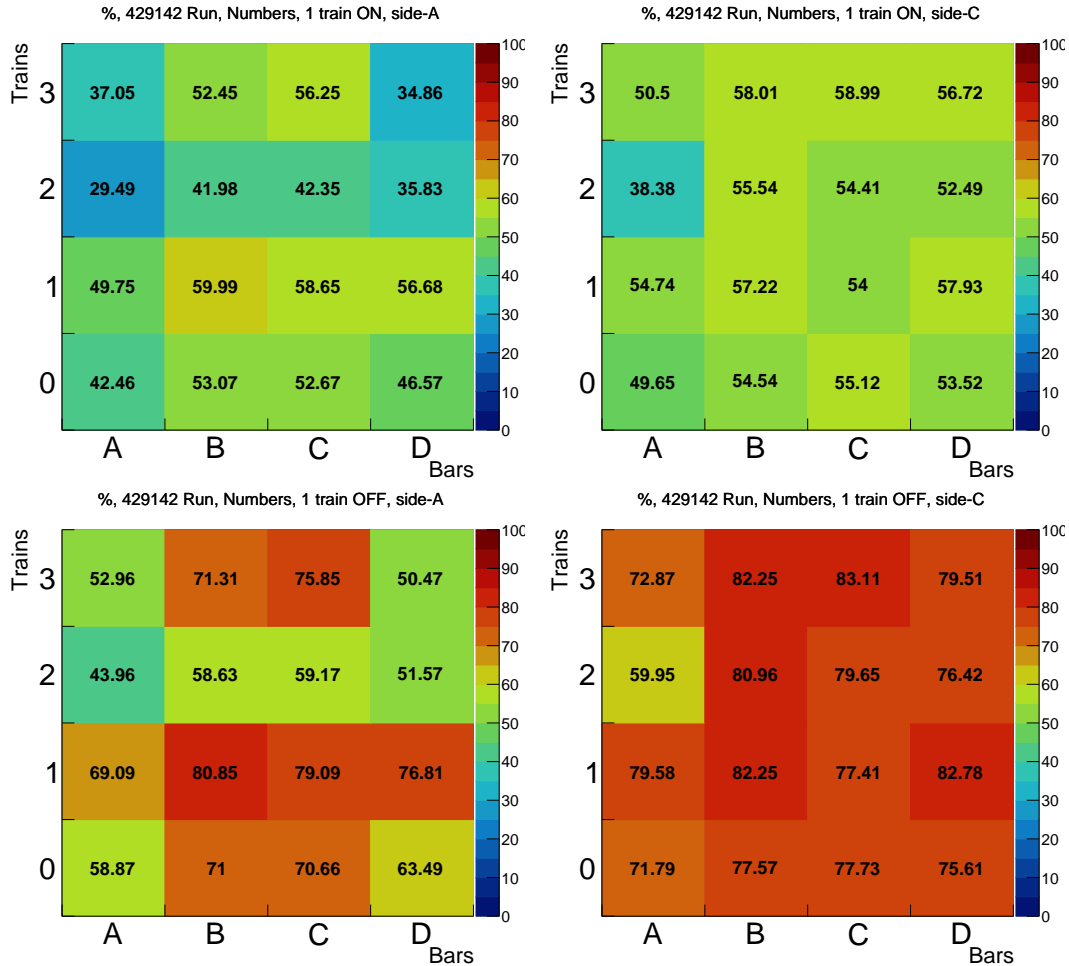


Figure 3.27: Efficiencies (%) for the run 429142 for each channel of ToF for A (left) and C (right) sides with the optional requirement ON, (top) and OFF, (bottom) for the "direct numbers" method.

The efficiencies for both methods are very similar. The efficiencies for case OFF is higher than for case ON, as far as it includes non ideal events and some background. A comparison of the methods shows almost the same results, therefore, for the further studies only "direct numbers" method will be used.

The same procedure for the "direct numbers" method was applied to the low- μ run 435229. The resulting efficiencies for both cases (ON/OFF) for the method of "direct numbers" are shown in Figure 3.28, top: ON, bottom: OFF. Each cell on that plot corresponds to the efficiency in this channel assuming that SiT track points to the respective ToF train.

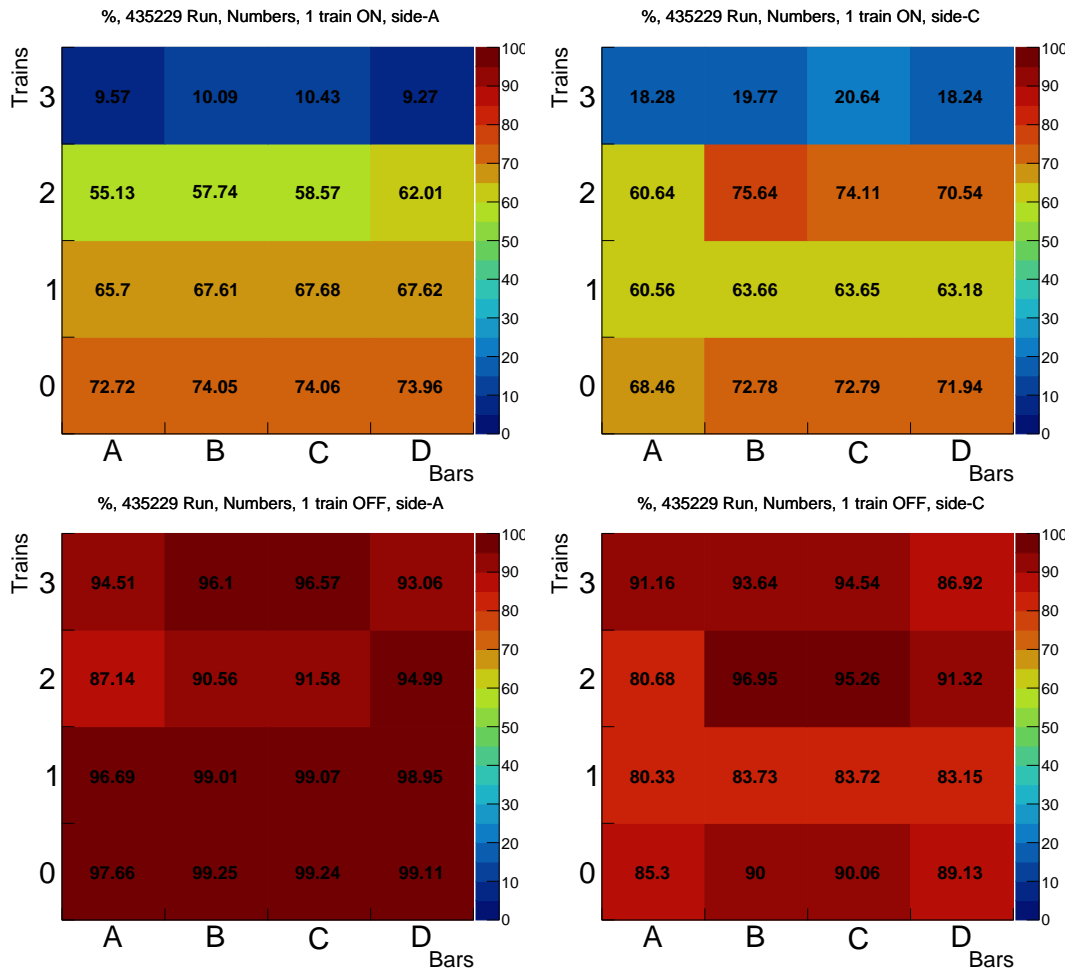


Figure 3.28: Efficiencies (%) for the run 435229 for each channel of ToF for A (left) and C (right) sides with the optional requirement ON, (top) and OFF, (bottom) for the "direct numbers" method.

The low- μ run 435229 case ON shows structure close to the step-like with higher efficiencies in train 0 and lower in train 3. The possible reason of such a structure is proximity to the beam. Since this run has very low pile-up, the beam is more focused than for usual high- μ run³.

Another useful method of representing efficiencies is calculate efficiency in all channels assuming that SiT track points to one of the ToF trains. With such a representation a full map of ToF activity can be seen. Both for the train to which the track points, and for other trains. Therefore, more information about possible systematic background can be obtained.

Efficiencies calculated in such a way for the run 429142 for both cases (ON/OFF) using the method "direct numbers" are shown in Figures 3.29-3.32 for train 0 (3.29), train 1 (3.30), train 2 (3.31) and train 3 (3.32).

³as discussed at an ATLAS Combined Performance meeting

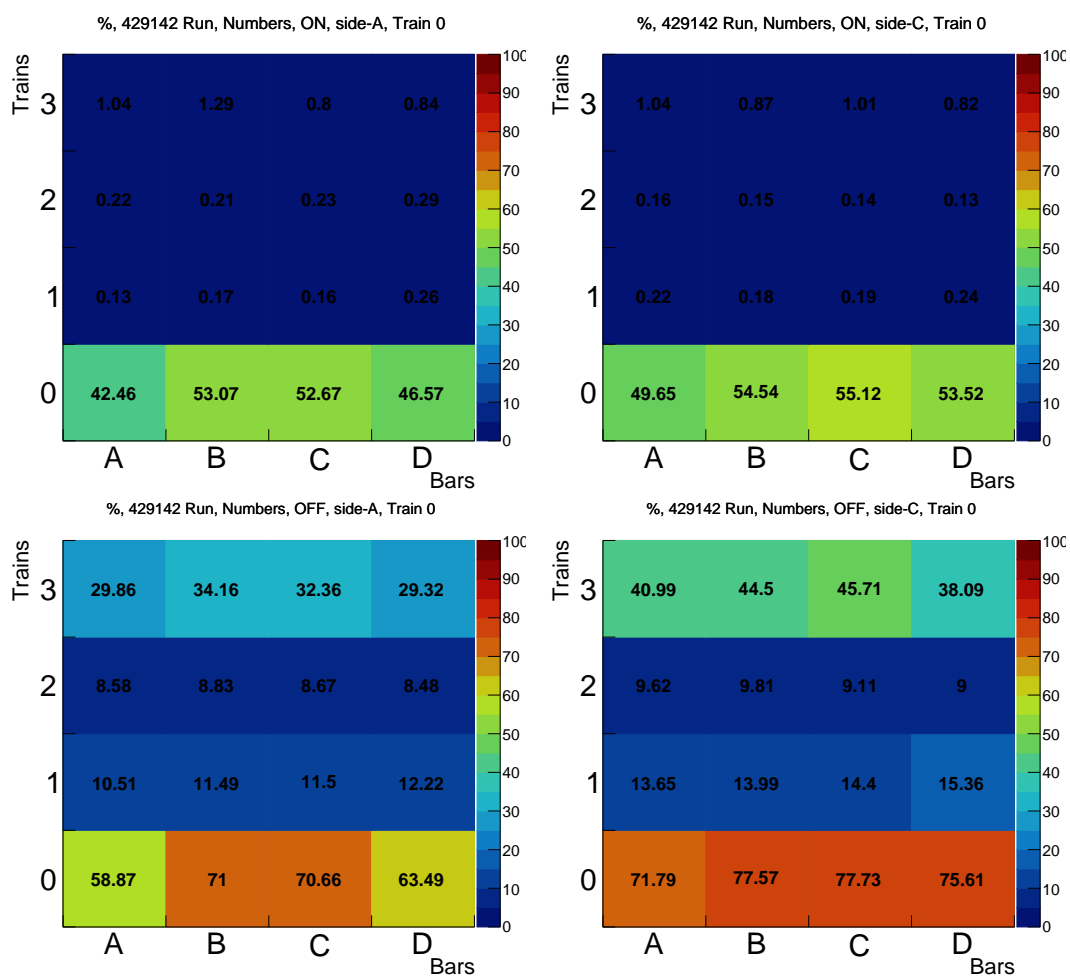


Figure 3.29: Efficiencies (%) for the run 429142 for each channel of the ToF with track pointing to train 0 for A (left) and C (right) sides with the optional requirement ON, (top) and OFF, (bottom) for the "direct numbers" method.

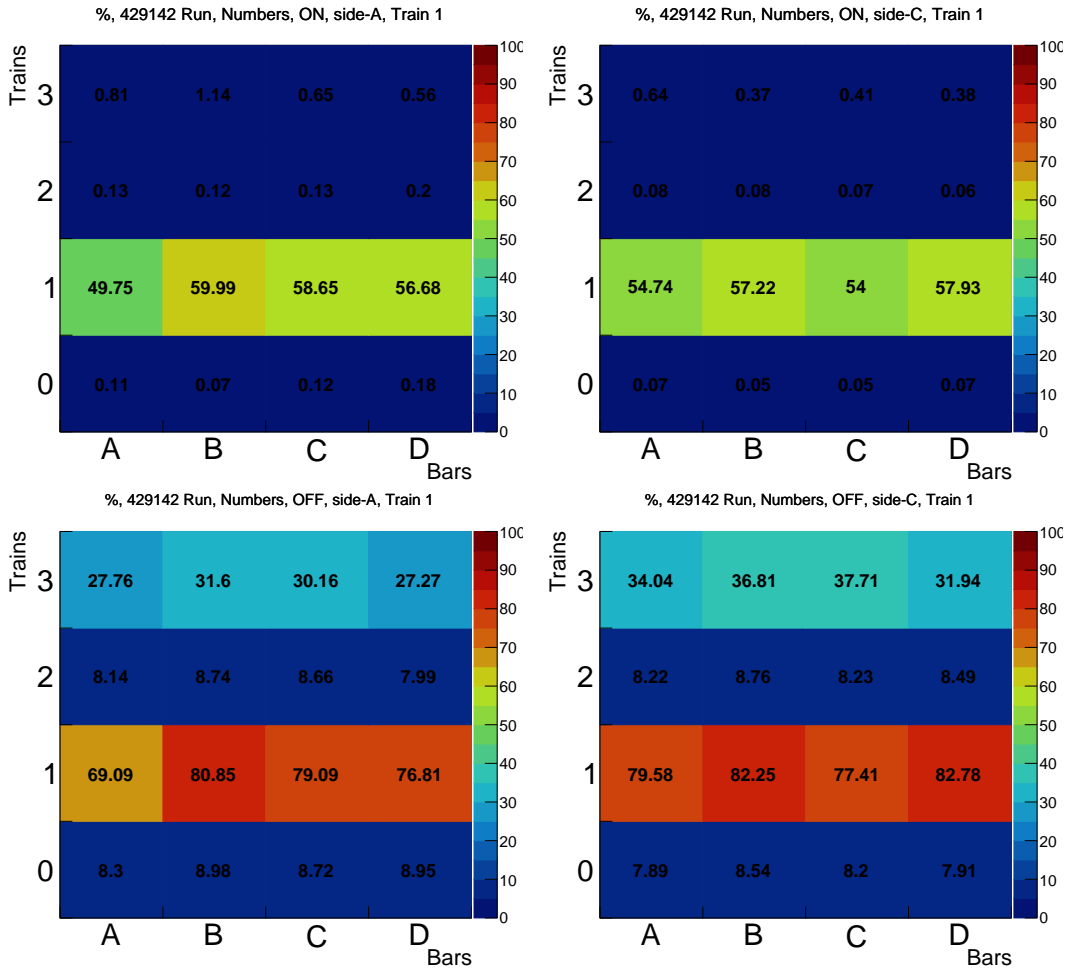


Figure 3.30: Efficiencies (%) for the run 429142 for each channel of the ToF with track pointing to train 1 for A (left) and C (right) sides with the optional requirement ON, (top) and OFF, (bottom) for the "direct numbers" method.

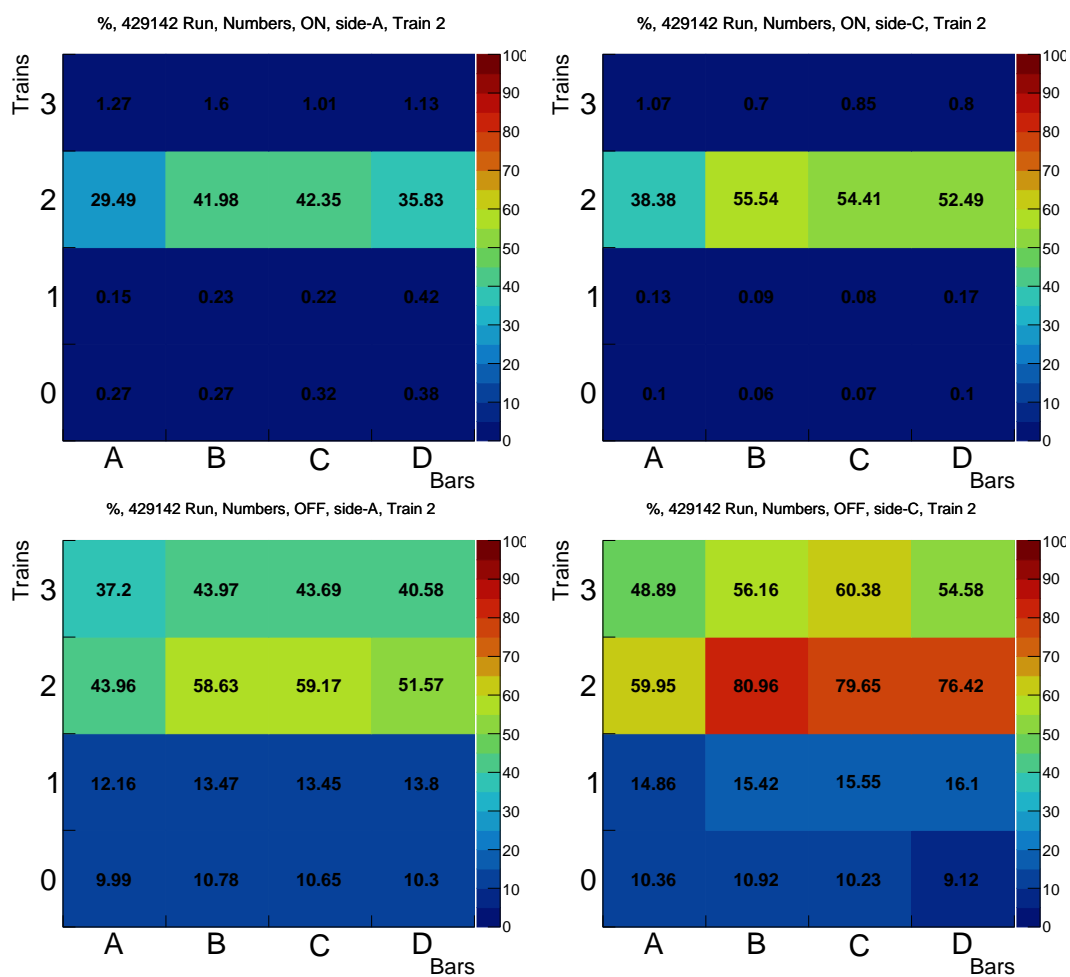


Figure 3.31: Efficiencies (%) for the run 429142 for each channel of the ToF with track pointing to train 2 for A (left) and C (right) sides with the optional requirement ON, (top) and OFF, (bottom) for the "direct numbers" method.

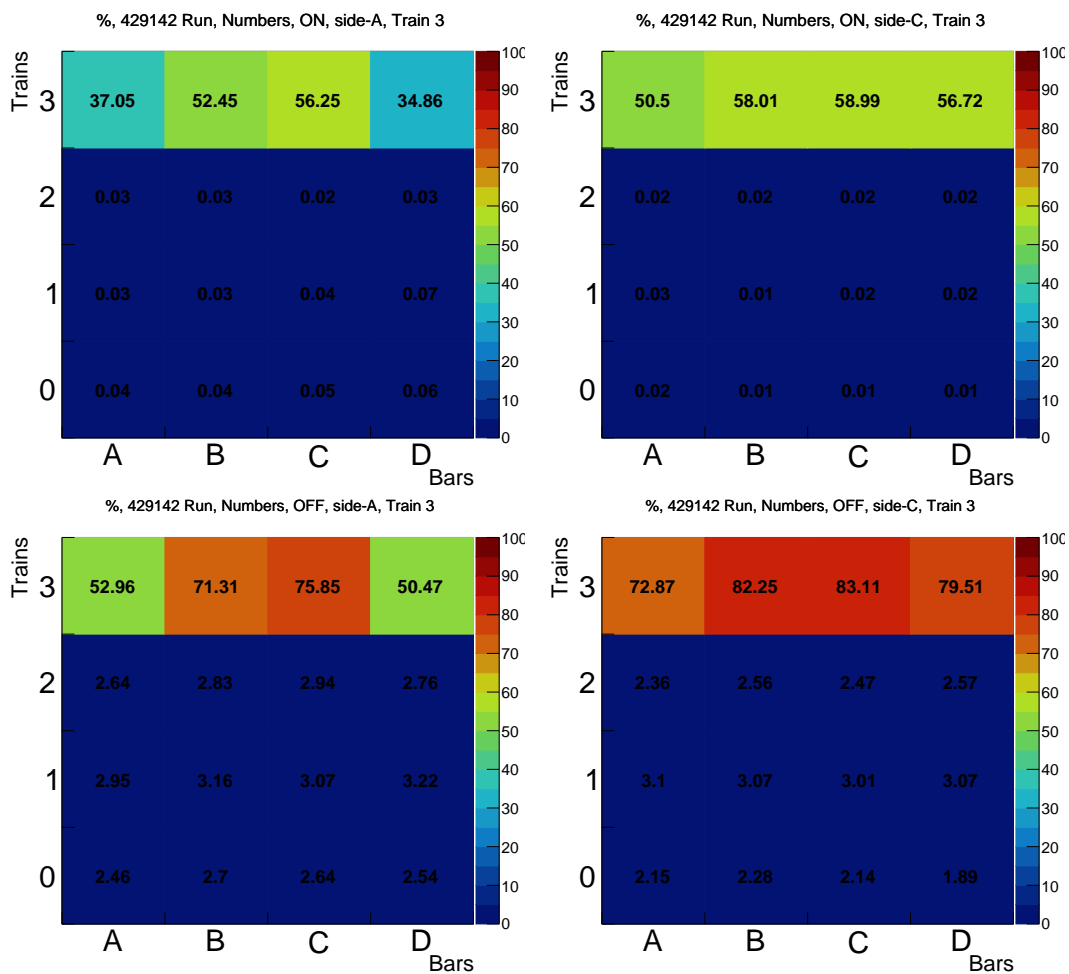


Figure 3.32: Efficiencies (%) for the run 429142 for each channel of the ToF with track pointing to train 3 for A (left) and C (right) sides with the optional requirement ON, (top) and OFF, (bottom) for the "direct numbers" method.

Efficiencies calculated in such a way for the low- μ run 435229 for both cases (ON/OFF) using the method "direct numbers" are shown in Figures 3.33-3.36 for train 0 (3.33), train 1 (3.34), train 2 (3.35) and train 3 (3.36).

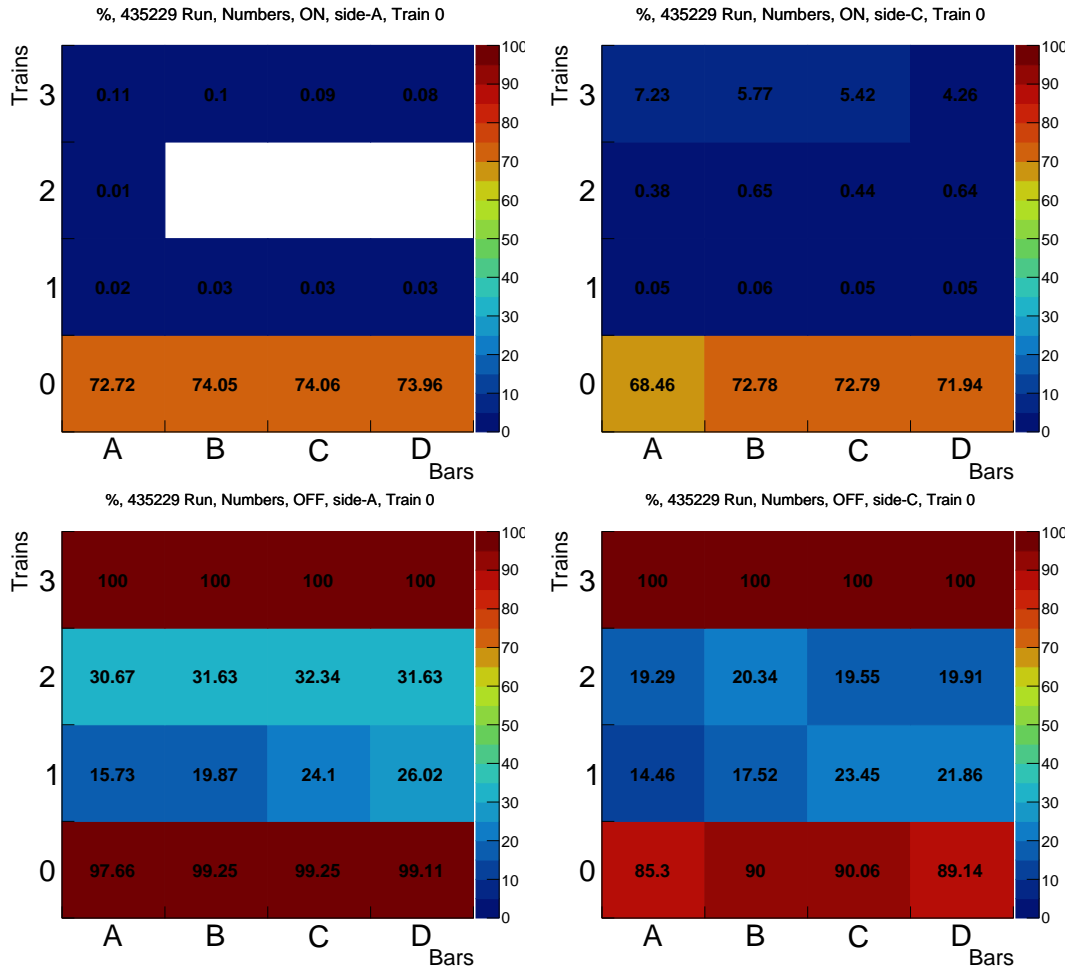


Figure 3.33: Efficiencies (%) for the low- μ run 435229 for each channel of the ToF with track pointing to train 0 for A (left) and C (right) sides with the optional requirement ON, (top) and OFF, (bottom) for the "direct numbers" method.

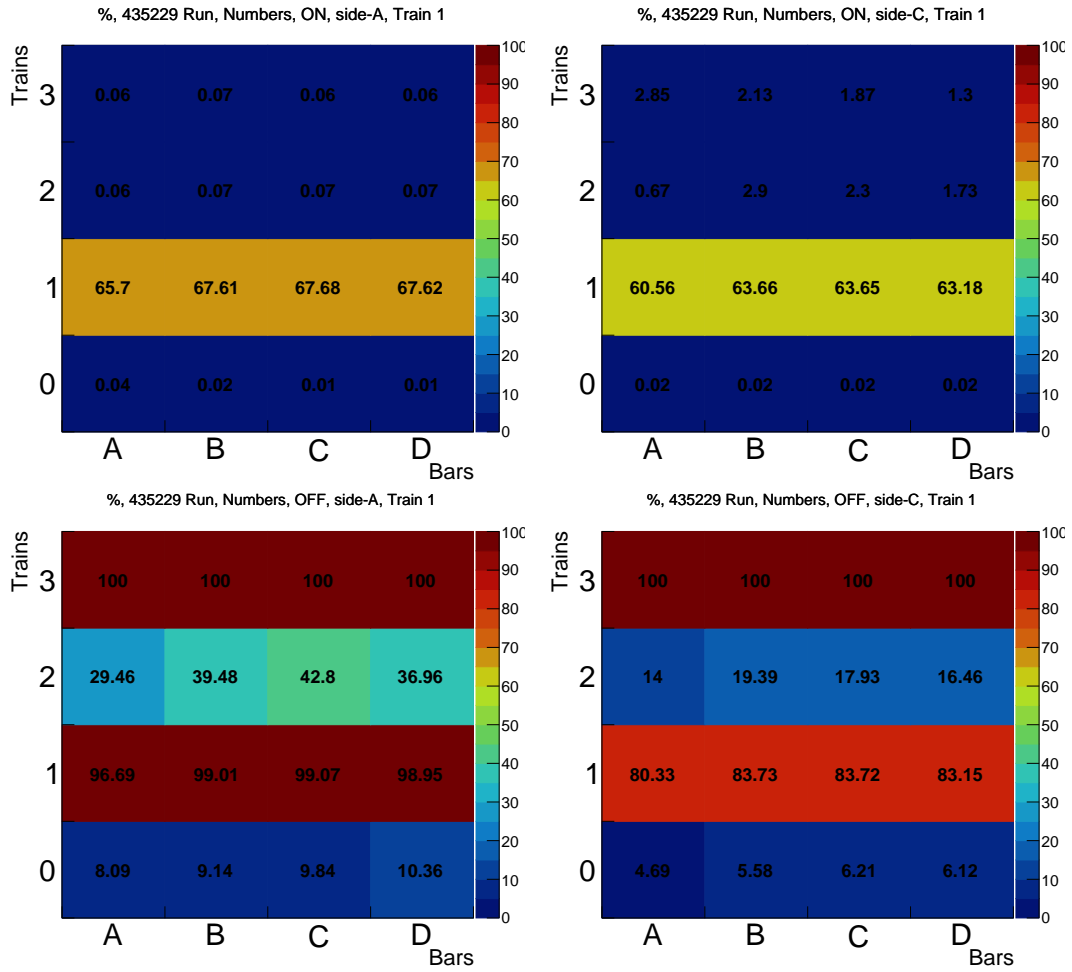


Figure 3.34: Efficiencies (%) for the low- μ run 435229 for each channel of the ToF with track pointing to train 1 for A (left) and C (right) sides with the optional requirement ON, (top) and OFF, (bottom) for "direct numbers" method.

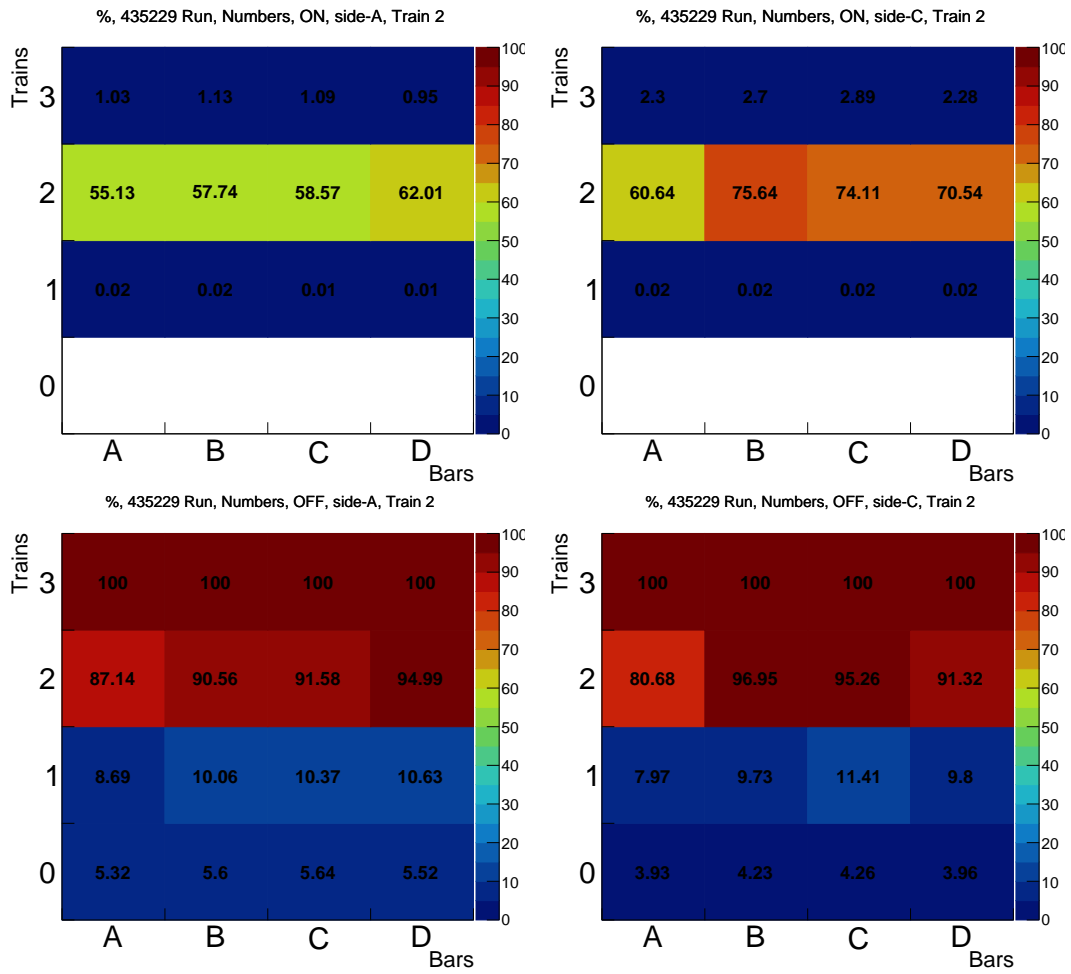


Figure 3.35: Efficiencies (%) for the low- μ run 435229 for each channel of the ToF with track pointing to train 2 for A (left) and C (right) sides with the optional requirement ON, (top) and OFF, (bottom) for the "direct numbers" method.

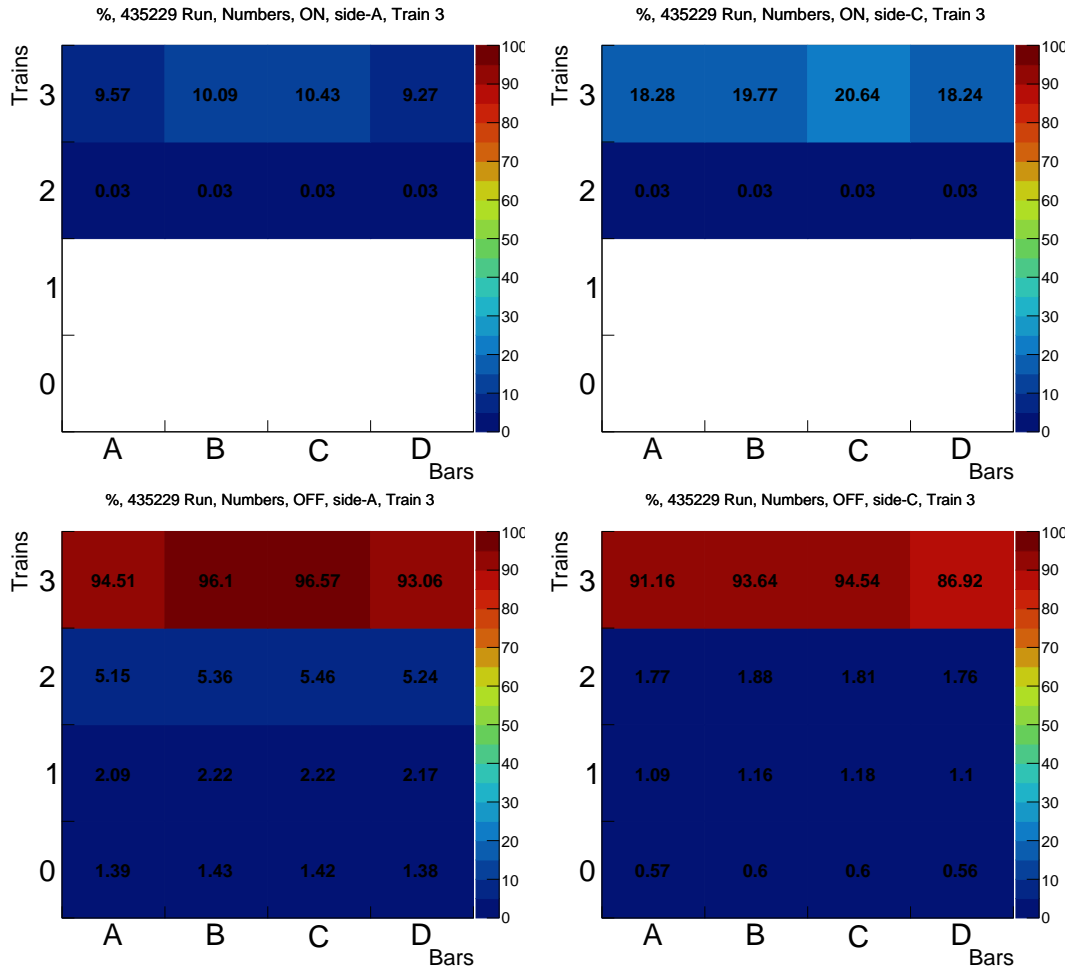


Figure 3.36: Efficiencies (%) for the low- μ run 435229 for each channel of the ToF with track pointing to train 3 for A (left) and C (right) sides with the optional requirement ON, (top) and OFF, (bottom) for the "direct numbers" method.

Typically the efficiency is maximized in the ToF train to which SiT track is pointing. For the case one train ON a clear structure can be seen. Only the pointed train is active, all other trains do not contribute in both runs. For the case one active train OFF efficiencies in pointed train are maximized, however other trains are still active, especially train 3. This effect is magnified in the low- μ run 435229. The reason for such a behavior can be the presence of secondary particles, or collimator shadow, which covers part of the train 3 and it could give secondary particles⁴.

⁴as discussed at an ATLAS Combined Performance meeting

Chapter 4

Di-photon vertex reconstruction

Two approaches were used for determining the vertex of interaction, i.e. photon pointing and calorimeter pointing methods. For the photon pointing method, the position of the event in ATLAS is selected from Primary Vertex (PV) candidates reconstructed using tracks. This method has a good resolution, but for the vertices of photons it can give misleading information (as photons do not leave tracks). The second method uses the calorimeter pointing tool [23] to obtain the vertex of the two photons.

The first part of this study was conducted prior to the collection of the first data from LHC Run-3. Therefore, Run-2 data taken in 2017 with integrated luminosity of 14.3 fb^{-1} were used for this analysis. For a rejection factor calculation, a simple simulation of the ToF data was used.

The two vertex reconstruction techniques were compared, and the most appropriate one was used on the first Run-3 data from 2022 year in the second part of this chapter.

4.1 Data 2017

4.1.1 Photon pointing

For this analysis, the earlier prepared n-tuples for the ALP with AFP search were used for the photon pointing method. They were created on the basis of the simulated AODs [20] corresponding to ALP masses from 100 to 2000 GeV with the coupling constant $g = 0.2$. These n-tuples contain true primary vertex and the reconstructed vertex. The difference between them defines the resolution of the method. The photon pointing method selects one Primary Vertex from the PV candidates reconstructed using tracks. There can be two types of photons, namely converted and unconverted photons. The resolutions are determined for two cases, two unconverted and two converted photons. Conversion means production of an electron and positron pair. This is caused by the electromagnetic interaction with the material in the detectors. Electrons and positrons have electric charge, therefore they interact with the

tracker and leave their tracks. The conversion occurs at about 30% probability. Unless conversion occurs, there is no track pointing to the PV, and we cannot obtain precise information about the PV position.

Figure 4.1 shows the resolutions for the different masses of the ALP for the photon pointing method in simulated signal events. The widths of these distributions are shown in Figure 4.2 as a function of mass.

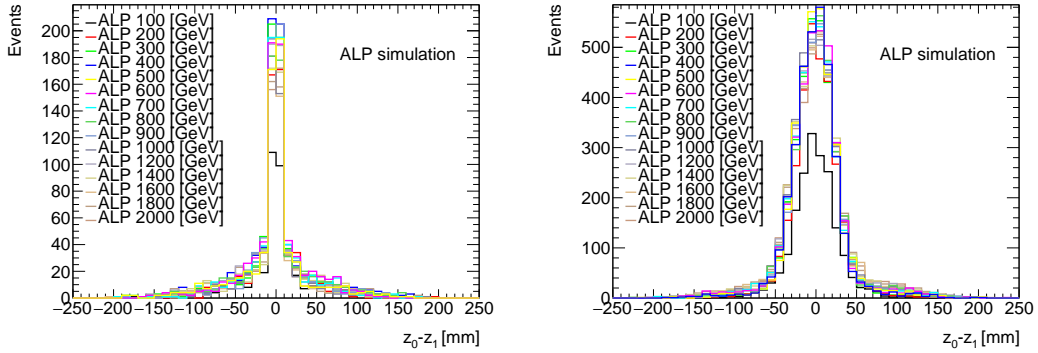


Figure 4.1: Resolutions using the photon pointing method for converted (left) and unconverted (right) photons for different ALP masses in simulated signal events.

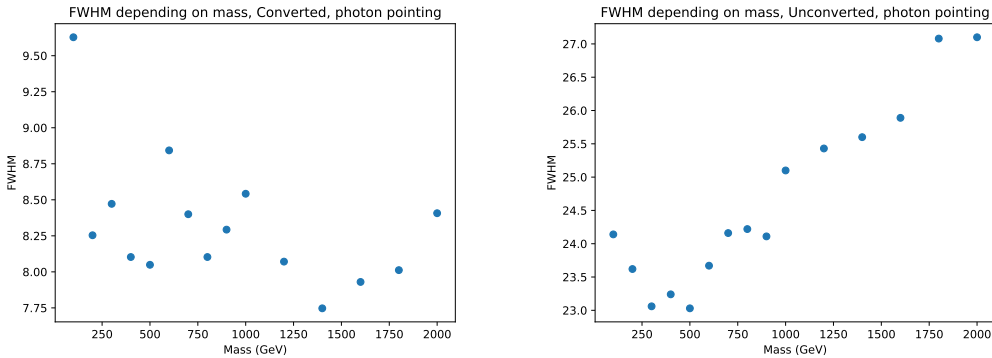


Figure 4.2: Widths (FWHM - Full Width Half Maximum) of resolutions in mm using photon pointing method for converted (left) and unconverted (right) photons as a function of ALP mass in simulated signal events.

For the unconverted photons a slight slope with increasing ALP mass is observed. In contrast, there is no dependence on the ALP mass for converted photons.

4.1.2 Calorimeter pointing

Resolutions

In the previous section it was noticed that the photon pointing method can give misleading information, since unconverted photons do not leave any tracks.

For this reason another pointing method was used, the calorimeter pointing method. This method uses "traces" which photons leave in the calorimeter to reconstruct the displaced di-photon vertex.

For this method the "Calo Pointing tool" from "Delayed Hino Analysis" was used [23]. Starting from the Derived Analysis Object Data (DAOD) DAOD_HIGG1D1 n-tuples created from the simulated events for the ALP masses in the range 100-2000 GeV with a coupling constant $g = 0.2$.

Figure 4.3 shows the resolutions for the different masses of the ALP using the calorimeter pointing method in the simulated signal events with a cut on the transverse momentum $p_t > 40$ GeV. The widths of these distributions are shown in Figure 4.4 as a function of the ALP mass. There is no dependence on the ALP mass. The resolutions were obtained as differences between the truth vertices and the reconstructed vertices using the calorimeter pointing method.

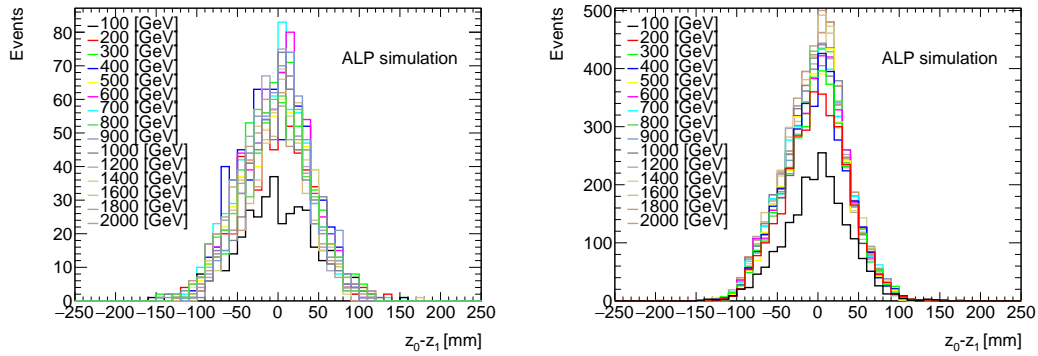


Figure 4.3: Resolutions using calorimeter pointing method for converted (left) and unconverted (right) photons for different masses of ALP in simulated signal events.

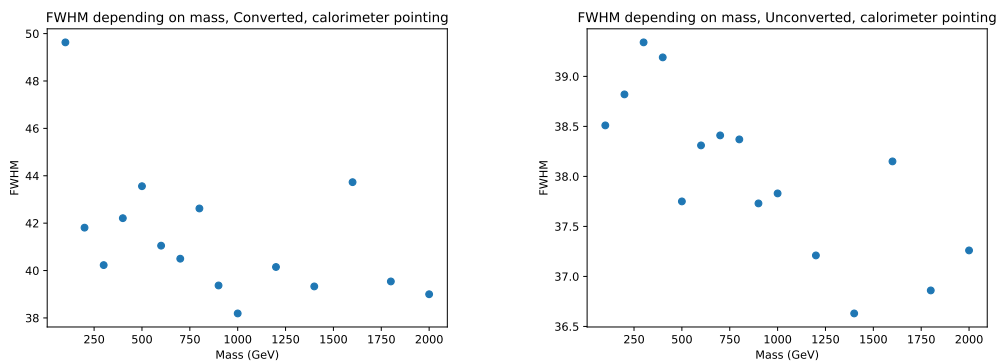


Figure 4.4: Widths (FWHM - Full Width Half Maximum) of resolutions in mm using calorimeter pointing method for converted (left) and unconverted (right) photons as a function of ALP mass in simulated signal events.

Using the calorimeter pointing tool on the data, collected in 2017, n-tuples for 20 different data sets were created. Figure 4.5 shows the distributions for the

resolutions in data for different runs as a function of a the run number. There is no dependence on the run number, according to Figure 4.6, which shows width of these resolutions as a function of a the run number. Resolutions were obtained as a difference between vertices of two photons in the data 2017.

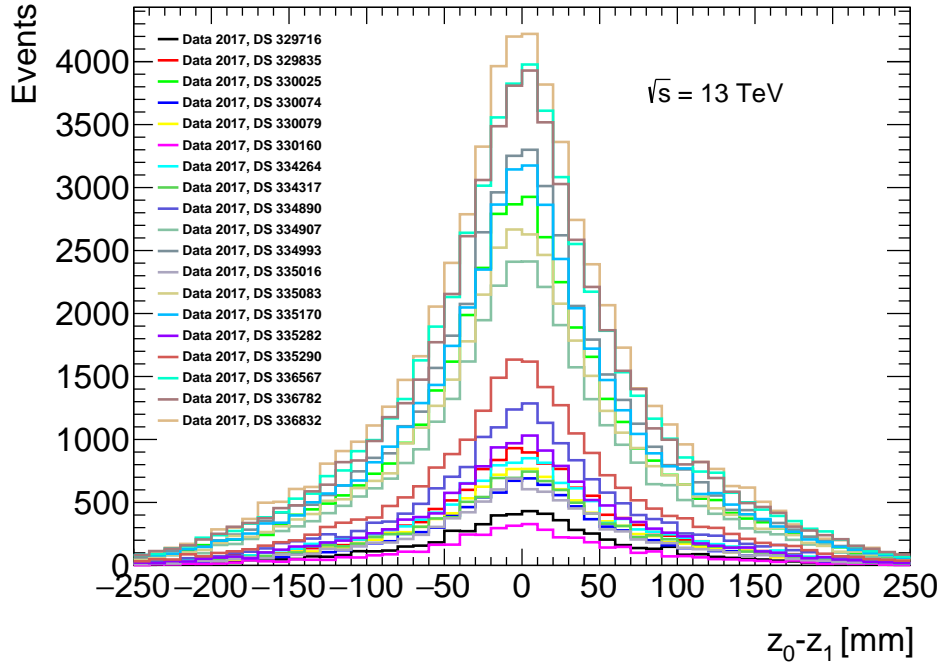


Figure 4.5: Resolutions using the calorimeter pointing method for different 2017 data sets (DS). The values, z_0 and z_1 , correspond to the z -position of the leading and the sub-leading photons, respectively.

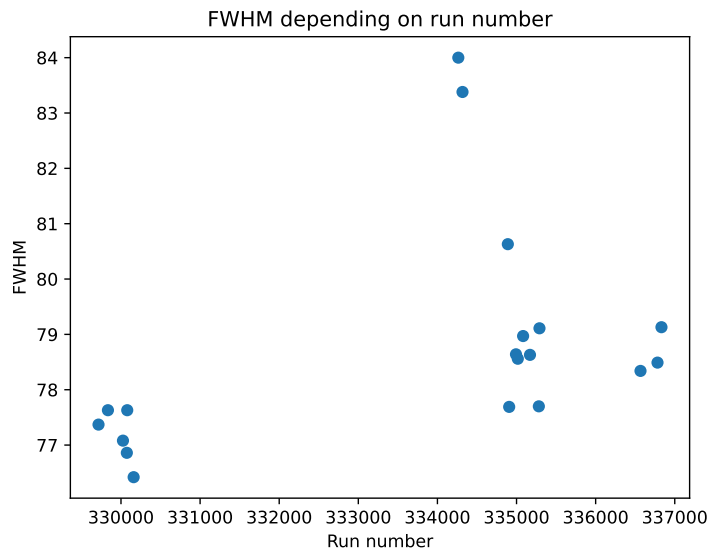


Figure 4.6: Widths (FWHM - Full Width Half Maximum) of the resolutions in mm using the calorimeter pointing method for different 2017 data sets.

Table 4.1 summarizes the comparison of the photon pointing and the calorimeter pointing methods as widths of the distributions for the simulated samples. For the case of converted photons, the photon pointing method has a narrow peak and wider peak around zero. In the table the value of the narrow peak is listed.

Mass (GeV)	Photon pointing		calorimeter pointing	
	Converted	Unconverted	Converted	Unconverted
200	8.25	23.62	41.81	38.82
400	8.10	23.24	42.21	39.19
800	8.10	24.22	42.62	38.37
1600	7.93	25.89	43.73	38.15

Table 4.1: Width (mm) of resolutions using photon and calorimeter pointing methods for different ALP masses.

Figure 4.7 compares the resolutions in simulated events and recorded data. For the simulated sample the ALP mass is 400 GeV. Distributions of simulated events and recorded data are plotted normalized to the same number of events.

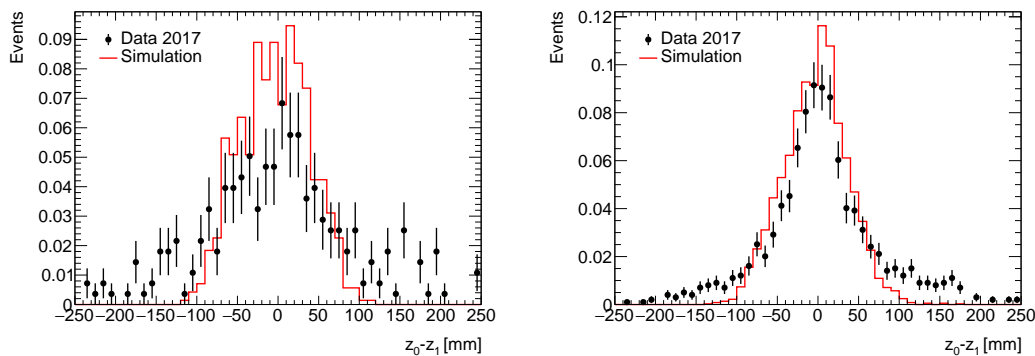


Figure 4.7: Compared resolutions for converted (left) and unconverted (right) photons for simulated events and recorded data using the calorimeter pointing method.

The width for the case of the converted (unconverted) photons of the simulated events and the recorded data distributions are 42.21 mm (39.19 mm) and 71.51 mm (57.51 mm), respectively. The reason for the large value in the recorded data could be that the di-photons in the data do not result from the simulated ALP process.

Comparison of the two techniques of vertex reconstruction shows better resolution for photon pointing method. Nevertheless, this method has limited opportunities in case of photons, as they do not leave tracks in trackers.

Background rejection

In order to study how the information from the Time-of-Flight (ToF) detector can help to reduce background to a possible di-photon signal, a simple event simulation of the vertex position was created. This simulation is based on design information about the time resolutions of the ToF detector, namely 20 ps (≈ 6 mm) and 26 ps (≈ 7.8 mm) for A-side and C-side, respectively. The combined resolution is obtained as the square root of the sum of the squared resolutions for each side, and equals about 9.8 mm.

The reduction of the background was calculated as a rejection factor for the assumed $\pm 1\sigma$, $\pm 2\sigma$, $\pm 3\sigma$ ToF time resolutions. The following method to obtain the rejection factor was used: for each simulated signal event, the number of background events is determined within the ToF uncertainty.

$$\text{Rejection factor} = \text{all_data}/\text{selected_data}$$

In addition, the sensitivity was defined:

$$\text{sensitivity} = \text{signal}/\sqrt{\text{background}},$$

where $\text{signal} = 1/\text{rejection_factor}(\text{signal})$,
and $\text{background} = 1/\text{rejection_factor}(\text{background})$.

The results for the rejection factors were obtained for cases with converted and unconverted photons, as given in Table 4.2. As simulated sample ALPs with a mass of 400 GeV were used. The data was collected in 2017. Based on these results it is clear that using the ToF detector can help greatly to reduce the background in the ALP search.

σ	$\sigma(\text{mm})$	Signal Gaus(%)	Photons type	Rejection factor(data)	Rejection factor (signal)	Sens
$\pm 1\sigma$	9.83	68	Conv	1026.40	18.31	1.74
			Unconv	2391.50	19.47	2.51
$\pm 2\sigma$	19.66	95	Conv	437.93	9.03	2.31
			Unconv	1035.86	9.69	3.32
$\pm 3\sigma$	29.50	99.7	Conv	262.54	5.93	2.73
			Unconv	578.23	6.30	3.81

Table 4.2: Rejection factors and sensitivity for converted and unconverted photons for 3 regions ($\pm 1\sigma$, $\pm 2\sigma$, $\pm 3\sigma$). Sens (sensitivity) = $\text{signal}/\sqrt{\text{background}}$.

4.2 Data 2022

In Section 4.1 two approaches were investigated for determining the di-photon vertex. A comparison of the two techniques shows better resolution for

the photon pointing method. Nevertheless, this method has limited opportunities in the case of photons, as they do not leave tracks in trackers. Therefore, for the first analysis of the Run-3 data the calorimeter pointing method was applied.

For this analysis data from run 429142, taken on July 25, 2022, was used. "Calo Pointing Tool" [24] from the source in ATLAS ATHENA [25] was used directly on the DAOD_HIGG1D1 and n-tuple for analysis was created. Events with two photons only were used for this analysis.

Figure 4.8 shows the distributions for the resolutions in data for converted and unconverted photons with fitted curve overlaid. Resolutions were obtained as a difference between vertices of two photons in the data 2022. These distributions do not have a fully Gaussian shape, therefore a double-Gaussian fit was applied to the data.

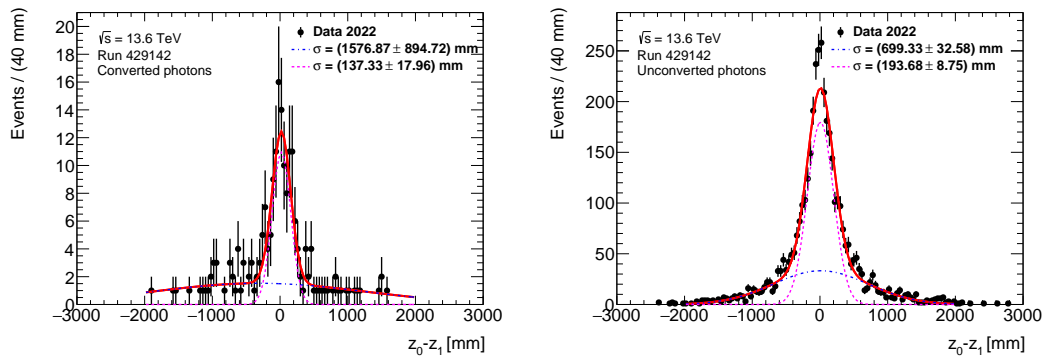


Figure 4.8: Resolutions for converted (left) and unconverted (right) photons for first Run-3 data from 2022 using the calorimeter pointing method with fitted curve overlaid. The values, z_0 and z_1 , correspond to the z -position of the leading and the sub-leading photons, respectively.

The distributions for the resolutions of di-photon vertices for the first Run-3 data taken in 2022 are wider than for the data taken in 2017, as shown in subsection 4.1.2 of this chapter. The reason for such a difference is the newness of the data, for which some calibrations are not done yet. Moreover, statistics for the converted photons is poor.

Chapter 5

ToF vertex reconstruction

The capability of the ToF detector to measure the z -coordinate of the primary vertex in interactions of kind $pp \rightarrow pXp$ is investigated in this chapter.

Vertex reconstruction using ToF is based on the proton arrival times on the A and C sides of the AFP system. The z -coordinate of the primary vertex (z_{ToF}) is basically calculated as follows:

$$z_{\text{ToF}} = \frac{c}{2}(t_C - t_A). \quad (5.1)$$

This formula represents a general approach, but cannot be used directly on the data; firstly arrival times should be corrected for possible time offsets, which is shown in first section of this chapter (5.1).

The final corrected z_{ToF} is then used for the distribution $z_{\text{ATLAS}} - z_{\text{ToF}}$, whose width represents the combined resolution of the z_{ToF} and z_{ATLAS} measurement. z_{ATLAS} here is the z -coordinate of the reconstructed primary vertex, provided by the central ATLAS detector with resolution at the level of $\approx 30 \mu\text{m}$. The distribution of $z_{\text{ATLAS}} - z_{\text{ToF}}$ contains a background from the random coincidences of protons measured in the ToF, but not originating from $pp \rightarrow pXp$ processes and whose arrival time spreads are mainly driven by the beamspot size.

For this analysis, some general requirements on the data samples were applied:

- One track in the SiT per event.
- At most one cluster per plane in the SiT per event.
- One active train in the ToF per event.
- Cut on measured ToF arriving time period.

Full data from the low- μ run 435229 and the high- μ run 429142 are used in this study and are compared.

5.1 Time delays correction

The time measured in one ToF channel i (for example, channel 0A is train 0, bar A) is made up from several components as follows:

$$t_i = t_{\text{proton}} + t_{i,\text{delay}} + t_{i,\text{smear}} - t_{\text{clock}} \quad (5.2)$$

Here the t_{proton} is the proton arrival time, the $t_{i,\text{delay}}$ is a constant time offset in exact ToF channel, appeared because of the signal delay (for example, it can be caused by signal cable lengths). Therefore, this time delay is constant for the given ToF channel, if there was no intervention into the system (e.g. during data taking of the one run for sure). The $t_{i,\text{smear}}$ represents all random effects of the signal processing, for example variation in Cherenkov photon statistics or effects of electronics. The t_{clock} is a reference clock that opens a 25 ns window within which the leading protons from a single bunch-crossing arrive to the ToF.

The t_{proton} and t_{clock} can be abolished by measuring time differences on the event by event basis within one ToF train. This approach also allows to deal with the $t_{i,\text{delay}}$, which is required for this study.

The main goal of this part is to determine $t_{i,\text{delay}}$, which is done using Δt_{ij} distributions which are defined as follows:

$$\begin{aligned} \langle \Delta t_{ij} \rangle &= \langle t_i - t_j \rangle = \langle t_{i,\text{smear}} + t_{i,\text{delay}} - t_{j,\text{smear}} - t_{j,\text{delay}} \rangle \\ &= \langle t_{i,\text{delay}} - t_{j,\text{delay}} \rangle, \end{aligned} \quad (5.3)$$

where $\langle t_{i,\text{smear}} \rangle$ cancels for all channels.

For determination of the delay correction constants an approach [18] is used with the z -position of the luminous ATLAS beamspot, which is measured by the central ATLAS detector. The z_{ToF} value, determined using Equation 5.1, in its mean value copy the z -position of the luminous ATLAS beamspot, therefore the following relation is used:

$$\langle z_{\text{ToF}}^{(ij)} \rangle = z_{\text{BS}} - (D_A^i - D_C^j) \quad (5.4)$$

where D_A^i and D_C^j are mentioned above delay correction constants for the given ToF channels i and j in A and C sides, respectively, which were used for determination of the z_{ToF} . The mean value is obtained over the time period of one LHC LB [26] (~ 1 min of data taking). These delay correction constants are unique for the each pair of the ToF channels and basically only their difference matters to correct positions of the z_{ToF} in given ToF channels. The following equation was used for the determination of this difference, assuming that the mean value is obtained over the one lumiblock and the fact that z_{BS} does not change within one LB (showed as sum over LBs, \sum_{LB})

$$\langle \sum_{LB} z_{\text{ToF}}^{(ij)} - z_{\text{BS}} \rangle = D_C^j - D_A^i \quad (5.5)$$

With event by event approach only double-tag events are used, which means that signal is required in both sides of the AFP system (A and C) simultaneously. However, this significantly reduces the data statistics. Therefore, another approach was used to create pseudo-double-tag events from single-tag events. This approach is called event mixing. For this analysis the time buffers were filled with time values measured during one LB and then pseudo-double-tag events can be produced.

The ToF has 16 channels on each side, therefore there exist $16 \times 16 = 256$ combinations of channels. For each of them the distribution corresponding to Equation 5.5 was created and a Gaussian fit was applied to determine the mean value. A few examples of such distributions with fitted curve overlaid are given in Figure 5.1 for run 429142 and in Figure 5.2 for low- μ run 435229.

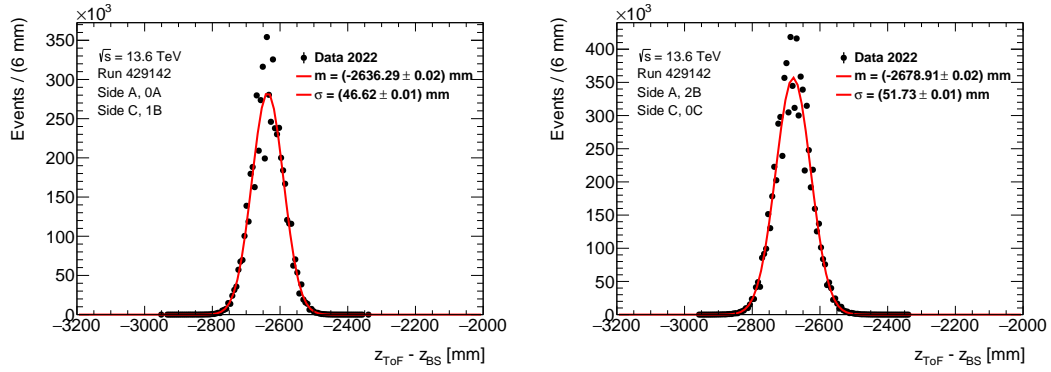


Figure 5.1: $z_{\text{ToF}} - z_{\text{BS}}$ distributions for the run 429142 with a Gaussian fitted curve overlaid for 2 combinations of the ToF channels. Left - side A 0A (train 0, bar A) with side C 1B (train 1, bar B). Right - side A 2B (train 2, bar B) with side C 0D (train 0, bar D).

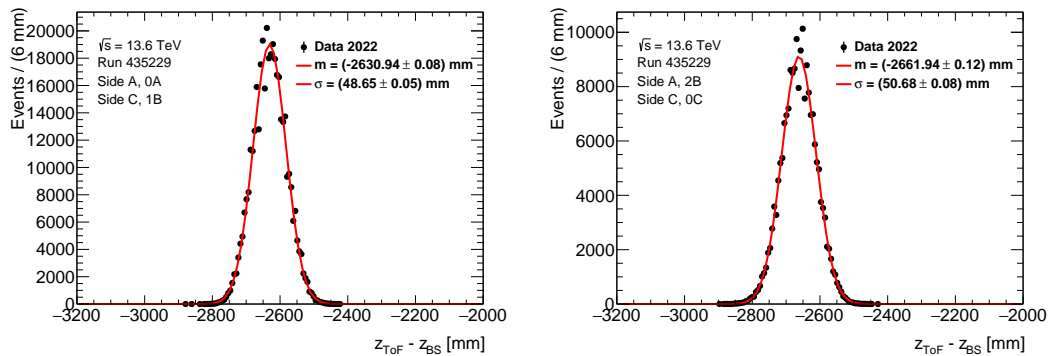


Figure 5.2: $z_{\text{ToF}} - z_{\text{BS}}$ distributions for the low- μ run 435229 with Gaussian fitted curve overlaid for 2 combinations of the ToF channels. Left - side A 0A (train 0, bar A) with side C 1B (train 1, bar B). Right - side A 2B (train 2, bar B) with side C 0D (train 0, bar D).

The mean values of these fits define the differences between the delay correction constants for each of the 256 combinations of the ToF channels, according to Equation 5.5. All combinations are shown in Figure 5.3 for both runs. The mapping of the indices is performed by means of the logic:

$$\begin{aligned}
 & \text{for}(i = \text{Index}_{[\text{SideA}]}) \\
 & \{ \\
 & \quad \text{for}(j = \text{Index}_{[\text{SideC}]}) \\
 & \quad \{ \\
 & \quad \quad D_C^j - D_A^i \\
 & \quad \} \\
 & \} ,
 \end{aligned} \tag{5.6}$$

which means that in each iteration a channel on the A-side is chosen and channels on the C-side are taken one by one to form combinations, then the procedure is repeated for each channel on the A-side. Some structure in the differences depending on the channel combination can be seen.

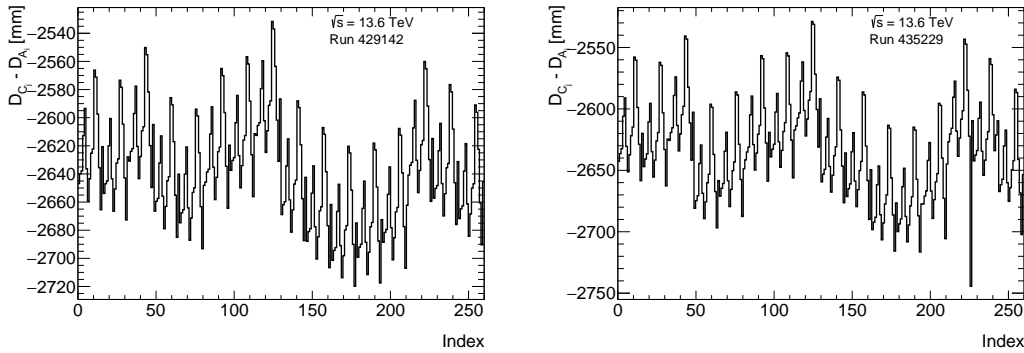


Figure 5.3: All differences between delay correction constants for each of the 256 combinations of the ToF channels for the run 429142 (left) and for the low- μ run 435229 (right).

These 256 differences between delay correction constants can be parameterized in terms of the D_A^i and D_C^j to find 32 correction factors (D_A^i , D_C^j). This was done using a fit as shown in Figure 5.4 for both runs. Finally, all delay correction constants are determined for each channel on both sides for both runs. Figure 5.5 shows them in mm.

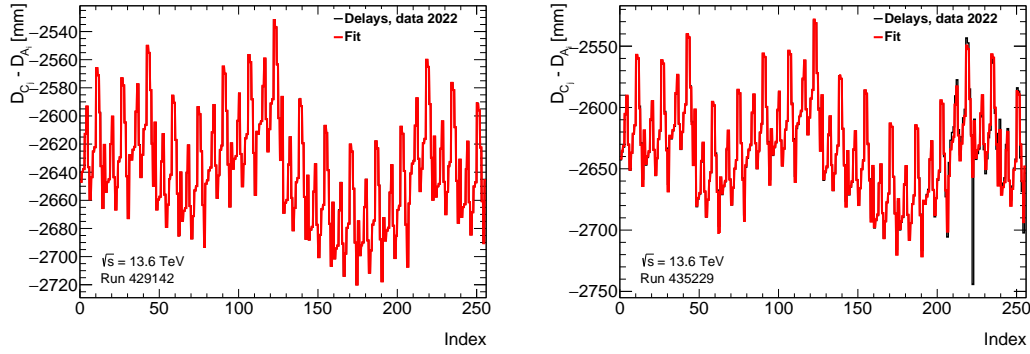


Figure 5.4: All differences between delay correction constants for each of the 256 combinations of the ToF channels with fit overlaid for the run 429142 (left) and for the low- μ run 435229 (right).

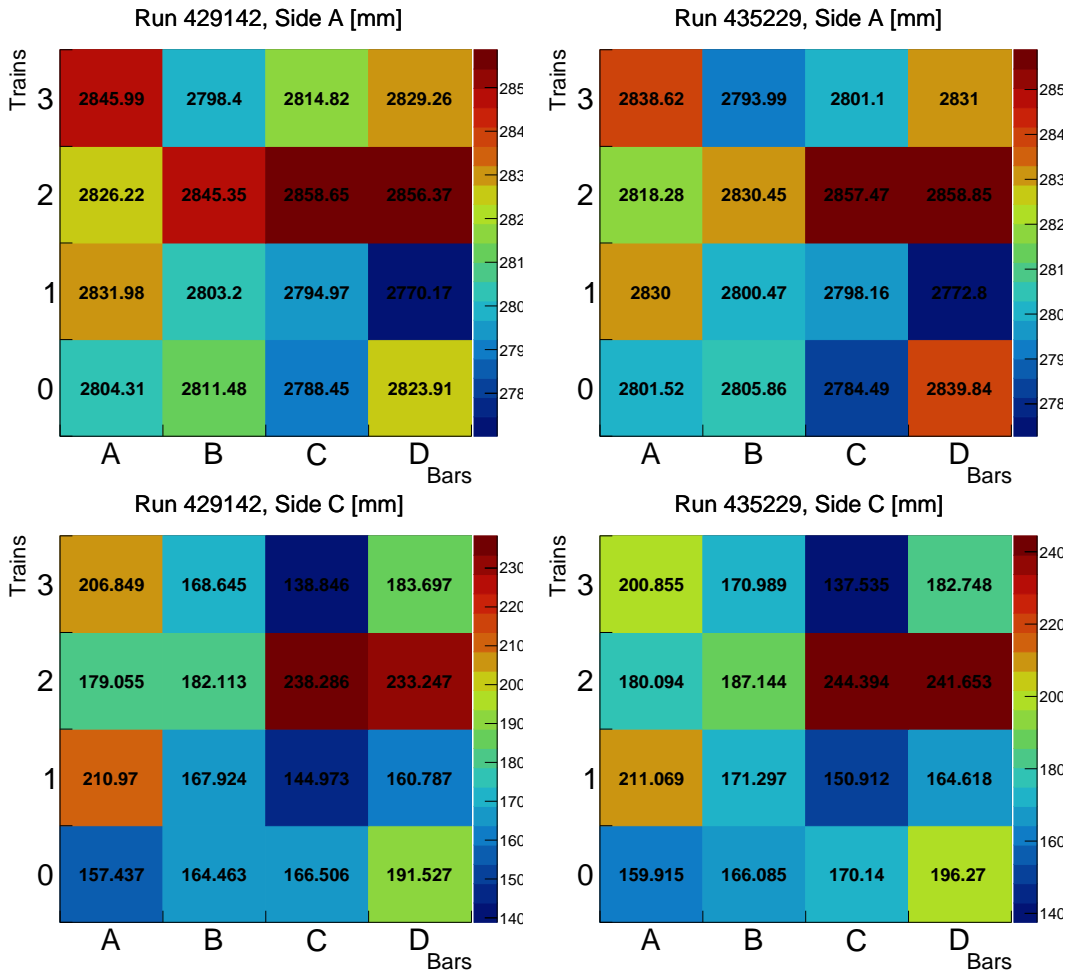


Figure 5.5: Delay correction constants for all ToF channels on A-side (top) and C-side (bottom) for the run 429142 (left) and for the low- μ run 435229 (right).

After all the corrections are determined it is possible to correct the z_{ToF}

position and compare it with the z_{BS} position. The dependence of the z_{BS} on lumiblock (basically - on time) is not uniform and differs in each particular run. As the z_{ToF} copying the z_{BS} , procedure of time delay corrections is checked by comparing the dependence of the z_{BS} and z_{ToF} per LB. The raw positions of z_{ToF} are distributed around the z_{BS} in a Gaussian-like manner. Therefore, Gaussian fit was applied.

Figure 5.6 shows the dependence of the z_{BS} and z_{ToF} per LB before and after the corrections on time delays for both runs. Figure 5.7 shows the dependence of the z_{BS} and z_{ToF} per LB after the corrections on time delays for both runs in a magnified way, which allows it to be seen clearly that the z_{ToF} repeats the form of the z_{BS} .

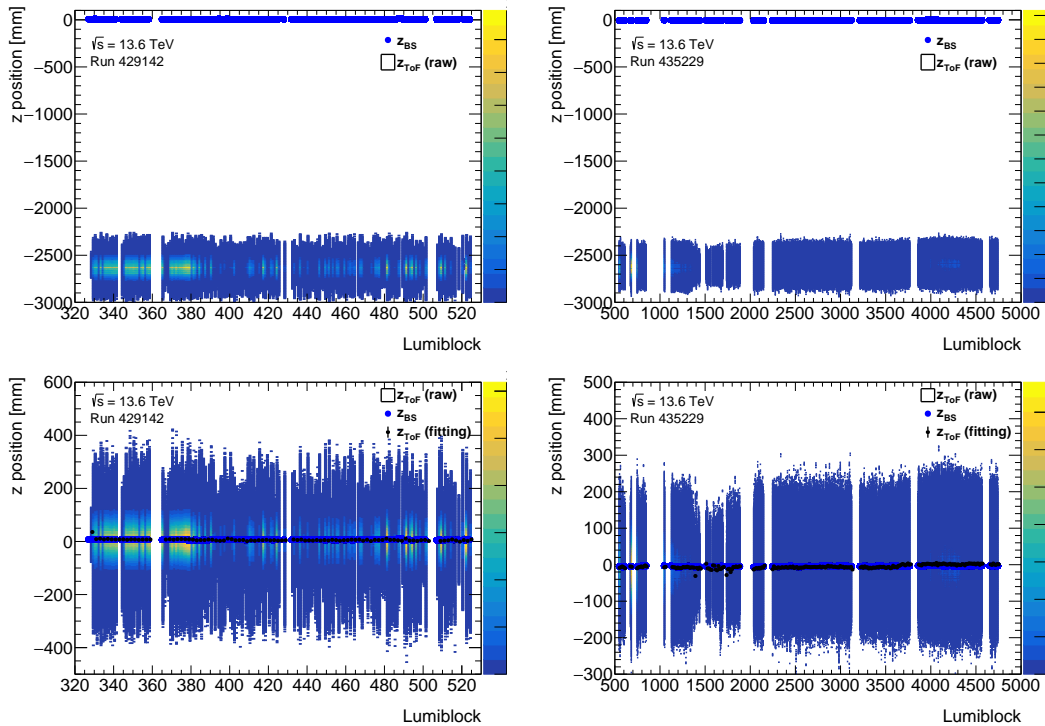


Figure 5.6: Dependence of the z_{BS} and z_{ToF} per LB before (top) and after (bottom) the corrections on time delays for the run 429142 (left) and for the low- μ run 435229 (right).

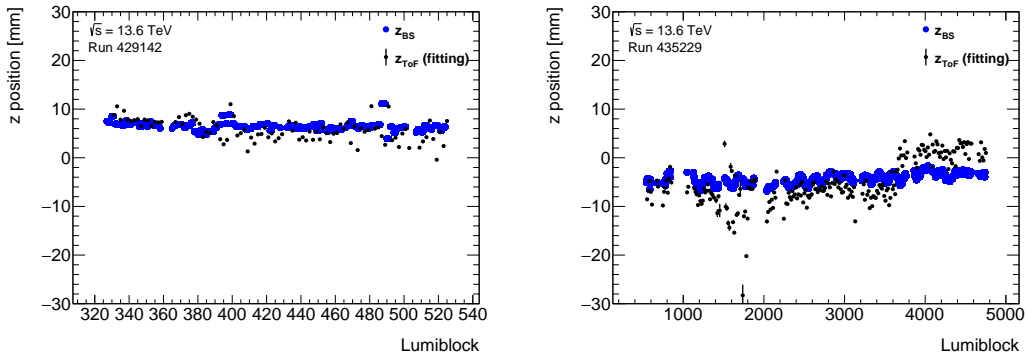


Figure 5.7: Dependence of the z_{BS} and z_{ToF} per LB after the corrections on time delays for the run 429142 (left) and for the low- μ run 435229 (right), magnified version.

5.2 Vertex matching

The ToF detector reconstructs the primary vertex in the case of finding two leading protons under the proper conditions. However, it can reconstruct fake vertices caused by a fake double-tag of two leading protons from two unrelated events.

It is possible to measure the production vertex of a $pp \rightarrow pXp$ process from the time information of the two leading protons on each side. If z_{ToF} happens to be measured from protons that truly are coming from the primary ATLAS vertex, a narrow enhancement is observed in the otherwise wide $z_{\text{ATLAS}} - z_{\text{ToF}}$ distribution. In other words, the primary vertex position in ATLAS (z_{ATLAS}) and z position from ToF (z_{ToF}) are correlated for the signal processes; the projection to the $z_{\text{ATLAS}} - z_{\text{ToF}}$ is a convenient way for searching for such correspondence.

Then, in a given data sample if a cut is applied on such $z_{\text{ATLAS}} - z_{\text{ToF}}$ observable (e.g. a window around the signal peak, whose width is driven by the resolution) some statistics will be lost (the events in the wide tails are cut away, but these are mostly background) and the signal is enriched, because the sub-selected sample contains larger fraction of genuine signal events than the whole sample.

For this analysis only the low- μ run 435229 is used, since high- μ runs include too much combinatorics. The variable z_{ToF} is corrected on time delays, discussed in Section 5.1. Figure 5.8 shows $z_{\text{ATLAS}} - z_{\text{ToF}}$; the wide distribution indicates background and narrow one is the signal.

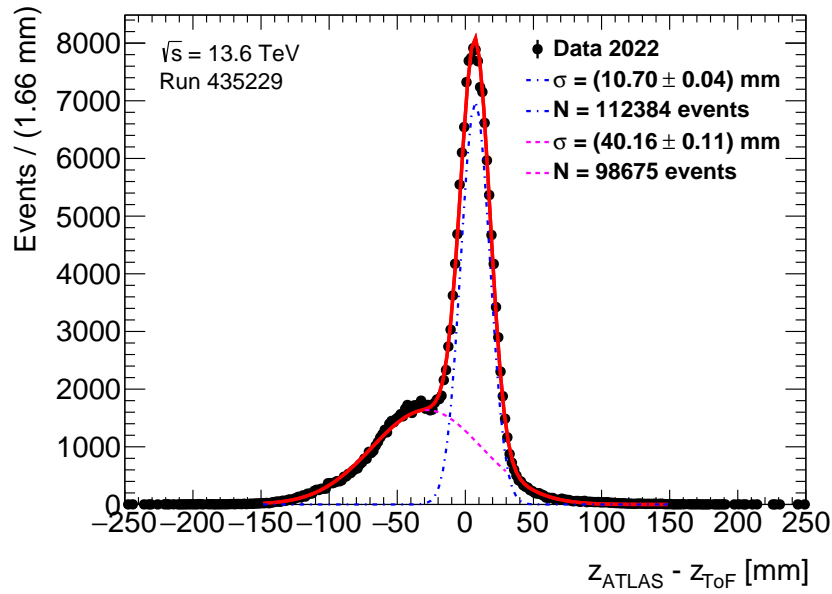


Figure 5.8: The distribution of the $z_{\text{ATLAS}} - z_{\text{ToF}}$ for the low- μ run 435229.

The background distribution is shifted to the left with respect to the signal distribution. This is caused by the unevenness of the Δt distributions in the train 2, which was shown in Section 3.2. By excluding this train from the vertex matching analysis, the background is reduced. Figure 5.9 shows $z_{\text{ATLAS}} - z_{\text{ToF}}$ distribution for data, excluding ToF train 2.

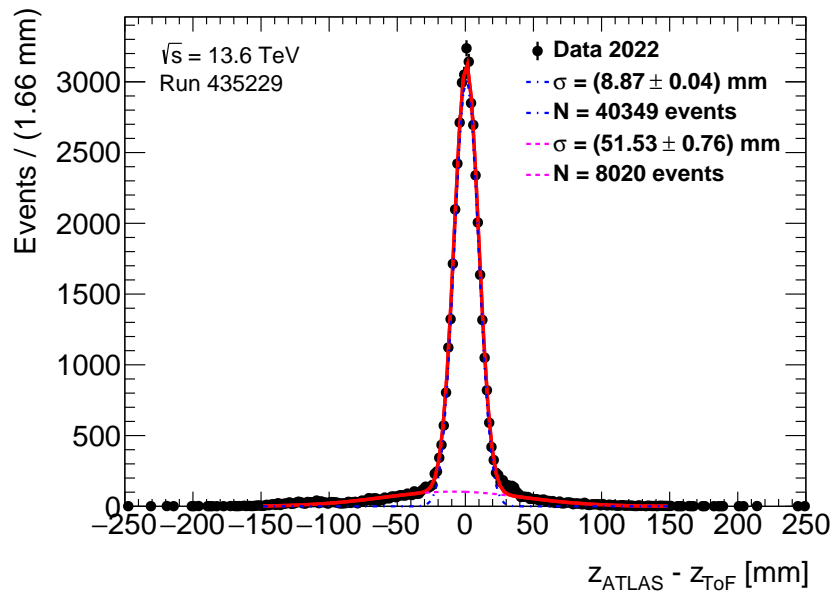


Figure 5.9: The distribution of the $z_{\text{ATLAS}} - z_{\text{ToF}}$ for the low- μ run 435229 excluding train 2.

Excluding train 2 from the analysis significantly reduced background and improved the resolution of the signal distribution from 10.70 mm to 8.87 mm. At the same time it decreased statistics, however, it is still enough to perform the analysis. The sensitivity of the approach to the signal can be checked using Equation 5.7:

$$\text{sensitivity} = \text{signal} / \sqrt{\text{background}}, \quad (5.7)$$

according to which sensitivity for the full data is about 357 and after the excluding train 2 is about 450.

The width of the signal distribution is $\sigma = 8.87$ mm. To convert it to the single side resolution, Equation 5.1 is used for the determination of z_{ToF} , including a factor 1/2. Thus, the resolution in length units is calculated as follows, assuming that both sides are the same:

$$\sigma_{\text{length}} = \frac{c}{2} \sqrt{\sigma_{\text{time,A}}^2 + \sigma_{\text{time,C}}^2} = \frac{c}{2} \sigma_{\text{time}} \sqrt{2}. \quad (5.8)$$

According to Equation 5.8, the single side resolution in ps is calculated:

$$\sigma_{\text{ps}} = \frac{\sqrt{2}}{c} \sigma_{\text{mm}} \times 10^9 \approx 41.84 \text{ ps}, \quad (5.9)$$

where the speed of light is in m/s.

This indicates that the ToF works well and definitely can reconstruct signal events; however, the resolutions are still not fully established, which was also shown in Section 3.2. Figure 5.10 shows $z_{\text{ATLAS}} - z_{\text{ToF}}$ distribution for the data from 2017 [18]. In data from 2022 the signal is much better visible, which is result of better efficiency of the ToF detector in Run-3 in comparison with Run-2. However, the resolution in data 2017 is better, due to the single-channel resolutions which were fully established in data from 2017, which did not have some effects which are present in data from 2022. Therefore, it must be stressed out that results obtained in data from 2022 are very preliminary and cannot be compared with results from 2017 directly, only indicatively.

Applying the ToF data to the di-photon vertex reconstruction is not appropriate at the moment, owing to the very different orders of the resolutions for the di-photon vertex reconstruction (Section 4.2) and that of the ToF one. Because of this large difference in resolutions, the ToF data will be absorbed and lost in combinatorics.

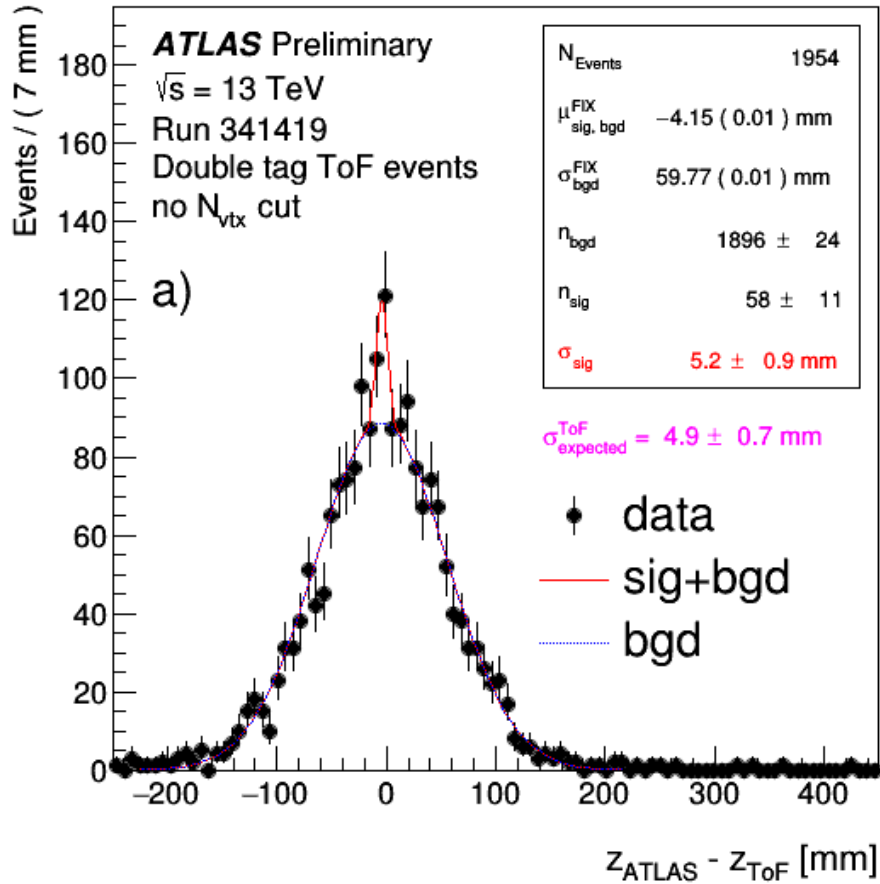


Figure 5.10: The distribution of $z_{\text{ATLAS}} - z_{\text{ToF}}$ measured in events with ToF signals on both sides of the interaction region in run 341419 in data 2017, where z_{ATLAS} is the primary vertex z -position reconstructed by ATLAS. The z_{ToF} is obtained as $z_{\text{ToF}} = -\frac{c}{2} \Delta t$, where Δt is the time difference of proton arrival times in A and C far stations of the AFP measured by ToF. The distribution correspond to the ATLAS data containing a reconstructed primary vertex together with coincidence of signals in both ToF detectors in scenario with no cut on number of vertices reconstructed by ATLAS. A double Gaussian function representing the signal and background components is fitted to unbinned data samples using the extended likelihood fit as implemented in RooFit. The mean of the signal component as well as the mean and width of the background component are always estimated from a Gaussian fit to the mixed event data, denoted as $\mu_{\text{sig}}^{\text{FIX}}$, $\mu_{\text{bgd}}^{\text{FIX}}$ and $\sigma_{\text{bgd}}^{\text{FIX}}$. The mixed event data $z_{\text{ATLAS}} - z_{\text{ToF}}$ distributions are obtained by random mixing of times measured by ToF in either station and the z_{ATLAS} values which do not originate in the same collision event. The expected resolution of the ToF detector, quoted as $\sigma_{\text{expected}}^{\text{ToF}}$ is obtained from the known single-channel resolutions convoluted with the actual channel-hit-patterns observed in the data [18].

Chapter 6

Future applications on an ALP search

Searches for the hypothetical Axion-like particles are a hot topic in a modern science. Many extensions of the Standard Model use them as possible candidates for particles that make up dark matter.

At the Large Hadron Collider the electromagnetic fields between protons are strong enough to create powerful fluxes of high-energy virtual photons. These photons can interact, for example, by merging together and then decaying into various final states. Photon fusion is a separate way of looking for physics BSM. Scattering of light by light mediated by ALPs is prohibited in the classical theory of electrodynamics. In various extensions, additional contributions are possible, which makes light-by-light scattering measurements sensitive to physics BSM, which can be used to search for an Axion-like particle.

A search for a forward proton scattering in association with light-by-light scattering mediated by an Axion-like particle was performed using central ATLAS detector and Silicon Tracker from the AFP system [27], however without any ToF data.

In processes such as central exclusive di-photon production $pp \rightarrow p(\gamma\gamma)p$, photons are recorded with the ATLAS central detector and the vertex position of the di-photons is used as a criterion to separate di-photon events coming from the expected ALP signal, from di-photon events produced in other background processes. Therefore, an improved di-photon vertex resolution will contribute to better separate signal and background events.

The ToF detector can provide data to improve the vertex reconstruction, in particular for di-photon events. This additional data improves largely the di-photon vertex reconstruction as currently the di-photon vertex reconstruction uses calorimeter data which was taken at a large distance from the interaction point in the central detector. The extrapolation from the calorimeters to the interaction point has therefore inherently a large uncertainty.

In this analysis performance of the ToF detector on first Run-3 data was

studied. In future searches data provided by the ToF can be used for improvement of the vertex reconstruction, and therefore will help to reduce background in ALP searches.

The 2017 AFP data have been used in a recent ATLAS publication on an Axion-like particle (ALP) search [27]. It is planned that the ALP analysis will be extended using the LHC Run-3 data. The sensitivity for an ALP will be greatly increased by the larger integrated luminosity and an enhanced background reduction using the ToF detector.

Chapter 7

Conclusions

The first performance study of recorded Run-3 ToF detector data has been conducted. It provides a preliminary understanding on efficiencies and resolutions of the ToF detector. Preliminary resolutions were found to be consistent with the expectations. Different approaches for obtaining efficiencies were tested and the results are compared with each other. In addition, the performance study includes primary proton-proton vertex reconstruction using the ToF detector and vertex matching analyses with the central ATLAS detector. The resulting resolution of the ToF vertex reconstruction is less than 10 mm, which is consistent with the expectations.

The study was performed on two data sets, with high ($\langle \mu \rangle = 37.5$) and low ($\langle \mu \rangle = 0.02$) pile-up. The low- μ run was the longest run in 2022 with a duration of 2 days 20 hours.

In addition, the vertex reconstruction study of di-photon events has been part of a larger effort to use the AFP information together with central ATLAS detector information to search for an Axion-Like-Particle with a di-photon resonance signature, produced in ultraperipheral pp interactions, also known as Light-by-Light (LbyL) scattering. The vertex information is used to reduce the expected background contributions, and in this study the performance increase is estimated when including ToF detector data. The improved vertex reconstruction of di-photon events largely suppresses background. Two approaches for the vertex reconstruction were compared using 2017 data. The calorimeter pointing method is found to be more suitable. Therefore, this method was applied for the determination of the di-photon vertex reconstruction in the first 2022 data.

The expected improvement of the vertex reconstruction including ToF data, based on simulation, is shown to reduce greatly the background for an ALP di-photon search.

Bibliography

1. N. DU, ET AL. *A Search for Invisible Axion Dark Matter with the Axion Dark Matter Experiment* [Phys. Rev. Lett. 120 (2018) 151301]. 2018. Available also from: <https://arxiv.org/abs/1804.05750>.
2. G. BERTONE, D. HOOPER AND J. SILK. *Particle dark matter: Evidence, candidates and constraints* [Phys. Rept. 405 (2005) 279]. 2005. Available also from: <https://arxiv.org/abs/hep-ph/0404175>.
3. R. D. PECCEI AND H. R. QUINN. *CP Conservation in the Presence of Instantons* [Phys. Rev. Lett. 38 (1977) 1440, [328(1977)]]. 1977. Available also from: <https://journals.aps.org/prl/abstract/10.1103/PhysRevLett.38.1440>.
4. C. BALDENEGRO, S. FICHET, G. VON GERSDORFF AND C. ROYON. *Searching for axion-like particles with proton tagging at the LHC* [JHEP 06 (2018) 131]. 2018. Available also from: <https://arxiv.org/abs/1803.10835>.
5. L. EVANS. *The Large Hadron Collider*. 2007. Available also from: <https://iopscience.iop.org/article/10.1088/1367-2630/9/9/335/meta>.
6. J. M. BUTTERWORTH, D. GRELLSCHEID, M. KRÄMER, B. SARRAZIN AND D. YALLUP. *Constraining new physics with collider measurements of Standard Model signatures* [JHEP 03 (2017) 078]. 2017. Available also from: <https://arxiv.org/abs/1606.05296>.
7. H. EULER. *On the scattering of light by light according to Dirac's theory* [Annalen Phys.418,no.5,398(1936)]. 1936. Available also from: <https://onlinelibrary.wiley.com/doi/10.1002/andp.19364180503>.
8. ATLAS COLLABORATION. *Observation of light-by-light scattering in ultraperipheral Pb+Pb collisions with the ATLAS detector* [Phys. Rev. Lett. 123 (2019) 052001]. 2019. Available also from: <https://arxiv.org/abs/1904.03536>.
9. L. ADAMCZYK, ET AL. *AFP: A Proposal to Install Proton Detectors at 220,m around ATLAS to Complement the ATLAS High Luminosity Physics Program* [tech. rep. ATL-COM-LUM-2011-006, AFP technical proposal: CERN]. 2011. Available also from: <https://cds.cern.ch/record/1331213>.

10. ATLAS COLLABORATION. *Observation and measurement of forward proton scattering in association with lepton pairs produced via the photon fusion mechanism at ATLAS* [Phys. Rev. Lett. 125, 261801 (2020)]. 2020. Available also from: <https://arxiv.org/abs/2009.14537>.
11. CMS COLLABORATION, TOTEM COLLABORATION. *Observation of proton-tagged, central (semi)exclusive production of high-mass lepton pairs in pp collisions at 13 TeV with the CMS-TOTEM precision proton spectrometer* [JHEP 07 (2018) 153]. 2018. Available also from: <https://arxiv.org/abs/1803.04496>.
12. ATLAS COLLABORATION. *The ATLAS Experiment at the CERN Large Hadron Collider*. 2008. Available also from: <https://iopscience.iop.org/article/10.1088/1748-0221/3/08/S08003>.
13. J. LANGE, ET AL. *Beam tests of an integrated prototype of the ATLAS Forward Proton detector* [Journal of Instrumentation 11 (2016) P09005]. 2016. Available also from: <http://stacks.iop.org/1748-0221/11/i=09/a=P09005>.
14. HERAEUS. *Suprasil UVL datasheet*. 2018. Available also from: https://www.heraeus.com/media/media/hqs/doc_hqs/products_and_solutions_8/optics/Suprasil_UVL_synthetic_fused_silica_EN.pdf.
15. L. NOZKA, A. BRANDT, M. RIJSSENBEK, T. SYKORA, T. HOFFMAN, J. GRIFFITHS, J. STEFFENS, P. HAMAL, L. CHYTKA, AND M. HRABOVSKY. *Design of Cherenkov bars for the optical part of the time-of-flight detector in Geant4*. 2014. Available also from: <https://opg.optica.org/oe/fulltext.cfm?uri=oe-22-23-28984&id=304628>.
16. M. RIJSSENBEK. *‘ATLAS Forward Proton Detectors: Time-of-Flight Electronics* [Proceedings of Workshop on Picosecond Photon Sensors for Physics and Medical Applications, Clermont-Ferrand, France, March 12–14, 2014, Acta Phys. Pol. B Proc. Suppl. Vol. 7, 2014 751]. 2014.
17. M. MOTA, ET AL. *A flexible multi-channel high-resolution time-to-digital converter ASIC* [2000 IEEE Nuclear Science Symposium. Conference Record (Cat. No.00CH37149), vol. 2, 2000 9/155]. 2000.
18. ATLAS COLLABORATION. *Performance of the ATLAS Forward Proton Time-of-Flight Detector in 2017* [ATL-FWD-PUB-2021-002]. 2021. Available also from: <https://cds.cern.ch/record/2749821>.
19. THE LHCf COLLABORATION, ET AL. *The LHCf detector at the CERN Large Hadron Collider*. 2008. Available also from: <https://iopscience.iop.org/article/10.1088/1748-0221/3/08/S08006>.

20. J. CATMORE, J. CRANSHAW, T. GILLAM, E. GRAMSTAD, P. LAYCOCK, N. OZTURK, G. A. STEWART. *A new petabyte-scale data derivation framework for ATLAS* [Journal of Physics Conference Series 664(7):072007]. 2015. Available also from: https://www.researchgate.net/publication/288021245_A_new_petabyte-scale_data_derivation_framework_for_ATLAS.
21. BAIRD, S. *Accelerators for pedestrians* [AB-Note-2007-014 OP, CERN]. 2007. Available also from: <http://cdsweb.cern.ch/record/1017689>.
22. *AFPTrackContainer*. Available also from: https://atlas-sw-doxygen.web.cern.ch/atlas-sw-doxygen/atlas_22.0.X-DOX/docs/html/d0/d58/classxAOD_1_1AFPTrack__v1.html.
23. *Calo Pointing Tool from Delayed Hino Analysis*. Available also from: <https://gitlab.cern.ch/jgonski/delayedhinoanalysis>.
24. *Calo Pointing Tool from ATLAS ATHENA*. Available also from: <https://acode-browser2.usatlas.bnl.gov/lxr/source/r22/athena/PhysicsAnalysis/ElectronPhotonID/PhotonVertexSelection/Root/PhotonPointingTool.cxx>.
25. *ATLAS ATHENA framework*. Available also from: <https://atlassoftwaredocs.web.cern.ch/athena/>.
26. ATLAS COLLABORATION. *Luminosity determination in pp collisions at $\sqrt{s} = 8$ TeV using the ATLAS detector at the LHC* [Eur. Phys. J. C 76 (2016) no.12, page 653]. 2016. Available also from: <https://link.springer.com/article/10.1140/epjc/s10052-016-4466-1>.
27. ATLAS COLLABORATION. *Search for an axion-like particle with forward proton scattering in association with photon pairs at ATLAS*. 2023. Available also from: <https://arxiv.org/abs/2304.10953>.

Acronyms

AFP	ATLAS Forward Proton. 2, 4, 6, 39, 47, 49, 56–59
ALP	Axion-like particle. 2, 39–41, 43, 44, 57–59
ALPs	Axion-like particles. 1, 44, 57
AOD	Analysis Object Data. 7
ATLAS	A Toroidal LHC Apparatus. 3, 4, 7, 39, 47, 48, 56–59
BSM	Beyond the Standard Model. 1, 57
CFD	constant fraction discriminator. 6
CP	Charge conjugation times Parity. 1
DAOD	Derived Analysis Object Data. 41
HPTDC	high performance time-to-digital converter. 6
LB	lumiblock. 48, 49, 52, 53
LHC	Large Hadron Collider. 1–3, 6, 8, 39, 48, 58
LHCf	Large Hadron Collider forward. 7
PMT	Photomultiplier Tube. 6
PV	Primary Vertex. 39, 40
QED	Quantum Electrodynamics. 1
RF	Radiofrequency. 8
RP	Roman Pots. 2
SiT	Silicon pixel Tracker. 2, 4–8, 11, 24, 25, 27–29, 37, 47
SM	Standard Model. 1

ToF Time-of-Flight. 2, 4–9, 11–22, 24, 25, 27–37,
39, 44, 47–51, 53–59